Spin-dependent Transport of Interacting Electrons in Mesoscopic Systems

Dissertation

zur Erlangung des Doktorgrades
der Naturwissenschaften (Dr. rer. nat.)
der Naturwissenschaftlichen Fakultät II – Physik
der Universität Regensburg

vorgelegt von

Andreas Laßl

aus Regenstauf

Oktober 2007

Promotionsgesuch eingereicht am 23. Oktober 2007
Promotionskolloquium am 16. November 2007

Die Arbeit wurde angeleitet von Prof. Dr. Klaus Richter

Prüfungsausschuß:

Vorsitzender:	Prof. Dr. Christoph Strunk
1. Gutachter:	Prof. Dr. Klaus Richter
2. Gutachter:	Prof. Dr. Milena Grifoni
Weiterer Prüfer:	Prof. Dr. Andreas Schäfer

Contents

List of symbols

Symbol	Description
a	lattice constant of the numerical grid
$A(\vec{x},\vec{x}';E)$	spectral function
$\vec{A}$	vector potential of the magnetic field
$\vec{B}$	magnetic field, $\vec{B}=\vec{\nabla}\times\vec{A}$
β	inverse temperature, $\beta=1/(k_BT)$
$d(E)$	density of states
$\delta(x)$	Dirac delta distribution
$\delta_{i,j}$	Kronecker symbol, $\delta_{i,j}=1$ for $i=j$, otherwise $\delta_{i,j}=0$
e	charge quantum $e=1.60\times10^{-19}\,\mathrm{As}$; the electron charge is $-e$
ε	relative dielectric constant
ε_0	vacuum dielectric constant, $\varepsilon_0=8.85\times10^{-12}\,\mathrm{As/(Vm)}$
E	energy
E_Z	Zeeman energy, $E_Z=g\mu_B B$
$f(E,\mu)$	Fermi-Dirac distribution function, $f(E,\mu)=[\mathrm{e}^{\beta(E-\mu)}+1]^{-1}$
g	gyromagnetic ratio, for free electrons $g\approx2$
G	conductance
G_0	conductance quantum, $G_0=2e^2/h=7.75\times10^{-5}\,\mathrm{A/V}$
$\mathcal{G}$	time-ordered Green function
$\mathcal{G}^{r(a)}$	retarded (advanced) Green function
$\mathcal{G}^{<(>)}$	lesser (greater) Green function
$\mathcal{G}_0^{(r,a,>,<)}$	Green function of the noninteracting system
γ	interaction strength for the delta-type interaction
h	Planck's constant, $h=6.63\times10^{-34}\,\mathrm{Js}$
$\hbar$	scaled Planck's constant, $\hbar=h/(2\pi)=1.05\times10^{-34}\,\mathrm{Js}$
H_0	Hamilton operator of noninteracting particles
$\mathcal{H}$	full Hamiltonian including interactions
I	current
k_B	Boltzmann constant, $k_B=1.38\times10^{-23}\,\mathrm{J/K}$
κ	energy unit in the lattice representation, $\kappa=\hbar^2/(2ma^2)$
m	effective electron mass, for GaAs $m=0.07m_0$
m_0	free electron mass, $m_0=9.11\times10^{-31}\,\mathrm{kg}$
μ	chemical potential
μ_B	Bohr magneton, $\mu_B=e\hbar/(2m_0)=9.27\times10^{-24}\,\mathrm{J/T}$
μ_0	magnetic permeability, $\mu_0=4\pi\times10^{-7}\,\mathrm{Vs/(Am)}$
$n(\vec{x})$	particle density
$\vec{\nabla}$	differential operator, $\vec{\nabla}=\left(\frac{\partial}{\partial x},\frac{\partial}{\partial y},\frac{\partial}{\partial z}\right)$
ϕ_0	magnetic flux quantum, $\phi_0=h/e=4.14\times10^{-15}\,\mathrm{Vs}$

Symbol	Description
$\hat{\Psi}^{(\dagger)}(\vec{x},t)$	field operator that destroys (creates) a particle at point $\vec{x}$ at time t
$\vec{r}$	two-dimensional vector in the plane of the electron gas, $\vec{r}=(x,z)$
σ	spin index or spin quantum number, $\uparrow=+1/2$, $\downarrow=-1/2$
$\vec{\sigma}$	vector of Pauli matrices
Σ	self-energy
$S(t,t')$	S-matrix describing the time evolution, $S(t,t')=\hat{U}(t)\hat{U}^{\dagger}(t')$
t	time
T	temperature
$\mathcal{T}$	transmission
$\mathscr{T}$	rocking period
$\Theta(x)$	Heaviside step-function, $\Theta(x)=1$ for $x>0$, $\Theta(x)=0$ otherwise
$U(\vec{x})$	external (confinement) potential
$\hat{U}(t)$	time evolution operator
V	source-drain voltage
$V_{\mathrm{es}}(\vec{x})$	electrostatic potential
$w(\vec{x},\vec{x}')$	interaction potential between particles at $\vec{x}$ and $\vec{x}'$
W	width of the quantum wire
$\mathcal{W}$	interaction Hamiltonian
$\vec{x}$	three-dimensional vector, $\vec{x}=(x,y,z)$
brackets:	
$\{A,B\}$	anti-commutator of the operators A and B, $\{A,B\}=AB+BA$
$[A,B]$	commutator of the operators A and B, $[A,B]=AB-BA$
$\langle A\rangle$	thermal expectation value of the operator A
$\langle Q(\vec{r})\rangle$	spatial average of the quantity $Q(\vec{r})$
$\langle Q(t)\rangle$	temporal average of the quantity $Q(t)$
sub- and superscripts:	
a	advanced function
L	refers to the left lead or contact
r	retarded function
R	refers to the right lead or contact
$\widetilde{X}$	the tilde marks a dimensionless quantity
$\overline{Q}(x)$	the bar refers to quantities $Q(x,z)$, averaged over the z-coordinate
abbreviations:	
2DEG	two-dimensional electron gas
a.u.	arbitrary units
AC	alternating current
DFT	density functional theory

The scientist does not study nature because it is useful; he studies it because he delights in it, and he delights in it because it is beautiful. If nature were not beautiful, it would not be worth knowing, and if nature were not worth knowing, life would not be worth living.

Jules Henri Poincaré (1854-1912)

CHAPTER 1
Introduction

1.1 Towards nanoscale devices

The development of modern electronic equipment such as notebooks, mobile phones or multimedia devices experiences a rapid evolution towards always smaller and more powerful units. This trend continues thanks to the technological progress in designing smaller and smaller electronic components, which simultaneously increases the number of transistors per unit area on a chip. Whereas the first transistor built in the early 1950s had the extensions of several millimeters, nowadays commercial transistors have a channel length down to 45 nm. Already in the early days of electronics Moore realized that the packing density doubles every year, which leads to an exponential increase of the number of transistors per chip [1]. Although the doubling time was later corrected to about two years, the exponential shrinking of the size of electronic components known as *Moore's law* is still valid to date. The reason why the continuous miniaturization process could take place over the last decades is that even the smallest commercial transistors still work in the classical diffusive transport regime. The working principle and the electronic properties did not change essentially during the downscaling. However, there is a natural limit for the validity of Moore's law as soon as the extensions of the devices reach the atomic scale or the scale of the mean free path of the electrons.

In the lab, nanostructures like quantum dots or quantum point contacts can be realized and yet currents through molecules or single atoms could be measured [2]. Whereas the former systems rely on the semiconductor technology, the usage of molecules as conducting elements leads into the novel field of *molecular electronics* [3]. The properties of such nanodevices are dominated by the laws of quantum mechanics, and their fabrication, characterization and understanding is one main subject of today's nanophysics.

The basis for many nanosystems are semiconductor heterostructures which are produced by epitaxial growth of layers of different semiconductor materials such as GaAs and AlGaAs [4]. With present techniques atomically sharp interfaces between the different materials can be achieved. Because of the different band gaps of the distinct materials a band bending occurs close to the interface forming a sharp quantum well in the y-direction perpendicular to the plane of the interface. At temperatures close to zero only the lowest of the discrete quantum well states is occupied giving rise to a strong confinement of the electrons in the y-direction, while the particles can move freely within the (x, z)-plane. One is talking about a two-dimensional electron gas (2DEG) which forms at the interface between different semiconductor materials. Since the electrons in the 2DEG are spatially separated from the donor ions the impurity scattering is reduced. Moreover, at low temperatures, where phonons are absent, and in the presence of clean interfaces the mean free path of the electrons can reach length scales up to several micrometers (see e.g. [5]). 2DEGs serve as the main building blocks for a variety of low-dimensional nanostructures. The in-plane movement of the electrons in a 2DEG can be further confined by additional gating or etching [4] in order to realize quasi-one-dimensional systems like quantum wires or quasi-zero-dimensional quantum dots. The length scale of that systems typically is much shorter than the mean free path of the electrons. Therefore one meets the ballistic transport regime, where the phase coherence of the particles is maintained and the quantum nature of the electrons becomes important. One can observe quantum phenomena like conductance quantization [6, 7], weak localization or conductance fluctuations [8] in ballistic systems.

A promising research direction in order to overcome the limitations of classical electronic devices is the field of spin-based electronics, known as *spintronics* [9–11]. Whereas the spin degree of freedom of the electrons is neglected in conventional electronic devices, here it plays the central role. The idea is to build devices where the information is carried by the electron spin, instead of the charge. From the realization of spintronics devices one expects several advantages like an enhanced data processing speed, higher integration densities and lower electric power consumption compared to standard electronic devices. To use the technological know-how from nowadays electronics it is desirable to build semiconductor-based spintronics devices. Therefore the possibility to inject, manipulate and detect spin-polarized currents in semiconductors is required. A milestone in spin-related electronic effects was the discovery of the giant magneto-resistance (GMR) in 1988 [12, 13], which will be awarded with this year's Nobel prize. The GMR is observed in layered ferromagnet-metal-ferromagnet systems, whose electrical resistance strongly depends on the relative orientation of the magnetization. The resistance of such a device is minimal if the magnetization of the ferromagnets is parallel, and maximal if it is oriented antiparallel. GMR devices have already found their application in read-heads for hard disks and in magnetoresistive random access memory (MRAM) units, which have the great advantage that the information remains stored even after switching off the computer. Another important device is the spin field-effect transistor (SFET) proposed by Datta and Das in 1990

[14]. It consists of ferromagnetic source and drain contacts connected by a narrow semiconducting channel, where the electrons travel ballistically subject to spin-orbit interaction [15, 16]. The strength of the spin-orbit interaction can be tuned by a gate, which allows for an electrostatic control of the precession length of the spins. In that way the current through the SFET is gate-controlled. Though the setup is relatively simple, the SFET could not yet be realized. The main problem is that the injection of a spin-polarized current from a ferromagnetic metal into a semiconductor is highly inefficient due to the conductivity mismatch of the two materials [17].

The usage of the spin orientations "up" and "down" of the electrons to store logical information opens up the way towards quantum computing [18]. In contrast to classical bits a quantum bit incorporates the pure up- and down-states associated with the logical values 0 and 1, but also superpositions of both. This can be used in specially designed algorithms, whereby a quantum computer can solve certain problems much more efficiently than a conventional one.

1.2 Approaches to transport phenomena

In order to use nanodevices as electronic components, an important issue is the understanding of their transport properties. The relevant quantity is the IV-characteristics which relates the current I through a device to the applied voltage V. To understand the transport characteristics theoretically a microscopic description of the electron dynamics including all internal interactions is necessary. During the technological development towards smaller and smaller systems also the description of transport has changed. In this section we shall give a short overview over different approaches and their applicability.

One long standing approach to discuss electronic transport in bulk semiconductor devices on a quasi-classical level is based on the Boltzmann equation [19]. It describes the dynamics of a probability distribution $f(\vec{x}, \vec{p}, t)$ to find a particle with momentum $\vec{p}$ at position $\vec{x}$. The Boltzmann distribution function obviously is a classical object, as in quantum mechanics the simultaneous determination of momentum and position is limited by the uncertainty relation. Furthermore, all phase information about the electrons is neglected in that approach making it inapplicable to describe interference effects like weak localization. However, interaction effects, both elastic and inelastic, can be included in the Boltzmann equation. Hence, it provides a satisfactory description of high energy electron transport on large length and time scales.

In the regime of mesoscopic systems, where the coherence length exceeds the system size, the phase coherence of the electrons is important. The electron transport in such systems can be described by semiclassical methods, where quantum mechanical objects are expressed by means of classical trajectories [20, 21]. They are intensively used in the realm of quantum chaos in order to understand the implications of classically chaotic dynamics in quantum systems. The semiclassical description contains phase information about the electrons, so that it is suitable to account for interference

effects like weak localization. In numerical simulations often the so-called diagonal approximation is used, which neglects all phases and gives the classical transmission and reflection probabilities. To go beyond this level of approximation is numerically very elaborate. In chaotic systems there are analytical methods to sum up all the orbits making use of ergodicity. In this way one obtains universal properties of quantum chaotic systems, rather than system specific results. There are also possibilities to go beyond the diagonal approximation by considering certain types of correlated orbits [21]. Semiclassics, however, is an asymptotic theory which is exact in the so-called semiclassical limit, where the Fermi wavelength is short compared to the system size.

The master equation approach [22] is successfully used to describe electronic transport of nanosystems which are weakly coupled to the leads, like a quantum dot connected to the contacts via tunnel barriers. The starting point typically is a Hamiltonian of the form

$$\mathcal{H} = H_D + H_L + H_T, \tag{1.1}$$

where H_D and H_L are the Hamilton operators of the isolated dot and leads, respectively, and H_T is the tunneling Hamiltonian coupling the individual parts. As a first step the states of the isolated dot are computed. The presence of tunneling affects those states only weakly, wherefore the tunneling Hamiltonian is treated as a perturbation of the isolated dot. From Fermi's Golden Rule one extracts tunneling rates between different states of the system, which then define the changes in the occupation of the individual states. This can be written down in form of a rate equation consisting of an in- and out-scattering contribution, also known as the master equation. The current through the system can then be computed from the occupation probabilities and tunneling rates.

Finally, also the Green function method is a widely used approach to transport phenomena [23–31]. It is a fully quantum mechanical approach equivalent to solving the Schrödinger equation. Knowing the Green function of a system one can easily extract observables like the current or the particle density. The formalism is suitable to describe open systems that are connected to semi-infinite leads. Moreover, it possesses a perturbation expansion for interactions, so that electron-electron or electron-phonon interactions can be included via a proper self-energy. For realistic mesoscopic devices, where the Green functions are represented by large matrices, the perturbation expansion involves an increasing number of matrix multiplications and inversions, making the computations enormously time consuming. Therefore one is often restricted to the 0th or 1st order of the expansion. Employing the nonequilibrium or Keldysh technique it is possible to describe systems in the presence of a nonvanishing external voltage.

1.3 Purpose of this work

Within this thesis we investigate transport properties of ballistic mesoscopic structures. The theoretical approach which is most suitable for our purpose is the Green function

formalism, since we are dealing with open quantum systems that are strongly coupled to the contacts in a regime of Fermi wavelengths comparable with the system size. With the trend towards always smaller devices, interaction effects among the electrons become more and more important. Also nonlinear electron transport of highly biased nanosystems attracted considerable attention during the last decade. Therefore, we are particularly interested in electron-electron interaction effects and the presence of large source-drain voltages. Both aspects can be described within the scope of the nonequilibrium Green function formalism. We will highlight two phenomena in mesoscopic transport which are dominated by interactions: on the one hand the 0.7 conductance anomaly observed in quantum point contacts is caused by interactions. On the other hand, for charge transport through ballistic quantum ratchet devices, which operate in the nonlinear regime, electron-electron interactions play a crucial role.

Often mesoscopic transport properties are investigated in the linear response regime. It is defined by the range of small voltages, where the current I depends linearly on the applied voltage V,

$$I = GV, \tag{1.2}$$

with the conductance G as proportionality constant. In that regime the transport properties are fully characterized by the conductance, which is related to the total quantum mechanical transmission $\mathcal{T}$ by the celebrated Landauer formula [32, 33]

$$G = \frac{2e^2}{h}\mathcal{T}. \tag{1.3}$$

Here, $-e$ is the electron charge, h is Planck's constant, and the quantity $G_0 = 2e^2/h$ is called the conductance quantum. Hence, to compute the conductance one needs to know the transmission, which is connected to the Green function through the Fisher-Lee relation [34]. Therefore, the conductance can be calculated from the system's Green function in a straightforward way.

In many situations the transport of effectively noninteracting electrons is considered, see e.g. [35], with the interaction effects absorbed in an effective confinement potential $U(\vec{x})$ [36]. This description, however, may be inadequate under certain conditions and some phenomena like the 0.7 conductance anomaly cannot be explained without the explicit consideration of interactions. Therefore one objective of this work is to study the modification of the conductance in presence of electron-electron interactions.

Another goal is the description of transport beyond the linear response regime, where the system is exposed to a finite source-drain voltage V. A central question in that regime is the shape of the *potential drop*, i.e. the electrostatic potential $V_{\mathrm{es}}(\vec{x})$ created by the classical Coulomb interaction of the electrons. The potential drop influences the transmission $\mathcal{T}$ and thereby the current

$$I = \frac{2e}{h}\int \mathrm{d}E\, \mathcal{T}(E, V, \mu)\Big(f(E - eV/2, \mu) - f(E + eV/2, \mu)\Big). \tag{1.4}$$

In the above equation, known as the Landauer formula for the current, $f(E, \mu)$ is the Fermi distribution function and μ is the chemical potential. The current thus is obtained by integrating the transmission over the so-called *bias window*, which is defined by the difference of the Fermi functions of the left and right contact. In general the transmission does not only depend on the energy E, but also on the voltage V and the chemical potential μ, as the shape of the electrostatic potential is affected by V and μ.

In this work we are focussing on the influence of interaction effects on the transport properties of mesoscopic systems. In the first part we restrict ourselves to the linear response regime and calculate the conductance of a quantum point contact in the presence of short-range electron-electron interactions. In the second part we concentrate on the self-consistent computation of the electrostatic potential drop due to Coulomb interaction in a biased nanosystem. This allows us to investigate the nonlinear transport characteristics of ballistic charge and spin ratchet devices.

Nanostructures in the linear transport regime

In the first half of this thesis we study the transport properties of a quantum point contact in the linear response regime, where we model the electron-electron interactions by a delta-like interaction potential. In Hartree-Fock approximation, due to the exchange interactions of electrons with equal spins, the resulting interaction acts only between electrons with opposite spins. Using this model we focus on the range of the first conductance step, where the *0.7 anomaly* is frequently observed in experiments [37].

The 0.7 feature is a small anomalous plateau below the first conductance step at a value of around $0.7 \times G_0$. In the presence of an in-plane magnetic field the 0.7 feature evolves smoothly into the Zeeman spin-split plateau at $0.5 \times G_0$, and within a certain range the 0.7 plateau gets more pronounced with increasing temperature T. Experimentalists measure a shot noise suppression at the 0.7 plateau, and they find so-called 0.7 analogs at high magnetic fields.

On the theoretical side there are various approaches that describe different aspects of the 0.7 anomaly. They generally agree that interactions are responsible for this anomalous behavior of the conductance, however the actual mechanism is still controversial. Our model, though based on a simplified description of the interactions, is able to reproduce most of the relevant features observed in experiments. The computed conductance traces exhibit a shoulder below the first conductance step. We can reproduce the magnetic field behavior and we find a 0.7 analog structure at high magnetic fields. Moreover, the observed shot noise suppression is accounted for in our model. A drawback of our approach is, that it fails to reproduce the temperature dependence observed in experiments. In our results the 0.7 plateau is washed out and eventually vanishes with increasing T. Our findings are in agreement with various DFT results and support the phenomenological spin splitting model.

Mesoscopic devices in the nonlinear regime

The second part of this work is dedicated to the nonlinear transport regime. We introduce a way to account for the inter-particle interactions in Hartree approximation which corresponds to the classical Coulomb interaction between the electrons. This gives rise to an electrostatic potential $V_{\mathrm{es}}(\vec{x})$, which has to be determined self-consistently with the rearrangement of charges in the system. Employing a self-consistent numerical procedure we compute the current through a mesoscopic sample for a given external voltage V.

The systems under investigation are ballistic ratchet devices, that can produce a directed net current under a periodic AC driving with vanishing average bias [38–40]. We numerically investigate the transport properties of a triangular quantum dot ratchet. The sign and the magnitude of the obtained net current depends strongly on the external parameters like the driving amplitude and the chemical potential. This behavior is in line with the experimental observations.

Recently the idea of the ratchet mechanism was extended to so-called *spin ratchets*, which can create a net spin current if exposed to a periodic rocking [41–46]. So far the theoretical investigations made use of phenomenological models for the voltage drop throughout the system. In order to justify the heuristic models we shall extend the theoretical description to include the self-consistent electrostatic potential. The system we investigate is a double quantum dot acting as a resonant tunneling spin ratchet. Oppositely magnetized ferromagnetic stripes induce differently oriented magnetic fields in the two dots causing a spin splitting of the energy levels in the dots. By applying a voltage one can reach a resonant situation where the corresponding energy levels of the two dots are aligned, resulting in a large spin current. The obtained IV-characteristics of the device shows a resonant behavior of the net spin current, whereas the net charge current exactly vanishes for symmetry reasons.

Spin ratchet devices may find their application as "*spin batteries*" in the field of spintronics. As already mentioned the spin injection from ferromagnetic contacts into semiconducting materials is highly inefficient. Therefore it is desirable to create spin-polarized currents in a semiconductor. One possible realization of such a spin battery is based on spin pumps [47, 48], where the shape of a quantum dot is periodically modulated by two or more gates. An alternative realization is posed by spin ratchets, where a periodic external AC voltage is sufficient to create a net spin current.

Outline

The present work is structured as follows: after the general introduction we present the Green function formalism in Chapter 2, which is used throughout the thesis to compute the transport properties of mesoscopic devices. We outline the perturbation expansion to include interactions and sketch the steps towards the nonequilibrium Green function description. The general effective mass Hamiltonian describing the dynamics of electrons in a 2DEG is discretized and also the relations for the Green

functions are written down in matrix form. Finally we show how to extract the relevant physical observables from the system's Green functions.

Chapter 3 is dedicated to the description of transport through quantum point contacts in the presence of short-range electron-electron interactions. We start with an introduction to the present state of the experimental and theoretical knowledge about the 0.7 conductance anomaly and summarize the most common approaches in that field. After presenting our model we show the numerical results concerning spin splitting, the magnetic field dependence, the shot noise suppression and the temperature dependence of the 0.7 structure. We discuss the relation of our model to the case of realistic Coulomb interaction and present a section on transport of cold fermionic atoms.

In Chapter 4 we describe the procedure to find the self-consistent solution of the electrostatic potential in a biased nanosystem. It is based on a Newton-Raphson method, that improves the convergence behavior of the coupled system of equations for the charge density and the electrostatic potential. The chapter closes with an example of the potential drop in a quantum wire.

The self-consistent scheme to determine the potential drop is applied to ballistic quantum ratchets in Chapter 5. We investigate the transport properties of a triangular quantum dot charge ratchet and a resonant tunneling double-dot spin ratchet in the nonlinear regime. The net charge and spin current is computed in the presence of an unbiased periodic external driving.

In Chapter 6 the main results of this work are summarized and we suggest possibilities for further research activities in this field.

The Appendix contains a derivation of the self-energy for electron-electron interactions in Hartree-Fock approximation. The second part provides an analytic expression of the Green function of a semi-infinite lead. Finally, the recursive Green function method for the nonequilibrium situation is presented.

CHAPTER 2

Green function formalism for electronic transport

In this chapter we introduce the basic concepts that are used throughout this thesis to calculate transport properties of mesoscopic systems. We outline the well established Green function formalism and write down the relevant equations. The perturbation expansion of the Green functions for a system with electron-electron interactions is presented and it is shown how a nonequilibrium situation can be treated within the same formalism. We introduce the general Hamilton operator describing a two-dimensional electron system and discretize the Hamiltonian and the Green functions. At the end of the chapter we show how to extract the relevant physical observables from the Green functions of the system.

2.1 Basic definitions and properties

The usage of Green functions is one standard approach in transport theory of mesoscopic devices [23–29]. Knowing the relevant Green functions of a specific system one can easily compute most of the quantities of interest like the particle density, the density of states, the conductance or the current through the device. In this chapter we shall give an overview over the important properties of the various Green functions and write down some useful relations.

The Hamilton operators we want to consider are on the one hand the single particle Hamiltonian

$$H_0 = -\frac{\hbar^2}{2m}\vec{\nabla}^2 + U(\vec{x}) \tag{2.1}$$

describing noninteracting electrons in an external potential $U(\vec{x})$, and on the other hand the Hamiltonian for interacting particles

$$\mathcal{H} = H_0 + \mathcal{W}, \tag{2.2}$$

where $\mathcal{W}$ is the interaction Hamiltonian.

The Green functions are usually defined by means of the fermionic field operators

$$\begin{aligned} \hat{\Psi}^\dagger(\vec{x}) &= \sum_\alpha \phi_\alpha^*(\vec{x})\hat{a}_\alpha^\dagger \\ \hat{\Psi}(\vec{x}) &= \sum_\alpha \phi_\alpha(\vec{x})\hat{a}_\alpha, \end{aligned} \tag{2.3}$$

that create or annihilate an electron at position $\vec{x}$. Here, the $\phi_\alpha(\vec{x})$ form a complete set of orthonormal single particle wave functions, and $\hat{a}_\alpha^\dagger$ and $\hat{a}_\alpha$ are the creation and annihilation operators for the quantum state $|\phi_\alpha\rangle$. They fulfill the fermionic anti-commutation rules

$$\begin{aligned} \left\{\hat{a}_\alpha, \hat{a}_\beta^\dagger\right\} &= \delta_{\alpha,\beta} \\ \left\{\hat{a}_\alpha^\dagger, \hat{a}_\beta^\dagger\right\} &= \left\{\hat{a}_\alpha, \hat{a}_\beta\right\} = 0, \end{aligned} \tag{2.4}$$

where $\{A, B\} = AB + BA$ denotes the anti-commutator of the operators A and B. From Eq. (2.4) follows an equivalent relation for the field operators, reading

$$\begin{aligned} \left\{\hat{\Psi}(\vec{x}), \hat{\Psi}^\dagger(\vec{x}')\right\} &= \delta(\vec{x} - \vec{x}') \\ \left\{\hat{\Psi}^\dagger(\vec{x}), \hat{\Psi}^\dagger(\vec{x}')\right\} &= \left\{\hat{\Psi}(\vec{x}), \hat{\Psi}(\vec{x}')\right\} = 0. \end{aligned} \tag{2.5}$$

These relations also hold if the field operators are time dependent Heisenberg operators

$$\hat{\Psi}(\vec{x}, t) = \mathrm{e}^{\frac{\mathrm{i}}{\hbar}\mathcal{H}t}\,\hat{\Psi}(\vec{x})\,\mathrm{e}^{-\frac{\mathrm{i}}{\hbar}\mathcal{H}t}, \tag{2.6}$$

as long as the time arguments of both operators in the anti-commutator are identical. The time evolution is governed by the operator

$$\hat{U}(t) = \mathrm{e}^{-\frac{\mathrm{i}}{\hbar}\mathcal{H}t} \tag{2.7}$$

with the full Hamiltonian $\mathcal{H}$. Using the field operators (2.3) the Hamiltonian (2.2) can be written in the second quantized form [25, 27]

$$\begin{aligned}\mathcal{H} = &\int \mathrm{d}^3x\, \hat{\Psi}^\dagger(\vec{x}) \left[-\frac{\hbar^2}{2m}\vec{\nabla}^2 + U(\vec{x})\right] \hat{\Psi}(\vec{x}) + \\ &+ \int \mathrm{d}^3x \int \mathrm{d}^3x'\; \hat{\Psi}^\dagger(\vec{x})\hat{\Psi}^\dagger(\vec{x}')w(\vec{x},\vec{x}')\hat{\Psi}(\vec{x}')\hat{\Psi}(\vec{x}),\end{aligned} \tag{2.8}$$

where $w(\vec{x},\vec{x}')$ describes the interaction potential between particles at $\vec{x}$ and $\vec{x}'$.

In the absence of electron-electron interactions the field operators satisfy the time dependent Schrödinger equation

$$\mathrm{i}\hbar\frac{\partial}{\partial t}\hat{\Psi}(\vec{x},t) = H_0\hat{\Psi}(\vec{x},t). \tag{2.9}$$

This follows from the Hamiltonian H_0 in the second quantized form (2.8) after making use of the anti-commutation relations (2.5) and calculating the time derivative via the commutator

$$\mathrm{i}\hbar\frac{\partial}{\partial t}\hat{\Psi}(\vec{x},t) = \left[\hat{\Psi}(\vec{x},t), H_0\right]. \tag{2.10}$$

With these field operators it is now possible to define the time-ordered (or causal) single particle Green function at zero temperature by

$$\mathcal{G}(\vec{x},\vec{x}';t,t') = -\frac{\mathrm{i}}{\hbar}\frac{\langle\Phi_0|\hat{\mathrm{T}}\hat{\Psi}(\vec{x},t)\hat{\Psi}^\dagger(\vec{x}',t')|\Phi_0\rangle}{\langle\Phi_0|\Phi_0\rangle}. \tag{2.11}$$

Here, $\hat{\mathrm{T}}$ denotes the time-ordering operator, that rearranges the operator product in a way that the operator with the later time argument is to the left of the operator with the earlier time,

$$\hat{\mathrm{T}}A(t)B(t') = \Theta(t-t')A(t)B(t') - \Theta(t'-t)B(t')A(t). \tag{2.12}$$

The minus-sign is due to the anti-commuting nature of the fermionic operators A and B. The state $|\Phi_0\rangle$ in Eq. (2.11) denotes the exact ground state of the full Hamiltonian including interactions, Eq. (2.2). The above definition of the time-ordered Green function can be generalized to describe an equilibrium system at finite temperatures by

$$\mathcal{G}(\vec{x},\vec{x}';t,t') = -\frac{\mathrm{i}}{\hbar}\mathrm{Tr}\left\{\varrho\hat{\mathrm{T}}\hat{\Psi}(\vec{x},t)\hat{\Psi}^\dagger(\vec{x}',t')\right\} = -\frac{\mathrm{i}}{\hbar}\left\langle\hat{\mathrm{T}}\hat{\Psi}(\vec{x},t)\hat{\Psi}^\dagger(\vec{x}',t')\right\rangle. \tag{2.13}$$

The brackets $\langle \ldots \rangle$ denote a thermal average

$$\langle A \rangle = \mathrm{Tr}\{\varrho A\} \tag{2.14}$$

with the statistical operator ϱ. In a grand-canonical ensemble the statistical operator is given by

$$\varrho = \frac{\exp\left(-\beta(\mathcal{H} - \mu N)\right)}{\mathrm{Tr}\exp\left(-\beta(\mathcal{H} - \mu N)\right)}, \tag{2.15}$$

where $\beta = 1/(k_B T)$ is the inverse of the temperature T and the Boltzmann constant k_B, μ is the chemical potential, and N is number operator.

Besides the causal Green function it is common to define also the retarded, advanced, greater, and lesser function:

$$\mathcal{G}^r(\vec{x},\vec{x}';t,t') = -\frac{\mathrm{i}}{\hbar}\Theta(t-t')\left\langle\left\{\hat{\Psi}(\vec{x},t),\hat{\Psi}^\dagger(\vec{x}',t')\right\}\right\rangle \tag{2.16}$$

$$\mathcal{G}^a(\vec{x},\vec{x}';t,t') = \frac{\mathrm{i}}{\hbar}\Theta(t'-t)\left\langle\left\{\hat{\Psi}(\vec{x},t),\hat{\Psi}^\dagger(\vec{x}',t')\right\}\right\rangle \tag{2.17}$$

$$\mathcal{G}^>(\vec{x},\vec{x}';t,t') = -\frac{\mathrm{i}}{\hbar}\left\langle\hat{\Psi}(\vec{x},t)\hat{\Psi}^\dagger(\vec{x}',t')\right\rangle \tag{2.18}$$

$$\mathcal{G}^<(\vec{x},\vec{x}';t,t') = \frac{\mathrm{i}}{\hbar}\left\langle\hat{\Psi}^\dagger(\vec{x}',t')\hat{\Psi}(\vec{x},t)\right\rangle, \tag{2.19}$$

where $\Theta(t)$ is the Heaviside step-function. Within this thesis we are mostly concerned with the retarded Green function (2.16) and the lesser function (2.19), as those objects determine the physical quantities of interest, see also Sec. 2.5. If we calculate the time derivative of the retarded Green function of a noninteracting system,

$$\begin{aligned}\mathrm{i}\hbar\frac{\partial}{\partial t}\mathcal{G}_0^r(\vec{x},\vec{x}';t,t') = {}& \delta(t-t')\left\langle\left\{\hat{\Psi}(x,t),\hat{\Psi}^\dagger(x',t')\right\}\right\rangle \\ & - \frac{\mathrm{i}}{\hbar}\Theta(t-t')\left\langle\left\{\mathrm{i}\hbar\frac{\partial}{\partial t}\hat{\Psi}(x,t),\hat{\Psi}^\dagger(x',t')\right\}\right\rangle,\end{aligned} \tag{2.20}$$

using Eqs. (2.5) and (2.9) we find that it obeys the inhomogeneous Schrödinger equation

$$\left[\mathrm{i}\hbar\frac{\partial}{\partial t} - H_0\right]\mathcal{G}_0^r(\vec{x},\vec{x}';t,t') = \delta(t-t')\delta(\vec{x}-\vec{x}'). \tag{2.21}$$

The subscript '0' in the Green function indicates that it refers to a noninteracting system described by the Hamilton operator H_0, as defined in Eq. (2.1).

For a system in a stationary state the Green functions only depend on time differences $\tau = t - t'$ [25, 26]. Therefore it is possible to perform a Fourier transformation and work with the Green function in the energy domain

$$\mathcal{G}(\vec{x},\vec{x}';E) = \int \mathrm{d}\tau\, \mathrm{e}^{\frac{\mathrm{i}}{\hbar}E\tau}\mathcal{G}(\vec{x},\vec{x}';\tau). \tag{2.22}$$

In order to transform Eq. (2.21) let us consider

$$\begin{aligned} H_0\mathcal{G}_0^r(\vec{x},\vec{x}';E) &= \int \mathrm{d}\tau\, \mathrm{e}^{\frac{\mathrm{i}}{\hbar}E\tau} H_0\mathcal{G}_0^r(\vec{x},\vec{x}';\tau) \\ &= \int \mathrm{d}\tau\, \mathrm{e}^{\frac{\mathrm{i}}{\hbar}(E+\mathrm{i}\eta)\tau} \left[\mathrm{i}\hbar\frac{\partial}{\partial\tau}\mathcal{G}_0^r(\vec{x},\vec{x}';\tau) - \delta(\tau)\delta(\vec{x}-\vec{x}')\right], \end{aligned} \tag{2.23}$$

where we made use of Eq. (2.21) and added an infinitesimal positive imaginary part $\mathrm{i}\eta$ to the energy for convergence reasons. After integrating Eq. (2.23) by parts we find

$$\big[E - H_0 + \mathrm{i}\eta\big]\mathcal{G}_0^r(\vec{x},\vec{x}';E) = \delta(\vec{x}-\vec{x}'). \tag{2.24}$$

It is straightforward to verify that the eigenfunction representation of the Green function [23]

$$\mathcal{G}_0^r(\vec{x},\vec{x}';E) = \sum_\alpha \frac{\psi_\alpha(\vec{x})\psi_\alpha^*(\vec{x}')}{E-\epsilon_\alpha+\mathrm{i}\eta} \quad \text{with} \quad H_0\psi_\alpha(\vec{x}) = \epsilon_\alpha\psi_\alpha(\vec{x}) \tag{2.25}$$

fulfills the inhomogeneous Schrödinger equation (2.24).

From the definitions of the Green functions (2.13) and (2.16) – (2.19) it follows that they are not independent, but obey the relations

$$\begin{aligned} &\mathcal{G}^r = [\mathcal{G}^a]^\dagger, \\ &\mathcal{G}^r - \mathcal{G}^a = \mathcal{G}^> - \mathcal{G}^<, \\ &\mathcal{G}^r = \mathcal{G} - \mathcal{G}^<. \end{aligned} \tag{2.26}$$

Moreover, in thermal equilibrium the dissipation-fluctuation theorem [25, 26] is valid,

$$\mathcal{G}^<(\vec{x},\vec{x}';E) = \mathrm{i}f(E,\mu)A(\vec{x},\vec{x}';E). \tag{2.27}$$

It connects the lesser Green function with the spectral function

$$A(\vec{x},\vec{x}';E) = \mathrm{i}\left[\mathcal{G}^r(\vec{x},\vec{x}';E) - \mathcal{G}^a(\vec{x},\vec{x}';E)\right] = \mathrm{i}\left[\mathcal{G}^>(\vec{x},\vec{x}';E) - \mathcal{G}^<(\vec{x},\vec{x}';E)\right] \tag{2.28}$$

through the Fermi-Dirac distribution

$$f(E,\mu) = \frac{1}{\mathrm{e}^{\beta(E-\mu)}+1} \tag{2.29}$$

with chemical potential μ. The diagonal elements ($\vec{x}=\vec{x}'$) of $\mathcal{G}^<$ are related to the particle density and A is related to the density of states, see Eqs. (2.116) and (2.105) in Sec. 2.5. Thus the dissipation-fluctuation theorem has an illustrative interpretation: the particle density is given by filling up the density of states according to the Fermi function.

2.2 Perturbation expansion of the Green function

In the definition of the Green function, Eq. (2.11), the exact ground state $|\Phi_0\rangle$ of the interacting system enters, which we usually do not know. To avoid this problem it is favorable to treat the interaction as a time-dependent perturbation of the system

$$\mathcal{H}(t) = H_0 + \mathcal{W}(t). \tag{2.30}$$

One assumes that the interaction was adiabatically switched on in the past and will be switched off again, such that $\mathcal{W}(t) = 0$ for $t \to \pm\infty$. This allows us to express the Green function in terms of the ground state of H_0 and to include the interaction in a perturbative way.

For the following derivations one carefully has to distinguish between different representations of the operators and states, which we will mark with the appropriate subscripts throughout this section. In the Schrödinger representation the operators A_S are time-independent and the states evolve in time. The time evolution operators are obtained by writing the Schrödinger equation in an integral form

$$|\psi(t)\rangle_S = |\psi(0)\rangle_S - \frac{\mathrm{i}}{\hbar}\int_0^t \mathrm{d}t'\ \mathcal{H}(t')|\psi(t')\rangle_S. \tag{2.31}$$

An iterative solution of (2.31) leads to [26, 27]

$$|\psi(t)\rangle_S = \hat{\mathtt{T}}\exp\left[-\frac{\mathrm{i}}{\hbar}\int_0^t \mathrm{d}t'\ \mathcal{H}(t')\right]|\psi(0)\rangle_S \tag{2.32}$$

so that the time-evolution is governed by the operator

$$\hat{U}(t) = \hat{\mathtt{T}}\exp\left[-\frac{\mathrm{i}}{\hbar}\int_0^t \mathrm{d}t'\ \mathcal{H}(t')\right]. \tag{2.33}$$

The time-ordering operator $\hat{\mathtt{T}}$ is essential as Hamiltonians with different time arguments do not necessarily commute, in contrast to Eq. (2.7). To describe the time evolution of a quantum state from time t' to time t one introduces the S-matrix

$$S(t,t') = \hat{U}(t)\hat{U}^\dagger(t'), \tag{2.34}$$

so that $|\psi(t)\rangle_S = \hat{U}(t)|\psi(0)\rangle_S = \hat{U}(t)\hat{U}^\dagger(t')|\psi(t')\rangle_S = S(t,t')|\psi(t')\rangle_S$.

Besides the Schrödinger picture we can as well describe the system within the Heisenberg representation, where the states are time-independent $|\phi\rangle_H = |\phi(0)\rangle_S$. The full time dependence is incorporated in the operators that evolve with

$$A_H(t) = \hat{U}^\dagger(t)A_S\hat{U}(t) \tag{2.35}$$

with $\hat{U}(t)$ given in Eq. (2.33).

The interaction representation lets the operators evolve with the noninteracting part of the Hamiltonian

$$A_I(t) = \mathrm{e}^{\frac{\mathrm{i}}{\hbar}H_0 t} A_S \, \mathrm{e}^{-\frac{\mathrm{i}}{\hbar}H_0 t}. \tag{2.36}$$

Correspondingly, the states develop according to

$$|\psi(t)\rangle_I = \mathrm{e}^{\frac{\mathrm{i}}{\hbar}H_0 t}|\psi(t)\rangle_S = \mathrm{e}^{\frac{\mathrm{i}}{\hbar}H_0 t}\hat{U}(t)|\psi(0)\rangle_S = \hat{U}_I(t)|\psi(0)\rangle_S. \tag{2.37}$$

The Schrödinger equation for the states in interaction representation reads [25–27]

$$\mathrm{i}\hbar\frac{\partial}{\partial t}|\psi(t)\rangle_I = \mathcal{W}_I(t)|\psi(t)\rangle_I. \tag{2.38}$$

In analogy to Eq. (2.32) the time evolution of $|\psi(t)\rangle_I$ is determined by $\mathcal{W}_I(t)$ in the exponential and the S-matrix is given by

$$\begin{aligned} S_I(t,t') &= \hat{\mathtt{T}} \exp\left[-\frac{\mathrm{i}}{\hbar}\int\limits_{t'}^{t} \mathrm{d}t_1 \, \mathcal{W}_I(t_1)\right] \\ &= 1 + \frac{-\mathrm{i}}{\hbar}\int\limits_{t'}^{t} \mathrm{d}t_1 \, \mathcal{W}_I(t_1) + \left(\frac{-\mathrm{i}}{\hbar}\right)^2 \int\limits_{t'}^{t} \mathrm{d}t_1 \int\limits_{t'}^{t_1} \mathrm{d}t_2 \, \mathcal{W}_I(t_1)\mathcal{W}_I(t_2) + \ldots \end{aligned} \tag{2.39}$$

Having defined the S-matrix we can now rewrite the numerator of the causal Green function, Eq. (2.11), in terms of field operators in interaction representation

$$\begin{aligned} &{}_H\langle\Phi_0|\hat{\mathtt{T}}\,\hat{\Psi}_H(\vec{x},t)\hat{\Psi}^\dagger_H(\vec{x}',t')|\Phi_0\rangle_H = \\ &{}_H\langle\Phi_0|\hat{\mathtt{T}}\,\hat{U}^\dagger(t)\mathrm{e}^{-\frac{\mathrm{i}}{\hbar}H_0 t}\hat{\Psi}_I(\vec{x},t)\mathrm{e}^{\frac{\mathrm{i}}{\hbar}H_0 t}\hat{U}(t)\hat{U}^\dagger(t')\mathrm{e}^{-\frac{\mathrm{i}}{\hbar}H_0 t'}\hat{\Psi}^\dagger_I(\vec{x}',t')\mathrm{e}^{\frac{\mathrm{i}}{\hbar}H_0 t'}\hat{U}(t')|\Phi_0\rangle_H = \\ &{}_I\langle\Phi_0(t)|\hat{\mathtt{T}}\,\hat{\Psi}_I(\vec{x},t)S_I(t,t')\hat{\Psi}^\dagger_I(\vec{x}',t')|\Phi_0(t')\rangle_I, \end{aligned} \tag{2.40}$$

where we made use of Eqs. (2.35) – (2.37) in order to transform the expressions from Heisenberg to interaction representation. The next step is to take the time arguments at which the states $|\Phi_0(t)\rangle_I$ are evaluated to $\pm\infty$, respectively, where all particle-particle interactions are assumed to be absent. Hence, we replace $|\Phi_0(t')\rangle_I$ by $S_I(t',-\infty)|\Phi_0(-\infty)\rangle_I$ and ${}_I\langle\Phi_0(t)|$ by ${}_I\langle\Phi_0(\infty)|S_I(\infty,t)$, which does not change the overall expectation value of (2.40), according to the Gell-Mann and Low theorem [28, 49]. The states $|\Phi_0(-\infty)\rangle_I$ are given by the ground state $|0\rangle$ of the noninteracting Hamiltonian H_0. After switching on and off the interaction, the system finally ends up in the same state $|0\rangle$ at $t = +\infty$, apart from a possible phase factor which is cancelled by the same phase factor in the denominator. Therefore the final expression for the causal Green function is

$$\mathcal{G}(\vec{x},\vec{x}';t,t') = -\frac{\mathrm{i}}{\hbar}\frac{\langle 0|\hat{\mathtt{T}}S_I(\infty,-\infty)\hat{\Psi}_I(\vec{x},t)\hat{\Psi}^\dagger_I(\vec{x}',t')|0\rangle}{\langle 0|S_I(\infty,-\infty)|0\rangle}, \tag{2.41}$$

with $|0\rangle$ being the ground state of H_0. Expanding the S-matrix in the numerator and the denominator according to Eq. (2.39) leads to a perturbation expansion of the time-ordered Green function $\mathcal{G}$. If we insert the interaction Hamiltonian in second quantized form, see Eq. (2.8), the numerator yields

$$\begin{aligned}&\left\langle 0 \left| \hat{\mathtt{T}}\, \hat{\Psi}(\vec{x},t)\hat{\Psi}^\dagger(\vec{x}',t') \right| 0 \right\rangle + \left(-\frac{\mathrm{i}}{\hbar}\right)\frac{1}{2}\int \mathrm{d}^3x_1 \int \mathrm{d}^3x_1' \int \mathrm{d}t_1\; w(\vec{x}_1,\vec{x}_1') \times \\ &\times \left\langle 0 \left| \hat{\mathtt{T}}\, \hat{\Psi}^\dagger(\vec{x}_1,t_1)\hat{\Psi}^\dagger(\vec{x}_1',t_1)\hat{\Psi}(\vec{x}_1',t_1)\hat{\Psi}(\vec{x}_1,t_1)\hat{\Psi}(\vec{x},t)\hat{\Psi}^\dagger(\vec{x}',t') \right| 0 \right\rangle + \ldots\end{aligned} \tag{2.42}$$

Henceforth we will omit the subscripts distinguishing the different representations as all operators are to be taken in interaction representation. So the task is to calculate the expectation value of multiple products of field operators. This is allowed for by Wick's theorem [27, 28, 50], which states that the expectation value of a time-ordered product of field operators may be rewritten into a sum of all possible contractions

$$\underbrace{\hat{\Psi}_1\hat{\Psi}_2} = \hat{\mathtt{T}}\;\hat{\Psi}_1\hat{\Psi}_2 - \hat{\mathtt{N}}\;\hat{\Psi}_1\hat{\Psi}_2. \tag{2.43}$$

Here, $\hat{\mathtt{N}}$ denotes the normal-ordering operator that moves all annihilation operators to the right of the creation operators. The contraction $\underbrace{\hat{\Psi}_1\hat{\Psi}_2}$ is only non-zero if it contains both a creation and an annihilation operator. It is related to the free Green function by

$$\left\langle \underbrace{\hat{\Psi}(\vec{x}_1,t_1)\hat{\Psi}^\dagger(\vec{x}_2,t_2)} \right\rangle = \left\langle \hat{\mathtt{T}}\;\hat{\Psi}(\vec{x}_1,t_1)\hat{\Psi}^\dagger(\vec{x}_2,t_2) \right\rangle = \mathrm{i}\hbar\mathcal{G}_0(\vec{x}_1,\vec{x}_2;t_1,t_2), \tag{2.44}$$

therefore the full Green function (2.41) can be written in terms of unperturbed Green functions. In addition, the cancellation theorem [26–28] ensures that the denominator in Eq. (2.41) exactly cancels the *disconnected diagrams* of the numerator, which are those terms without any contraction between the field operators of the interaction Hamiltonian and the original points $(\vec{x},t)$ and $(\vec{x}',t')$. Hence the Green function is given by the sum of all possible *connected* contractions of the numerator of Eq. (2.41). This is expressed by the Dyson equation [26–28]

$$\begin{aligned}\mathcal{G}(\vec{x},\vec{x}';t,t') &= \mathcal{G}_0(\vec{x},\vec{x}';t,t') + \\ &+ \int \mathrm{d}^3x_1\mathrm{d}t_1 \int \mathrm{d}^3x_2\mathrm{d}t_2\; \mathcal{G}_0(\vec{x},\vec{x}_1;t,t_1)\Sigma_{\mathrm{int}}(\vec{x}_1,\vec{x}_2;t_1,t_2)\mathcal{G}(\vec{x}_2,\vec{x}';t_2,t').\end{aligned} \tag{2.45}$$

The self-energy $\Sigma_{\mathrm{int}}(\vec{x}_1,\vec{x}_2;t_1,t_2)$ can be identified by explicitly writing down the perturbation expansion like in Eq. (2.42), which is done in Appendix A for the first order of the expansion. The Dyson equation is often represented by Feynman diagrams

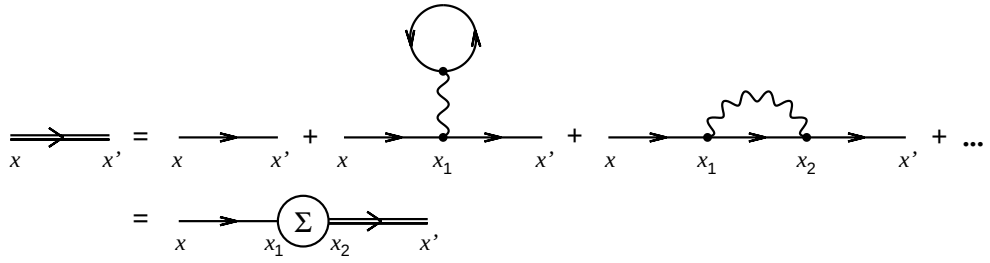

where a solid line indicates a free Green function, a double line represents the full Green function, and the wavy lines display the particle-particle interactions. The graphs shown here correspond to the first order of the perturbation expansion which is known as the Hartree-Fock approximation.

In steady-state problems the Green functions depend only on time differences $t - t'$ and the Dyson equation can be Fourier transformed to yield

$$\mathcal{G}(\vec{x}, \vec{x}'; E) = \mathcal{G}_0(\vec{x}, \vec{x}'; E) + \int \mathrm{d}^3 x_1 \int \mathrm{d}^3 x_2 \; \mathcal{G}_0(\vec{x}, \vec{x}_1; E) \Sigma_{\mathrm{int}}(\vec{x}_1, \vec{x}_2; E) \mathcal{G}(\vec{x}_2, \vec{x}'; E). \tag{2.46}$$

If the interaction is instantaneous, as considered within this thesis, the self-energy acquires an additional delta function $\delta(t_1 - t_2)$ in the time-domain. In that case the Fourier transformed interaction self-energy does not depend on the energy,

$$\begin{aligned} \Sigma_{\mathrm{int}}(\vec{x}_1, \vec{x}_2) &= \int \mathrm{d}(t_1 - t_2) \, \mathrm{e}^{\frac{\mathrm{i}}{\hbar} E'(t_1 - t_2)} \Sigma_{\mathrm{int}}(\vec{x}_1, \vec{x}_2; t_1 - t_2) \, \delta(t_1 - t_2) = \\ &= \Sigma_{\mathrm{int}}(\vec{x}_1, \vec{x}_2; 0). \end{aligned} \tag{2.47}$$

2.3 Nonequilibrium Green functions

In the preceding sections we defined various Green functions which are in equilibrium connected through the relations (2.26) and (2.27). Hence, in principle everything can be expressed by the retarded Green function only. This is, however, not the case in a nonequilibrium situation [52, 53], as the dissipation-fluctuation theorem (2.27) does not hold any more. The reason is that the electrons in a biased system are not distributed according to a Fermi function. If the system is equally populated by particles from a left and a right contact with chemical potentials μ_L and μ_R, respectively, then the correct distribution function is a two-step function $[f(E, \mu_L) + f(E, \mu_R)]/2$, as displayed in Fig. 2.1.

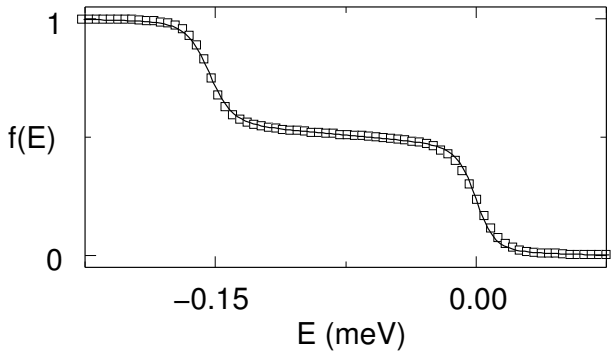

Figure 2.1: Experimentally measured distribution function of a wire biased with $V = 0.15\,\mathrm{mV}$, from [51].

Moreover, the perturbation expansion of the time-ordered Green function (2.41) cannot be generalized in a straight forward way to the nonequilibrium case, as the states at $t = +\infty$ and $t = -\infty$ are not identical. So instead of evolving the state $|0\rangle$ from $t = -\infty$ through t and t' to ∞, it is convenient to go back to $t = -\infty$ to end up in the same state $|0\rangle$. The time evolution therefore is taken along the Keldysh contour C sketched in Fig. 2.2. The time t' is smaller than t on the real time axis, but in the

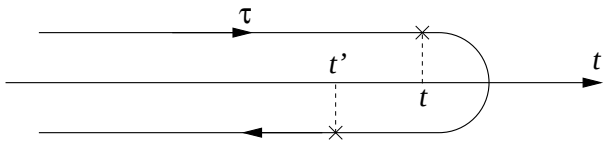

Figure 2.2: The Keldysh contour C.

contour sense $t <_C t'$ in that particular example. The contour-ordering operator

$$\hat{\mathrm{T}}_C A(t)B(t') = \begin{cases} A(t)B(t') & \text{for } t >_C t' \\ -B(t')A(t) & \text{for } t <_C t' \end{cases} \tag{2.48}$$

rearranges the fermion operators such that the operator with the later time argument (in the contour sense) is on the left. The contour-ordered Green function is defined by

$$\mathcal{G}^C(\vec{x},\vec{x}';t,t') = -\frac{\mathrm{i}}{\hbar}\left\langle \hat{\mathrm{T}}_C \hat{\Psi}(\vec{x},t)\hat{\Psi}^\dagger(\vec{x}',t')\right\rangle . \tag{2.49}$$

There are four different possibilities of assigning the times t and t' to the upper (C_1) or lower (C_2) branch of the Keldysh contour, leading to

$$\mathcal{G}^C(\vec{x},\vec{x}';t,t') = \begin{cases} \mathcal{G}(\vec{x},\vec{x}';t,t') & \text{for } t,t' \in C_1 \\ \mathcal{G}^{\bar{t}}(\vec{x},\vec{x}';t,t') & \text{for } t,t' \in C_2 \\ \mathcal{G}^{>}(\vec{x},\vec{x}';t,t') & \text{for } t \in C_2, t' \in C_1 \\ \mathcal{G}^{<}(\vec{x},\vec{x}';t,t') & \text{for } t \in C_1, t' \in C_2. \end{cases} \tag{2.50}$$

Hence, $\mathcal{G}^C$ incorporates the time-ordered Green function (2.13), the anti time-ordered function $\mathcal{G}^{\bar{t}}$, the greater (2.18), and lesser (2.19) Green function.

It is possible to show [25–28, 52] that the contour-ordered Green function possesses a perturbation expansion analogous to (2.42) but with time arguments lying on the contour C. Hence, it plays the same role as the time-ordered Green function in the equilibrium theory. In particular it satisfies the Dyson equation

$$\begin{aligned} \mathcal{G}^C(\vec{x},\vec{x}';t,t') &= \mathcal{G}_0^C(\vec{x},\vec{x}';t,t') + \\ &+ \int \mathrm{d}^3x_1\mathrm{d}^3x_2 \int_C \mathrm{d}\tau_1\mathrm{d}\tau_2\; \mathcal{G}_0^C(\vec{x},\vec{x}_1;t,\tau_1)\Sigma_{\mathrm{int}}(\vec{x}_1,\vec{x}_2;\tau_1,\tau_2)\mathcal{G}^C(\vec{x}_2,\vec{x}';\tau_2,t') \end{aligned} \tag{2.51}$$

where the time integrals have to be performed along the Keldysh contour. The appearing contour integrals are of the form

$$\begin{aligned} D(t,t') &= \int_C \mathrm{d}\tau A(t,\tau)B(\tau,t'), \\ E(t,t') &= \int_C \mathrm{d}\tau_1 \int_C \mathrm{d}\tau_2 A(t,\tau_1)B(\tau_1,\tau_2)C(\tau_2,t'), \end{aligned} \tag{2.52}$$

and can be rewritten in real-time integrals using the Langreth rules [25]:

$$D^{r(a)}(t,t') = \int \mathrm{d}t_1 A^{r(a)}(t,t_1)B^{r(a)}(t_1,t) \tag{2.53a}$$

$$D^{<}(t,t') = \int \mathrm{d}t_1 \left[A^{r}(t,t_1)B^{<}(t_1,t) + A^{<}(t,t_1)B^{a}(t_1,t)\right] \tag{2.53b}$$

$$E^{r(a)}(t,t') = \int \mathrm{d}t_1 \int \mathrm{d}t_2 A^{r(a)}(t,t_1)B^{r(a)}(t_1,t_2)C^{r(a)}(t_2,t') \tag{2.53c}$$

$$E^{<}(t,t') = \int \mathrm{d}t_1 \int \mathrm{d}t_2 \left[A^{r}B^{r}C^{<} + A^{r}B^{<}C^{a} + A^{<}B^{a}C^{a}\right]. \tag{2.53d}$$

Applying the Langreth rule (2.53c) we recover the Dyson equation for the retarded Green function, which can be Fourier transformed to

$$\mathcal{G}^r(\vec{x},\vec{x}';E) = \mathcal{G}_0^r(\vec{x},\vec{x}';E) + \int \mathrm{d}^3x_1 \int \mathrm{d}^3x_2\, \mathcal{G}_0^r(\vec{x},\vec{x}_1;E)\Sigma_{\mathrm{int}}(\vec{x}_1,\vec{x}_2;E)\mathcal{G}^r(\vec{x}_2,\vec{x}';E). \tag{2.54}$$

After employing the Langreth rule (2.53d) the Dyson equation for the contour ordered Green function, Eq. (2.51), yields the so-called kinetic equation [25, 27]

$$\mathcal{G}^<(\vec{x},\vec{x}';E) = \int \mathrm{d}^3x_1 \int \mathrm{d}^3x_2\, \mathcal{G}^r(\vec{x},\vec{x}_1;E)\Sigma^<(\vec{x}_1,\vec{x}_2;E)\mathcal{G}^a(\vec{x}_2,\vec{x}';E). \tag{2.55}$$

The kinetic equation a priori consists of more than the one term shown in Eq. (2.55), see [25]. However, the additional terms that were left out contain information about the initial state before the interaction was turned on, which can usually be neglected in steady-state problems [54]. The lesser self-energy $\Sigma^<(\vec{x}_1,\vec{x}_2;E)$ has to be identified from the explicit perturbation expansion of the S-matrix, see Appendix A, after applying the Langreth rules. In Hartree-Fock approximation the lesser self-energy due to interactions vanishes [23], and the only contributions to $\Sigma^<(\vec{x}_1,\vec{x}_2;E)$ come from the coupling to the leads, see Eq. (2.102).

In conclusion, the contour-ordered Green function was introduced in order to apply the standard formalism, which was established for equilibrium Green functions, also to nonequilibrium problems. It possesses a perturbation expansion and obeys the Dyson equation (2.51) involving contour integrals. For practical purposes one can convert the contour integrals into real-time integrals using the Langreth rules, Eq. (2.53). Thus

one obtains an ordinary Dyson equation for the retarded Green function, Eq. (2.54), and the kinetic equation (2.55) for the lesser function. Those two equations are the central relations to describe the steady-state properties of a nonequilibrium system. We will show in Chapters 3 and 4 how to apply them in order to obtain the interaction potentials and the transport properties of a mesoscopic device.

2.4 Discretization of the system

2.4.1 Dimensionless quantities

The systems we are interested in are two-dimensional electron gases, where all the dynamics takes place within a single plane. For numerical purposes we discretize the spatial coordinates according to Fig. 2.3 to obtain a square grid in the (x, z)-plane with lattice constant a. From here on $\vec{r} = (x, z)$ denotes a vector within the plane of the two-dimensional electron gas (2DEG), whereas three-dimensional vectors are represented by $\vec{x} = (x, y, z)$. The grid points $\vec{r}_j$ are labeled with an index $j = 1 \dots N$ and all functions of the spatial coordinates are evaluated at the mesh points, so that a function $f(\vec{r})$ is represented by a vector with components

$$f_j = f(\vec{r}_j). \tag{2.56}$$

We refer to neighboring lattice sites with the notation

$$f_{j+\hat{x}} = f(\vec{r}_j + a\hat{x}) \text{ and } f_{j+\hat{z}} = f(\vec{r}_j + a\hat{z}), \tag{2.57}$$

where $\hat{x}$ and $\hat{z}$ are the unit vectors in x- and z-direction, respectively. Hence, $j + \hat{x}$ labels the site next to site j in x-direction and $j + \hat{z}$ is the adjacent site in z-direction. The spatial derivatives are then written as finite differences of a function evaluated at neighboring sites

$$\begin{aligned} \frac{\partial f_j}{\partial x} &= \frac{1}{2a}\Big[f_{j+\hat{x}} - f_{j-\hat{x}}\Big] + \mathcal{O}(a^2) = \frac{1}{a}\Big[f_{j+\hat{x}/2} - f_{j-\hat{x}/2}\Big] + \mathcal{O}(a^2) \\ \frac{\partial^2 f_j}{\partial x^2} &= \frac{1}{a^2}\Big[f_{j+\hat{x}} - 2f_j + f_{j-\hat{x}}\Big] + \mathcal{O}(a^2). \end{aligned} \tag{2.58}$$

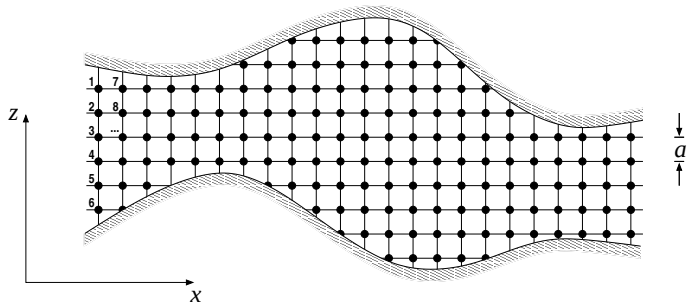

Figure 2.3: Sketch of the discretization of a two-dimensional system with lattice constant a.

In the continuum limit $a \to 0$ the differences evolve into the exact derivatives. Analog expressions are valid for the derivatives in z-direction. Moreover we can approximate a function by the mean value of the function at two neighboring sites

$$f_j = \frac{1}{2}\Big[f_{j+\hat{x}} + f_{j-\hat{x}}\Big] + \mathcal{O}(a^2) = \frac{1}{2}\Big[f_{j+\hat{x}/2} + f_{j-\hat{x}/2}\Big] + \mathcal{O}(a^2). \tag{2.59}$$

It is convenient to introduce dimensionless units for the numerical calculations. Therefore we refer to distances in units of the lattice constant a. The magnetic field is measured in units of $\phi_0/(2\pi a^2)$, where $\phi_0 = h/e$ is the magnetic flux quantum, and the energies are normalized to $\kappa = \hbar^2/(2ma^2)$:

$$\begin{aligned} x &= a\tilde{x}, z = a\tilde{z} \\ B &= \frac{\phi_0}{2\pi a^2}\widetilde{B} \\ E &= \frac{\hbar^2}{2ma^2}\widetilde{E} = \kappa\widetilde{E}. \end{aligned} \tag{2.60}$$

All dimensionless variables are marked by a tilde. The wave functions are also rescaled in lattice representation according to

$$\widetilde{\psi}_j = a\psi(\vec{r}_j). \tag{2.61}$$

The normalization for those lattice wave function reads

$$\sum_{j=1}^{N} |\widetilde{\psi}_j|^2 = \frac{1}{a^2}\sum_{j=1}^{N} a^2|\widetilde{\psi}_j|^2 \quad \underset{a\to 0}{\longrightarrow} \quad \frac{1}{a^2}\int \mathrm{d}^2 r\, |\widetilde{\psi}_j|^2 = \int \mathrm{d}^2 r\, |\psi(\vec{r}_j)|^2 = 1. \tag{2.62}$$

Moreover, the energy dispersion relation of a free particle changes in the discrete description. It can be obtained by inserting a plane wave $\psi(\vec{r}) = \exp(\mathrm{i}k_x x + \mathrm{i}k_z z)$ into the Schrödinger equation with the discretized kinetic Hamiltonian, Eq. (2.75) of the following subsection, yielding.

$$E\psi(\vec{r}) = \left[4\kappa - \kappa \mathrm{e}^{\mathrm{i}k_x a} - \kappa \mathrm{e}^{-\mathrm{i}k_x a} - \kappa \mathrm{e}^{\mathrm{i}k_z a} - \kappa \mathrm{e}^{-\mathrm{i}k_z a}\right]\psi(\vec{r}) \tag{2.63}$$

So the dispersion relation is

$$E = 2\kappa(1 - \cos k_x a) + 2\kappa(1 - \cos k_z a), \tag{2.64}$$

which evolves to the convenient expression $E = \hbar^2(k_x^2 + k_y^2)/(2m)$ in the continuum limit $a \to 0$. Hence, for an accurate description we have to ensure that $E \ll \kappa$. Another important quantity of interest is the particle density $n(\vec{r})$, which is rescaled to

$$\tilde{n}_j = a^2 n(\vec{r}_j). \tag{2.65}$$

The dimensionless Green functions are matrices with elements

$$\widetilde{\mathcal{G}}_{i,j}(E) = a^2\kappa\mathcal{G}(\vec{r}_i, \vec{r}_j; E), \tag{2.66}$$

and the Dirac delta function changes to a Kronecker symbol

$$\delta(\vec{r}_i - \vec{r}_j) \longrightarrow \frac{1}{a^2}\delta_{i,j} \tag{2.67}$$

in the discrete representation. After these considerations it is now possible to rewrite the Hamilton operator in matrix form and give the relevant expressions for the Green functions in a discretized notation.

2.4.2 The Hamiltonian

The systems we consider within this thesis are based on semiconductor heterostructures where a two-dimensional electron gas (2DEG) forms at the interface between different materials, e.g. GaAs and AlGaAs. The discontinuity of the band structure at the interface creates a strong lateral confinement potential, giving rise to quantized energy levels for the motion along the y-direction. At temperatures close to zero only the first subband is occupied, so that the electrons effectively move in a two-dimensional plane which will be the (x, z)-plane in our coordinate system. By additional gating or etching, the in-plane movement of the particles can be controlled and arbitrary device geometries can be realized [4], like for instance a quantum point contact [6, 7] shown in Fig. 3.1 of the next chapter.

We describe such a system by a *device*-region which is coupled to a left and right contact by leads [23], as sketched in Fig. 2.4. We assume that electron-electron interactions and external fields are only present inside the device. The leads are regarded as ideal conductors with no effective inter-particle interactions. This is approximately fulfilled if the particle density in the leads is sufficiently high, so that on the one hand the interactions are screened, and on the other hand the kinetic energy dominates over the interaction energy. The contacts serve as reservoirs that provide and absorb electrons. All energy relaxation and equilibration processes take place exclusively inside the contacts. They are in thermal equilibrium and can be characterized by a temperature T and a chemical potential μ. The leads in our model are taken to be infinitely long so that the contacts enter only through the Fermi-Dirac distribution function $f(E, \mu)$, that defines the occupation of the states in the leads.

The effective two-dimensional single-particle Hamiltonian for noninteracting electrons with charge $-e$ in a magnetic field $\vec{B}(\vec{r})$ and an external confinement potential

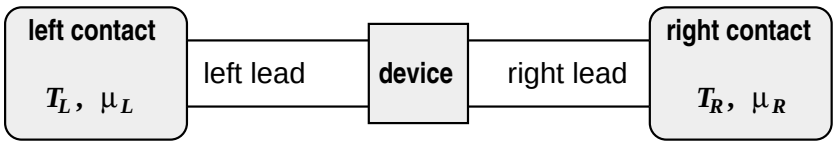

Figure 2.4: A device connected to two contacts via leads. The contacts are characterized by the temperature $T_{L(R)}$ and the chemical potential $\mu_{L(R)}$.

$U(\vec{r})$ is given by [55]

$$H_0 = \frac{1}{2m}\left[-\mathrm{i}\hbar\vec{\nabla} + e\vec{A}(\vec{r})\right]^2 + U(\vec{r}) + \frac{1}{2}g\mu_B\vec{B}(\vec{r})\cdot\vec{\sigma}. \tag{2.68}$$

Here, m is the effective electron mass, g is the material specific gyromagnetic ratio, $\mu_B = e\hbar/(2m_0)$ is the Bohr magneton with m_0 being the bare electron mass, and $\vec{\sigma}$ is the vector of Pauli matrices

$$\sigma_x = \begin{pmatrix} 0 & 1 \\ 1 & 0 \end{pmatrix}, \quad \sigma_y = \begin{pmatrix} 0 & -\mathrm{i} \\ \mathrm{i} & 0 \end{pmatrix}, \quad \sigma_z = \begin{pmatrix} 1 & 0 \\ 0 & -1 \end{pmatrix}. \tag{2.69}$$

The magnetic field $\vec{B}(\vec{r})$ is the related to the vector potential $\vec{A}(\vec{r})$ through

$$\vec{B}(\vec{r}) = \vec{\nabla}\times\vec{A}(\vec{r}). \tag{2.70}$$

As a first step let us discretize the kinetic part of the Hamiltonian (2.68). To do so we analyze how the kinetic Hamiltonian acts on a wave function $\psi(\vec{r}_j)$ after rewriting the derivatives by means of Eq. (2.58)

$$\begin{aligned}
H_{\mathrm{kin}}\psi_j &= \frac{1}{2m}\left[-\mathrm{i}\hbar\vec{\nabla} + e\vec{A}(\vec{r}_j)\right]^2\psi_j = \\
&= -\frac{\hbar^2}{2m}\vec{\nabla}^2\psi_j - \frac{\mathrm{i}\hbar e}{2m}\left[\psi_j\vec{\nabla}\cdot\vec{A}(\vec{r}_j) + 2\vec{A}(\vec{r}_j)\cdot\vec{\nabla}\psi_j\right] + \frac{e^2}{2m}\vec{A}^2(\vec{r}_j)\psi_j \\
&= \frac{\hbar^2}{2ma^2}\Big[4\psi_j - \psi_{j+\hat{x}} - \psi_{j-\hat{x}} - \psi_{j+\hat{z}} - \psi_{j-\hat{z}}\Big] \\
&\quad - \frac{\mathrm{i}e\hbar}{2ma}\Big[A_x(\vec{r}_j)\Big(\psi_{j+\hat{x}} - \psi_{j-\hat{x}}\Big) + A_z(\vec{r}_j)\Big(\psi_{j+\hat{z}} - \psi_{j-\hat{z}}\Big) \\
&\quad + \psi_j\Big(A_x(\vec{r}_j + a\hat{x}/2) - A_x(\vec{r}_j - a\hat{x}/2) + A_z(\vec{r}_j + a\hat{z}/2) - A_z(\vec{r}_j - a\hat{z}/2)\Big)\Big] \\
&\quad + \frac{e^2}{2m}\vec{A}^2(\vec{r}_j)\psi_j.
\end{aligned} \tag{2.71}$$

Applying Eq. (2.59) to $A_{x(z)}(\vec{r})$ and $\psi(\vec{r})$ in the second term, the above equation can be rewritten into

$$\begin{aligned}
H_{\mathrm{kin}}\psi_j = \frac{\hbar^2}{2ma^2}\Big[&4\psi_j - \Big(1 + \mathrm{i}\varphi_x^+(\vec{r}_j)\Big)\psi_{j+\hat{x}} - \Big(1 + \mathrm{i}\varphi_x^-(\vec{r}_j)\Big)\psi_{j-\hat{x}} - \\
&- \Big(1 + \mathrm{i}\varphi_z^+(\vec{r}_j)\Big)\psi_{j+\hat{z}} - \Big(1 + \mathrm{i}\varphi_z^-(\vec{r}_j)\Big)\psi_{j-\hat{z}} + \Big(\frac{ea}{\hbar}\Big)^2\vec{A}^2(\vec{r}_j)\psi_j\Big],
\end{aligned} \tag{2.72}$$

with

$$\varphi_x^{\pm}(\vec{r}_j) = \pm\frac{ea}{\hbar}A_x\left(\vec{r}_j \pm \frac{a}{2}\hat{x}\right) \text{ and } \varphi_z^{\pm}(\vec{r}_j) = \pm\frac{ea}{\hbar}A_z\left(\vec{r}_j \pm \frac{a}{2}\hat{z}\right). \tag{2.73}$$

The discretization has to be sufficiently fine, such that the magnetic flux ϕ through one unit cell is small compared to the flux quantum[1], $\phi \ll \phi_0$. Then the so-called Peierls substitution [56] allows us to introduce phase factors by replacing the prefactors $(1 + \mathrm{i}\varphi^{\pm}_{x(z)}(\vec{r}_j))$ by exponentials,

$$\left(1 + \mathrm{i}\varphi^{\pm}_{x(z)}(\vec{r}_j)\right) = \exp\left(\mathrm{i}\varphi^{\pm}_{x(z)}(\vec{r}_j)\right) + \mathcal{O}(a^2). \tag{2.74}$$

It can be shown that this replacement contains the $\vec{A}^2$-term of Eq. (2.72) in the second order of the expansion, wherefore we can omit this term. Hence the final expression of the kinetic Hamiltonian acting on ψ_j is

$$\begin{aligned}\widetilde{H}_{\mathrm{kin}}\psi_j = \frac{2ma^2}{\hbar^2}H_{\mathrm{kin}}\psi_j = 4\psi_j - \mathrm{e}^{\mathrm{i}\varphi^{+}_{x}(\vec{r}_j)}\psi_{j+\hat{x}} - \mathrm{e}^{\mathrm{i}\varphi^{-}_{x}(\vec{r}_j)}\psi_{j-\hat{x}} - \\ - \mathrm{e}^{\mathrm{i}\varphi^{+}_{z}(\vec{r}_j)}\psi_{j+\hat{z}} - \mathrm{e}^{\mathrm{i}\varphi^{-}_{z}(\vec{r}_j)}\psi_{j-\hat{z}}.\end{aligned} \tag{2.75}$$

From Eq. (2.75) we can now extract the elements of the Hamiltonian matrix, which consists of so-called onsite energies on the diagonal and hopping elements between neighboring sites:

$$\left[\widetilde{H}_{\mathrm{kin}}\right]_{i,j} = \begin{cases} 4 & \text{for } i = j \\ -\exp(\mathrm{i}\varphi^{\pm}_{x(z)}) & \text{for neighboring sites } i \text{ and } j \\ 0 & \text{otherwise.} \end{cases} \tag{2.76}$$

If we consider a static perpendicular magnetic field in y-direction with varying strength along the direction of transport we can choose the vector potential as

$$\vec{A}(\vec{r}) = \begin{pmatrix} zB(x) \\ 0 \\ 0 \end{pmatrix} \text{ so that } \vec{B} = \vec{\nabla} \times \vec{A}(\vec{r}) = \begin{pmatrix} 0 \\ B(x) \\ 0 \end{pmatrix}. \tag{2.77}$$

Then the Peierls phases are given by

$$\begin{aligned}\varphi^{\pm}_{x}(\vec{r}_j) &= \pm 2\pi a A_x(\vec{r}_j \pm a\hat{x}/2)/\phi_0 = \pm 2\pi a B(\vec{r}_j \pm a\hat{x}/2)z/\phi_0 = \\ &= \pm B(\vec{r}_j \pm a\hat{x}/2)\frac{2\pi a^2}{\phi_0}\tilde{z} = \pm\tilde{z}\widetilde{B}(\vec{r}_j \pm a\hat{x}/2) \\ \varphi^{\pm}_{z}(\vec{r}_j) &= 0\end{aligned} \tag{2.78}$$

From the above equation we see that the Peierls phase is 2π times the magnetic flux in units of ϕ_0 through one unit cell. The discretization has to be chosen fine enough, so that $\varphi^{\pm}_{x(z)} \ll 1$ in order to justify the Peierls substitution.

[1]The quantity $aA_{x(z)} \sim \phi$ roughly gives the magnetic flux through one unit cell of area a^2, see also Eq. (2.78). So $eaA_{x(z)}/\hbar \sim 2\pi\phi/\phi_0 \ll 1$ for a small enough lattice constant.

The case which is more relevant for our simulations in the following chapters is an in-plane field perpendicular to the transport direction. This can be realized by the choice

$$\vec{A}(\vec{r}) = \begin{pmatrix} -yB(x) \\ 0 \\ 0 \end{pmatrix} \text{ so that } \vec{B} = \vec{\nabla} \times \vec{A}(\vec{r}) = \begin{pmatrix} 0 \\ 0 \\ B(x) \end{pmatrix}. \tag{2.79}$$

As the origin of the coordinate system may be fixed within the plane of the 2DEG, we can set $y = 0$. Then the orbital term of the Hamiltonian can be neglected for moderate magnetic fields where the cyclotron radius $r_C = \hbar k_F/(eB)$ is large compared to the width of the lateral confinement in y-direction and the Peierls phases vanish,

$$\varphi_x^{\pm}(\vec{r}_j) = \varphi_z^{\pm}(\vec{r}_j) = 0. \tag{2.80}$$

The second term of the Hamiltonian (2.68) is the confinement potential $U(\vec{r})$. The discretized form is given by

$$\widetilde{U}_j = \frac{2ma^2}{\hbar^2} U(\vec{r}_j), \tag{2.81}$$

so there is only an onsite contribution $\widetilde{U}_j \delta_{i,j}$ to the Hamiltonian matrix $[\widetilde{H}_0]_{i,j}$.

The last term of the Hamilton operator, called the Zeeman term, is the only one depending on the spin of the electrons. The spin dependent wave functions are written as spinors

$$\psi(\vec{r}) = \begin{pmatrix} \psi_\uparrow(\vec{r}) \\ \psi_\downarrow(\vec{r}) \end{pmatrix} \tag{2.82}$$

of the different spin directions and the Pauli matrices (2.69) define how the magnetic field acts on the individual components of the wave function. The Zeeman term for a position dependent in-plane magnetic field $B(\vec{r})$ in z-direction reads

$$H_Z = \frac{1}{2} g\mu_B B(\vec{r}) \begin{pmatrix} 1 & 0 \\ 0 & -1 \end{pmatrix} = \frac{1}{2} E_Z(\vec{r}) \begin{pmatrix} 1 & 0 \\ 0 & -1 \end{pmatrix}. \tag{2.83}$$

In that case the Zeeman Hamiltonian acts like an additional magnetic field dependent potential which has a different sign for the different spins. A constant field therefore splits the energy spectrum of electrons with opposite spins. The Zeeman energy $E_Z = g\mu_B B$ gives the separation between the resulting up- and down-potential. The dimensionless Zeeman term reads

$$\widetilde{H}_Z = \frac{2ma^2}{\hbar^2} H_Z = \frac{1}{2} \widetilde{E}_Z(\vec{r}) \begin{pmatrix} 1 & 0 \\ 0 & -1 \end{pmatrix}, \tag{2.84}$$

where the Zeeman energy is related to the dimensionless magnetic field strength by $\widetilde{E}_Z = g\widetilde{B}m/m_0$.

Now we can write down the full discretized single particle Hamiltonian (2.68) in matrix form, which has due to the spin degree of freedom a block structure in the spin components

$$H_0 = \begin{pmatrix} H_0^{\uparrow\uparrow} & H_0^{\uparrow\downarrow} \\ H_0^{\downarrow\uparrow} & H_0^{\downarrow\downarrow} \end{pmatrix}. \tag{2.85}$$

Each of the elements $H_0^{\sigma\sigma'}$ is a matrix for itself acting only on one of the spin components. For the specific case of a static magnetic field in z-direction the off-diagonal entries in Eq. (2.85) vanish, i.e. there are no spin-flip processes present. An electron with a given spin σ keeps its spin direction for all the time. Spin-flip processes are involved if the magnetic field is not strictly oriented along the z-direction. Then also the σ_x and σ_y Pauli matrices (2.69) having off-diagonal entries contribute to the Zeeman term. Besides that also spin-orbit interaction [15, 16] leads to spin-flips. Since such processes are not relevant for the purpose of this work, the Hamiltonian and the Green functions are diagonal in the spin index σ. Therefore those objects are fully characterized by one instead of two spin indices.

The final form of the discretized single particle Hamiltonian for an in-plane magnetic field along the z-direction is then given by

$$\left[\widetilde{H}_0\right]_{i,j}^{\sigma} = 4\delta_{i,j} - \delta_{i,j+\hat{x}} - \delta_{i,j-\hat{x}} - \delta_{i,j+\hat{z}} - \delta_{i,j-\hat{z}} + \widetilde{U}_j\delta_{i,j} + \sigma\widetilde{E}_Z(\vec{r}_j)\delta_{i,j}, \tag{2.86}$$

where σ refers to the spin index or spin quantum number $\uparrow = +\frac{1}{2}$ and $\downarrow = -\frac{1}{2}$. The magnetic field in that case only enters through the Zeeman term, as the orbital contribution in the kinetic part of the Hamiltonian can be neglected for an in-plane field. For the numerical implementation it is convenient to subdivide the spatial grid into slices along the z-direction, perpendicular to the direction of transport. With H_n^{σ} we refer to the Hamilton matrix of slice n, which includes the intra-slice hopping elements $\delta_{i,j\pm\hat{z}}$ between neighboring sites within slice n. The matrix $\tau_{n,n+1}^{\sigma}$ contains the inter-slice hopping elements $\delta_{i,j\pm\hat{x}}$ between the neighboring slices n and $n+1$. Then the resulting Hamiltonian matrix of a finite system with N slices has a block-tridiagonal structure

$$\widetilde{H}_0^{\sigma} = \frac{2ma^2}{\hbar^2}\begin{pmatrix} H_1^{\sigma} & \tau_{1,2}^{\sigma} & 0 & \cdots & 0 \\ \tau_{2,1}^{\sigma} & H_2^{\sigma} & \tau_{2,3}^{\sigma} & \ddots & \vdots \\ 0 & \tau_{3,2}^{\sigma} & H_3^{\sigma} & \ddots & 0 \\ \vdots & \ddots & \ddots & \ddots & \tau_{N-1,N}^{\sigma} \\ 0 & \cdots & 0 & \tau_{N,N-1}^{\sigma} & H_N^{\sigma} \end{pmatrix}. \tag{2.87}$$

2.4.3 Lattice Green functions

After the discretization of the Hamiltonian, Eq. (2.86), the Green functions are also represented by a matrix with elements $\widetilde{\mathcal{G}}_{i,j}(E) = a^2\kappa\mathcal{G}(\vec{r}_i, \vec{r}_j; E)$, see Eq. (2.66). In

addition, we also introduce dimension-assigned matrices, where we will use the same symbols H and $\mathcal{G}$ for the Hamiltonian and the Green function in both the continuous and the discrete representation. From the context it will be clear which object we refer to. Those matrices are related to the dimensionless quantities by $H = \kappa\widetilde{H}$ and $\mathcal{G} = \widetilde{\mathcal{G}}/\kappa$. Then the Schrödinger equation for the retarded Green function (2.24) turns into a matrix equation

$$\left[(\widetilde{E} + \mathrm{i}\eta)\mathbb{1} - \widetilde{H}_0\right]\widetilde{\mathcal{G}}_0^r(\widetilde{E}) = \mathbb{1} = \left[(E + \mathrm{i}\eta)\mathbb{1} - H_0\right]\mathcal{G}_0^r(E). \tag{2.88}$$

According to the above relation the retarded Green function of the system is obtained by matrix inversion

$$\mathcal{G}_0^r(E) = \left[(E + \mathrm{i}\eta)\mathbb{1} - H_0\right]^{-1}. \tag{2.89}$$

Since we are dealing with an open system, H_0 and $\mathcal{G}_0^r$ are formally matrices of infinite rank. This problem, however, can be circumvented by dividing the whole system into device and leads as shown in Fig. 2.4. The leads are the homogeneous parts of the system that connect the device to the contacts, without external fields or effective interactions. Often there is no definite border between device and leads and in many situations it is necessary to include parts of the leads into the so-called *extended device*, as discussed later in this work. At least the extended device has to be sufficiently large, such that the physical observables do not change, if a larger part of the leads is included. After this division into device and leads it is possible to truncate the matrices that enter the calculations [23, 30]. If we consider a device connected to a lead α, the Hamiltonian matrix has the form

$$H = \begin{pmatrix} H_d & \tau \\ \tau^\dagger & H_\alpha \end{pmatrix}, \tag{2.90}$$

where H_d and H_α are the Hamiltonians of the isolated device and the isolated lead, respectively, and τ is the coupling between both. Since the discretized single particle Hamiltonian includes only nearest neighbor hopping elements, the matrix τ couples only the last slice of the lead with the first slice of the device. As the magnetic field is assumed to be zero in the leads the coupling matrix is simply given by $\tau = -\kappa\mathbb{1}$ if the two adjacent slices have identical widths. The retarded Green function of the full system has the same structure as the Hamiltonian and obeys the equation

$$\begin{pmatrix} E + \mathrm{i}\eta - H_d & -\tau \\ -\tau^\dagger & E + \mathrm{i}\eta - H_\alpha \end{pmatrix} \begin{pmatrix} \mathcal{G}_d^r & \mathcal{G}_{d\alpha}^r \\ \mathcal{G}_{\alpha d}^r & g_\alpha^r \end{pmatrix} = \begin{pmatrix} \mathbb{1} & 0 \\ 0 & \mathbb{1} \end{pmatrix}. \tag{2.91}$$

Here $\mathcal{G}_d^r$ is the Green function of the entire system projected on the device region, and g_α^r is the full Green function projected on the lead. These functions are distinct from the Green functions of the isolated parts, as the isolated lead Green function for instance is given by

$$g_\alpha^{0r} = \left[E + \mathrm{i}\eta - H_\alpha\right]^{-1}. \tag{2.92}$$

After performing the matrix multiplication in Eq. (2.91) and eliminating $\mathcal{G}^r_{\alpha d}$ we find

$$[E + \mathrm{i}\eta - H_d - \tau g^{0r}_\alpha \tau^\dagger]\mathcal{G}^r_d = \mathbb{1}. \tag{2.93}$$

Hence, the Green function of the open system in the device region, which we will from here on denote by $\mathcal{G}^r_0$ as in Eq. (2.89), can be computed by the inversion of a matrix of the same rank as the device Hamiltonian H_d, which will play the role of H_0. So the coupling to the leads can be exactly taken into account by adding a self-energy

$$\Sigma^r_\alpha(E) = \tau g^{0r}_\alpha(E)\tau^\dagger \tag{2.94}$$

to the Hamiltonian for each lead. Because the matrix τ couples only the adjacent slices of device and lead, only the last slice of the lead Green function g^{0r}_α enters in the self-energy. The Green function of a device coupled to two leads then takes the form

$$\mathcal{G}^r_0 = [E - H_0 - \Sigma^r_L(E) - \Sigma^r_R(E)]^{-1}, \tag{2.95}$$

where the subscripts 'L' and 'R' refer to the left and right lead, respectively. The infinitesimal energy shift $\mathrm{i}\eta$ can now be left out, since the lead self-energies contain a nonvanishing imaginary part.

The advantage of this self-energy method is that one can deal with an infinite system by calculating the Green function of a finite region only, since the lead Green function is known analytically [23, 24], as shown in Appendix B. For a noninteracting lead with hard-wall confinement and a constant width W the transverse wave functions are

$$\chi_m(z) = \sqrt{\frac{2}{W}}\sin\left(\frac{m\pi z}{W}\right) \quad \text{or} \quad \widetilde{\chi}_m(z_j) = \sqrt{\frac{2}{M+1}}\sin\left(\frac{m\pi j}{M+1}\right) \tag{2.96}$$

in dimensionless units, if M is the number of sites in transverse direction, so that $W = (M+1)a$. The lead Green function is then given by

$$\left[g^{0r}_\alpha\right]_{i,j}(E) = \frac{1}{\kappa}\sum_{m=1}^{M}\widetilde{\chi}^{(\alpha)}_m(z_i)\widetilde{\chi}^{(\alpha)}_m(z_j)F(Q), \tag{2.97}$$

with

$$Q = \frac{E}{2\kappa} - 2 + \cos\left(\frac{m\pi}{M+1}\right) \tag{2.98}$$

and

$$F(Q) = \begin{cases} Q - \sqrt{Q^2-1} & \text{for } Q > 1 \\ Q + \sqrt{Q^2-1} & \text{for } Q < -1 \\ Q - \mathrm{i}\sqrt{1-Q^2} & \text{for } |Q| \le 1. \end{cases} \tag{2.99}$$

For the lattice Green functions we can rewrite the Dyson equation (2.54) into a matrix equation by replacing the two-dimensional integrals over the continuous functions by sums over lattice sites, $\int \mathrm{d}^2 r \to a^2 \sum_{\vec{r}_j}$. Then the Dyson equation reads

$$\mathcal{G}^r(E) = \mathcal{G}_0^r(E) + \mathcal{G}_0^r(E)\Sigma^r(E)\mathcal{G}^r(E). \tag{2.100}$$

In an analog way the kinetic equation (2.55) also transforms into a matrix equation

$$\mathcal{G}^<(E) = \mathcal{G}^r(E)\Sigma^<(E)\mathcal{G}^a(E). \tag{2.101}$$

Similar to Eq. (2.94) the lesser self-energy of lead α is related to the lesser Green function $g_\alpha^{0<}(E)$ of the respective lead,

$$\Sigma_\alpha^<(E) = \tau g_\alpha^{0<}(E)\tau^\dagger. \tag{2.102}$$

As the leads are assumed to be in thermal equilibrium we can apply the dissipation-fluctuation theorem (2.27) to obtain $g_\alpha^{0<}(E) = -2\mathrm{i} f(E,\mu_\alpha)\mathrm{Im}\, g_\alpha^{0r}(E)$ and therefore

$$\Sigma_\alpha^<(E) = -2\mathrm{i} f(E,\mu_\alpha)\mathrm{Im}\,\Sigma_\alpha^r(E), \tag{2.103}$$

with lead index $\alpha \in \{L, R\}$.

Although the above presented truncation scheme allows us to deal with finite matrices covering only the device region, the evaluation of the Green function using Eq. (2.95) might still be very demanding. In order to describe the system accurately it is important to use a fine mesh for the discretization, such that the dimensionless energies are small compared to unity, $\widetilde{E} \ll 1$. This however means that the number of sites has to be as large as possible. With an increasing number of lattice points N, the calculation time rises proportional to $N^3 = L^3W^3$, where L is the length and W is the width of the system in units of lattice sites. It is possible to calculate the retarded Green function recursively, by making use of the Dyson equation (2.100) and calculate the Green function slice by slice. This strongly reduces the numerical effort, as the computation time for that algorithm scales like LW^3. This recursive strategy is well-known for non-interacting systems [24, 57], but it can be generalized to include interactions [58], as long as the block-tridiagonal structure of the Hamiltonian, Eq. (2.87), is maintained. This is, for instance, fulfilled for a mean-field description of the electron-electron interaction, where an additional local potential has to be considered, which affects only the diagonal elements of the Hamiltonian matrix. Details about the extension of the recursive Green function algorithm to the nonequilibrium formalism are presented in Appendix C.

2.5 Observables

In this subsection we provide the relations which are necessary to calculate the physical observables out of the Green functions. For most of the derivations we will ignore the spin degree of freedom of the electrons; the spin indices can easily be inserted afterwards. For a spin degenerate system the equations have to be multiplied by a factor of 2.

2.5.1 Density of states

The local density of states is defined by the product of the probability to find a state at a given energy E and the spatial distribution of that state:

$$d(\vec{r}, E) = \sum_{\alpha} |\psi_{\alpha}(\vec{r})|^2 \delta(E - \varepsilon_{\alpha}). \tag{2.104}$$

Here, ε_{α} is the energy spectrum and ψ_{α} are the corresponding eigenfunctions of the considered Hamiltonian.

From the definition of the spectral function, Eq. (2.28), and the eigenfunction representation of the Green function, Eq. (2.25), we find

$$A(\vec{r}, \vec{r}; E) = \sum_{\alpha} \frac{2\eta |\psi_{\alpha}(\vec{r})|^2}{(E - \varepsilon_{\alpha})^2 + \eta^2} \quad \underset{\eta \to 0}{\longrightarrow} \quad 2\pi d(\vec{r}, E). \tag{2.105}$$

Moreover, since $\mathcal{G}^r = [\mathcal{G}^a]^{\dagger}$, the diagonal elements of the retarded and advanced Green function are just complex conjugate to each other and therefore the local density of states is given by the retarded Green function

$$d(\vec{r}, E) = -\frac{1}{\pi} \mathrm{Im}\, \mathcal{G}^r(\vec{r}, \vec{r}; E). \tag{2.106}$$

Let us consider an infinite stripe with constant width W and a periodicity length of L. The wave functions for that system are

$$\psi_{nk}(x, z) = \frac{1}{\sqrt{L}} \mathrm{e}^{\mathrm{i}kx} \sqrt{\frac{2}{W}} \sin\left(\frac{n\pi z}{W}\right) \tag{2.107}$$

and the energy dispersion is

$$E_{nk} = \frac{\hbar^2 k^2}{2m} + \frac{\hbar^2 \pi^2 n^2}{2mW^2} = \frac{\hbar^2 k^2}{2m} + E_n. \tag{2.108}$$

Respecting the cosinusoidal energy dispersion on the lattice, Eq. (2.64), the dimensionless transverse energies are

$$\widetilde{E}_n = 2 - 2\cos\frac{n\pi}{M+1}, \tag{2.109}$$

which correspond to $\hbar^2\pi^2 n^2/(2mW^2)$ for $a \ll W$, $(M \gg 1)$. Inserting this into the definition of the local density of states we find

$$d(\vec{r}, E) = \frac{2}{LW} \sum_{n,k} \sin^2\left(\frac{n\pi z}{W}\right) \delta\left(E - E_n - \frac{\hbar^2 k^2}{2m}\right). \tag{2.110}$$

After rewriting the k-sum into an integral and performing the integral over the delta function we obtain

$$d(\vec{r}, E) = \frac{2m}{\pi\hbar W} \sum_{n} \sin^2\left(\frac{n\pi z}{W}\right) \Big[2m(E - E_n)\Big]^{-1/2}. \tag{2.111}$$

The density of states is defined as the spatial average over the local density of states, yielding

$$d(E) = \int_0^L \frac{\mathrm{d}x}{L} \int_0^W \frac{\mathrm{d}z}{W}\, d(\vec{r}, E) = \frac{m}{\pi\hbar W} \sum_n \Big[2m(E - E_n)\Big]^{-1/2} \tag{2.112}$$

for the homogeneous stripe. The dimensionless density of states is

$$\tilde{d}(\widetilde{E}) = a^2\kappa d(E) = \frac{1}{2\pi\widetilde{W}} \sum_n \Big[\widetilde{E} - \widetilde{E}_n\Big]^{-1/2}. \tag{2.113}$$

2.5.2 Particle density

The definition of the lesser Green function, Eq. (2.19), corresponds to the expectation value of the number operator in the case of equal time and space variables,

$$\mathcal{G}^<(\vec{r}, \vec{r}; t, t) = \frac{\mathrm{i}}{\hbar} \left\langle \hat{\Psi}^\dagger(\vec{r}, t)\hat{\Psi}(\vec{r}, t) \right\rangle = \frac{\mathrm{i}}{\hbar} n(\vec{r}, t), \tag{2.114}$$

where $n(\vec{r}, t)$ is the particle density. Since in steady-state problems the Green functions depend only on time differences, we can express $\mathcal{G}^<$ by its Fourier transform

$$\mathcal{G}^<(\vec{r}, \vec{r}'; t - t') = \int \frac{\mathrm{d}E}{2\pi\hbar}\, \mathrm{e}^{\mathrm{i}E(t-t')/\hbar}\, \mathcal{G}^<(\vec{r}, \vec{r}'; E). \tag{2.115}$$

Therefore the particle density, which is now time-independent, can be computed from the lesser Green function by

$$n(\vec{r}) = -\frac{\mathrm{i}}{2\pi} \int \mathrm{d}E\, \mathcal{G}^<(\vec{r}, \vec{r}; E). \tag{2.116}$$

In the numerical simulations we obtain the dimensionless electron density from the diagonal part of the matrix $\widetilde{\mathcal{G}}^<_{i,j}(E)$ by integrating

$$\tilde{n}_j = -\frac{\mathrm{i}}{2\pi} \int \mathrm{d}\widetilde{E}\, \widetilde{\mathcal{G}}^<_{j,j}(\widetilde{E}). \tag{2.117}$$

In equilibrium the integrand corresponds to the density of states times the Fermi function, according to the dissipation-fluctuation theorem, Eq. (2.27). In a nonequilibrium situation, however, the lesser Green function is still related to the density of states, but the distribution function is different from a Fermi function. Since the nonequilibrium distribution function is in general unknown, the particle density of a biased system has to be computed from $\mathcal{G}^<(E)$, according to Eq. (2.116).

If the density of states is strongly peaked, like for a quantum dot attached to leads or for the homogeneous stripe, Eq. (2.112), the above integral might become numerically demanding. Therefore, we will introduce a method based on complex contour

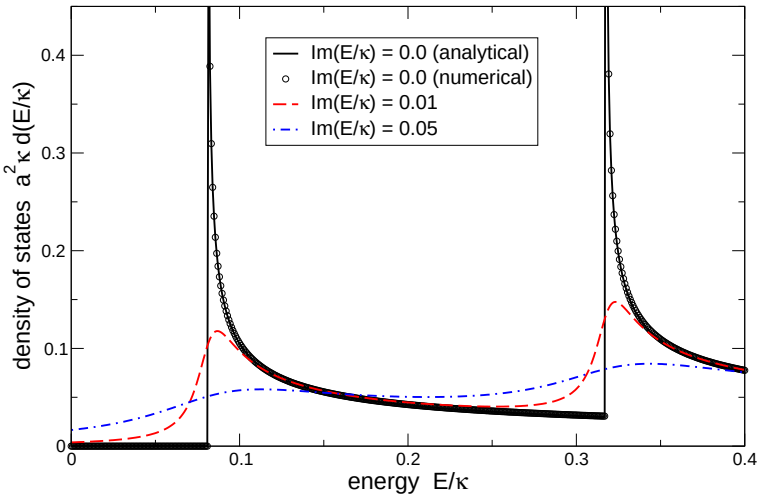

Figure 2.5: The analytical (black solid line) and numerical (black circles) result for the density of states for a homogeneous stripe with width $W = 11a$. The red dashed line and the blue dashed-dotted line are for finite imaginary parts of the energy, $\mathrm{Im}\,(\widetilde{E}) = 0.01$ and $\mathrm{Im}\,(\widetilde{E}) = 0.05$, respectively.

integration in order to circumvent this problem and make the numerical integration more accurate. Following Eq. (2.103) the lesser self-energy of a system coupled to a left and right lead is generally given by

$$\Sigma^<(E) = -2\mathrm{i}\,\mathrm{Im}\,[f(E,\mu_L)\Sigma^r_L(E) + f(E,\mu_R)\Sigma^r_R(E)]\,, \tag{2.118}$$

also in a nonequilibrium situation. At zero temperature the Fermi functions are step functions, $f(E,\mu) = \Theta(\mu - E)$, and we obtain for energies smaller than the lower Fermi level[2], $E < \min(\mu_L, \mu_R)$

$$\Sigma^<(E) = -2\mathrm{i}\,\mathrm{Im}\,[\Sigma^r_L(E) + \Sigma^r_R(E)] = -2\mathrm{i}\,\mathrm{Im}\,\Sigma^r(E). \tag{2.119}$$

Knowing that the retarded and advanced Green functions are related to the Hamiltonian and the self-energies by

$$[\mathcal{G}^r(E)]^{-1} - [\mathcal{G}^a(E)]^{-1} = (E - H - \Sigma^r) - (E - H - \Sigma^a) = -2\mathrm{i}\,\mathrm{Im}\,\Sigma^r(E), \tag{2.120}$$

we can insert Eqs. (2.119) and (2.120) into the kinetic equation (2.101) and express the lesser Green function by

$$\mathcal{G}^<(E) = -\mathcal{G}^r(E) + [\mathcal{G}^r]^\dagger(E). \tag{2.121}$$

[2]An applied source-drain voltage V shifts the bands of the left and right lead. We assume a symmetric shift $\mu_L = \mu + eV/2$ for the left lead and $\mu_R = \mu - eV/2$ for the right lead, see Sec. 4.1.

Then the equilibrium contribution to the particle density n_{eq} obtained from energies $E \leq E_{\max} = \min(\mu_L, \mu_R)$ can be related to the retarded Green function

$$n_{\mathrm{eq}}(\vec{r}) = \frac{\mathrm{i}}{2\pi} \int_{-\infty}^{E_{\max}} \mathrm{d}E \left[\mathcal{G}^r(\vec{r},\vec{r};E) - \mathcal{G}^{r^*}(\vec{r},\vec{r};E)\right] = -\frac{1}{\pi}\mathrm{Im} \int_{-\infty}^{E_{\max}} \mathrm{d}E\, \mathcal{G}^r(\vec{r},\vec{r};E). \tag{2.122}$$

The retarded Green function is analytic in the upper complex half-plane, that means it does not have any poles in that region and all resonances on the real energy axes are broadened for positive imaginary parts of the energy. Fig. 2.5 shows the density of states of a homogeneous wire with width $W = 11a$ exhibiting van Hove singularities at the energy thresholds of the transverse modes. Those sharp structures are smoothed out for complex energies with a positive imaginary part.

Due to the analytic properties of the retarded Green function the integration path to obtain the equilibrium density, Eq. (2.122), can be arbitrarily deformed within the upper complex half-plane. Hence, it is favorable to perform the energy integral along a contour above the real axis, where the integrand is a smooth function [59–62].

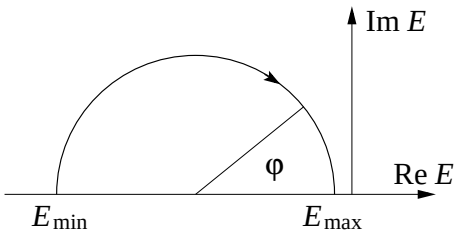

Figure 2.6: Integration contour in the complex energy plane.

We choose the semicircle sketched in Fig. 2.6 as integration contour, which can be parametrized by

$$\gamma(\varphi) = z_0 + r\mathrm{e}^{\mathrm{i}(\pi-\varphi)}, \quad \varphi = 0 \ldots \pi, \tag{2.123}$$

with $z_0 = (E_{\min} + E_{\max})/2$ and $r = (E_{\max} - E_{\min})/2$. The energy $E_{\min}$ has to be smaller than the lowest occupied level, and $E_{\max} = \min(\mu_L, \mu_R)$. With this choice of the contour the equilibrium part of the electron density can be rewritten into

$$\begin{aligned} n_{\mathrm{eq}}(\vec{r}) &= -\frac{1}{\pi}\mathrm{Im} \int_{E_{\min}}^{E_{\max}} \mathrm{d}E\, \mathcal{G}^r(\vec{r},\vec{r};E) \\ &= -\frac{r}{\pi} \int_0^{\pi} \mathrm{d}\varphi \left[\mathrm{Re}\,\mathcal{G}^r\big(\gamma(\varphi)\big)\cos\varphi + \mathrm{Im}\,\mathcal{G}^r\big(\gamma(\varphi)\big)\sin\varphi\right]. \end{aligned} \tag{2.124}$$

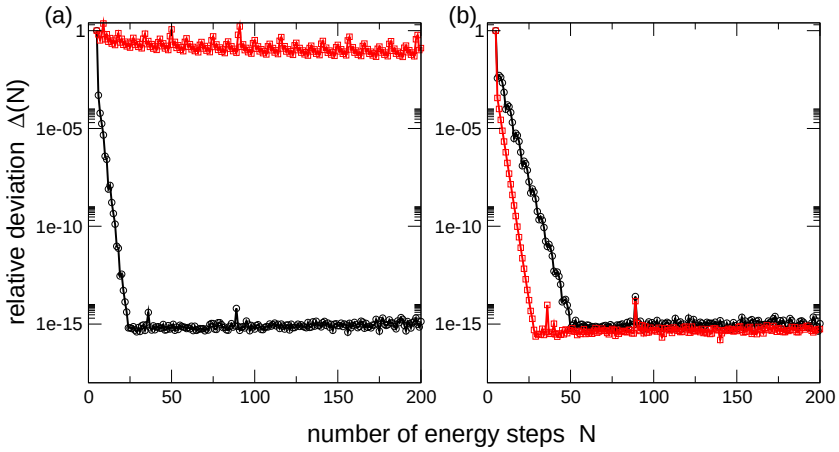

Figure 2.7: The relative deviation of the particle density defined in Eq. (2.125) for the complex contour integration (black circles) and the real axis integration (red squares). In (a) the integration interval is $\widetilde{E} = 0.0 \ldots 0.2$ across one pole, in (b) the interval is $\widetilde{E} = 0.1 \ldots 0.3$ without any pole.

If the left and right chemical potentials are identical and there is no applied bias, the full particle density is already given by n_{eq}. If this is not the case, the remaining integral over the so-called *bias window* from $E_{\max}$ to a value above the highest occupied state has to be performed along the real energy axis with $\mathcal{G}^<(E)$ being the integrand. Therefore it is important that the density of states in that range is sufficiently smooth and that the energy mesh, which is used for the integration, is fine enough. For the computation of n_{eq} the convergence properties are strongly improved if one uses the complex contour integration, as demonstrated by Fig. 2.7. We calculate the particle density $n_N(\vec{r})$ in an equilibrium system ($V = 0$) with N integration steps using the Gaussian quadrature method [63]. The plotted quantity Δ is the deviation from the value with one step less,

$$\Delta(N) = \left\langle \left| \frac{n_N(\vec{r}) - n_{N-1}(\vec{r})}{n_N(\vec{r})} \right| \right\rangle , \tag{2.125}$$

where $\langle \ldots \rangle$ denotes a spatial average over the system. We choose a uniform infinite stripe with width $W = 11a$, where the density of states is shown in Fig. 2.5. To compute the electron density for $\tilde{\mu} = 0.2$ one has to integrate over one pole of the density of states, and we see in Fig. 2.7(a) that the complex contour integration reaches an accuracy of 10^{-15}, which corresponds to the accuracy of a double precision variable, within 30 steps, whereas the real axis energy integration converges very slowly. For comparison, if there is no pole in the integration interval, as shown in Fig. 2.7(b) where the integral from $\widetilde{E} = 0.1$ to 0.3 was calculated, both methods converge very well.

The described method with the semicircle as integration contour works only for zero temperature, $T = 0$. At finite temperatures the integrand has poles due to the Fermi

function at $\mathrm{Re}\, E = \mu$, $\mathrm{Im}\, E = (2\nu + 1)\pi k_B T$ with $\nu \in \mathbb{Z}$. In that case the integration contour has to be modified to enclose a certain number of poles and the integral has to be corrected for the residuals of that poles, as described in Ref. [62]. However, in our finite temperature calculations in Sec. 3.3.6 we use a real axis energy integration, since the density of states in that system is sufficiently smooth.

2.5.3 Conductance

The conductance of a mesoscopic device, which is the inverse electrical resistance at zero bias, $G = \mathrm{d}I/\mathrm{d}V|_{V=0}$, is related to the quantum mechanical transmission amplitudes through the famous Landauer formula [23, 32, 33]

$$G = \frac{e^2}{h} \sum_{\sigma} \sum_{n,m} |t^{\sigma}_{n,m}|^2. \tag{2.126}$$

Here, $t^{\sigma}_{n,m}$ is the transmission amplitude of a particle with spin σ from channel m in the left lead to channel n in the right lead. As we do not consider spin-flip processes in our calculations, the spin quantum number σ is conserved throughout the transmission process. In a spin degenerate system the sum over σ gives a factor of 2 and the above relation yields

$$G = \frac{2e^2}{h} \sum_{n,m} |t_{n,m}|^2 = G_0 \mathcal{T}, \tag{2.127}$$

where $G_0 = 2e^2/h$ is the so-called conductance quantum, and the total transmission is given by

$$\mathcal{T} = \sum_{n,m} |t_{n,m}|^2. \tag{2.128}$$

Due to the factor of 2 in the conductance quantum a single perfectly transmitting channel with $\mathcal{T} = 1$ has a conductance of $G = G_0/2$ per spin. The transmission amplitudes entering the Landauer formula can be expressed by the retarded Green function using the Fisher-Lee relation [23, 34]

$$t_{n,m} = \mathrm{i}\hbar\sqrt{v_n v_m} \int \mathrm{d}z_L \int \mathrm{d}z_R \; \chi^*_n(z_R) \mathcal{G}^r(z_R, z_L) \chi_m(z_L), \tag{2.129}$$

where v_m is the longitudinal velocity in the lead for a particle in the transverse mode m, χ_m is the corresponding wave function given in Eq. (2.96), and $z_{L(R)}$ are the transverse coordinates along the interfaces of the left and right lead, respectively. The velocities are obtained from the dispersion relation (2.64)

$$\hbar v_m = \frac{\partial E}{\partial k_m} = 2\kappa a \sin k_m a, \tag{2.130}$$

where k_m is the longitudinal wave number given by

$$\cos k_m a = -\frac{E}{2\kappa} + 2 - \cos\frac{m\pi}{M+1} = -Q. \tag{2.131}$$

Inserting the lattice wave functions and the matrix Green function in Eq. (2.129) and replacing the integrals by sums, we get

$$t_{n,m} = \frac{\mathrm{i}\hbar\sqrt{v_n v_m}}{a} \sum_{i,j} \widetilde{\chi}_n^{*(R)}(z_i)\, \mathcal{G}^r_{i,j}\, \widetilde{\chi}_m^{(L)}(z_j). \tag{2.132}$$

The total transmission from left to right involves a sum over all $|t_{n,m}|^2$, yielding

$$\mathcal{T} = \sum_{i,i',j,j'} \sum_{n\in R} \widetilde{\chi}_n^{(R)}(z_{i'}) \frac{\hbar v_n}{a} \widetilde{\chi}_n^{*(R)}(z_i) \mathcal{G}^r_{i,j} \sum_{m\in L} \widetilde{\chi}_m^{(L)}(z_j) \frac{\hbar v_m}{a} \widetilde{\chi}_m^{*(L)}(z_{j'}) \mathcal{G}^a_{j',i'}. \tag{2.133}$$

With the definition

$$\begin{aligned} \Gamma^{L(R)} &= \mathrm{i}(\Sigma^r_{L(R)} - \Sigma^a_{L(R)}) = \mathrm{i}(\Sigma^>_{L(R)} - \Sigma^<_{L(R)}) \\ &\Rightarrow \Gamma^{L(R)}_{i,j} = \sum_m \widetilde{\chi}_m^{L(R)}(z_i) \frac{\hbar v_m}{a} \widetilde{\chi}_m^{*L(R)}(z_j) \end{aligned} \tag{2.134}$$

the above equation can be written as a trace

$$\mathcal{T} = \mathrm{Tr}\left\{\Gamma^R \mathcal{G}^r \Gamma^L \mathcal{G}^a\right\} \tag{2.135}$$

and hence the conductance reads [23]

$$G = \frac{2e^2}{h} \mathrm{Tr}\left\{\Gamma^R \mathcal{G}^r \Gamma^L \mathcal{G}^a\right\}. \tag{2.136}$$

For writing down the trace explicitly we note that according to Eq. (2.97) the lead self-energies are symmetric matrices, such that $\Gamma^\alpha = -2\mathrm{Im}\,\Sigma^r_\alpha$. Then the transmission reads

$$\mathcal{T} = 4 \sum_{n,i,j,k} \mathrm{Im}\left[\Sigma^r_R\right]_{n,i} \left[\mathcal{G}^r\right]_{i,j} \mathrm{Im}\left[\Sigma^R_L\right]_{j,k} \left[\mathcal{G}^r\right]^*_{n,k}. \tag{2.137}$$

As the lead self-energies are only non-zero at those sites which are directly connected to the leads, the indices n and i run over the points within the rightmost slice of the discretized device, and j and k over those within the leftmost slice. Hence the matrix elements $\mathcal{G}^r_{i,j}$ and $\mathcal{G}^r_{n,k}$ belong to that part of the Green function that connects the left and right lead.

2.5.4 Current

The current in nonequilibrium systems including interactions which is flowing from lead α into the device can be calculated using the Meir-Wingreen formula[3] [23, 64]

$$I_\alpha = \frac{e}{h}\int \mathrm{d}E\,\mathrm{Tr}\Big\{\Sigma_\alpha^< \mathcal{G}^> - \Sigma_\alpha^> \mathcal{G}^<\Big\}. \tag{2.138}$$

For a two-terminal device with a left and a right lead, as considered within this thesis, α takes the labels 'L' or 'R' and due to current conservation

$$I = I_L = -I_R. \tag{2.139}$$

The Meir-Wingreen formula has an intuitive interpretation: $\Sigma_\alpha^< = |\kappa|^2 g_{0_\alpha}^<$ is the product of the probability to find a particle at the surface of lead α and the hopping probability $|\kappa|^2$ between lead and device. Hence, $\Sigma_\alpha^</h$ can be interpreted as an in-scattering rate from lead α into the device, if there are empty states available. $\mathcal{G}^>$ gives the probability to find an empty state in the device, so that $\frac{1}{h}\Sigma_\alpha^<\mathcal{G}^>$ represents the incoming current per energy unit. Accordingly, $\frac{1}{h}\Sigma_\alpha^>\mathcal{G}^<$ is the outgoing particle current out of the device.

For the numerical evaluation of the current we express it by the retarded and lesser Green function. Therefore we replace $\mathcal{G}^>$ by $-\mathrm{i}A+\mathcal{G}^<$ by means of Eq. (2.28) to obtain

$$I_\alpha = \frac{e}{h}\int \mathrm{d}E\,\mathrm{Tr}\Big\{-\mathrm{i}\Sigma_\alpha^< A + (\Sigma_\alpha^< - \Sigma_\alpha^>)\mathcal{G}^<\Big\}. \tag{2.140}$$

Inserting the definition of the spectral function $A = \mathrm{i}(\mathcal{G}^r - \mathcal{G}^a)$ and using $\Sigma_\alpha^< - \Sigma_\alpha^> = \Sigma_\alpha^a - \Sigma_\alpha^r$ we get

$$I_\alpha = \frac{e}{h}\int \mathrm{d}E\,\mathrm{Tr}\Big\{\Sigma_\alpha^<(\mathcal{G}^r - \mathcal{G}^a) + (\Sigma_\alpha^a - \Sigma_\alpha^r)\mathcal{G}^<\Big\}. \tag{2.141}$$

Because of the symmetry of $\Sigma_\alpha^{r(a)}$, see Eq. (2.97), we have $(\Sigma_\alpha^a - \Sigma_\alpha^r) = 2\mathrm{i}\,\mathrm{Im}\,\Sigma_\alpha^r$, and as the lesser self-energy is purely imaginary, see Eq. (2.103), we end up with the current formula

$$I_\alpha = \frac{\mathrm{i}e}{h}\int \mathrm{d}E\,\mathrm{Tr}\Big\{\mathrm{Im}\,\Sigma_\alpha^<(\mathcal{G}^r - [\mathcal{G}^r]^\dagger) - 2\mathrm{Im}\,\Sigma_\alpha^r\mathcal{G}^<\Big\}. \tag{2.142}$$

The Meir-Wingreen formula is related to the well-known Landauer formula for the current. If we replace the Green functions in Eq. (2.138) with the kinetic equation (2.101) and the corresponding one for $\mathcal{G}^>$, we obtain

$$I_\alpha = \frac{e}{h}\int \mathrm{d}E\,\mathrm{Tr}\Big\{\Sigma_\alpha^<\mathcal{G}^r\Sigma^>\mathcal{G}^a - \Sigma_\alpha^>\mathcal{G}^r\Sigma^<\mathcal{G}^a\Big\}. \tag{2.143}$$

[3] The actual Meir-Wingreen formula derived in [64] is
$I = \frac{\mathrm{i}e}{2h}\int \mathrm{d}E\,\mathrm{Tr}\Big\{\big(f_L\Gamma^L - f_R\Gamma^R\big)\,(G^r - G^a) + \big(\Gamma^L - \Gamma^R\big)\,G^<\Big\}$, which is equivalent to Eq. (2.138).

We have seen in Sec. 2.2 that the effect of electron-electron interactions can be taken into account by a proper self-energy. Thus the total retarded and advanced self-energies consist of three parts,

$$\Sigma^{r(a)} = \Sigma_L^{r(a)} + \Sigma_R^{r(a)} + \Sigma_{\text{int}}^{r(a)}. \tag{2.144}$$

In general the lesser and greater self-energies also have an interaction contribution. However, in Hartree-Fock approximation this contribution vanishes [23] so that $\Sigma^{<(>)} = \Sigma_L^{<(>)} + \Sigma_R^{<(>)}$ and the current can be written as

$$\begin{aligned} I_\alpha &= -\frac{\mathrm{i}e}{h}\int \mathrm{d}E\,\mathrm{Tr}\Big\{\Sigma_\alpha^< \mathcal{G}^r\Gamma\mathcal{G}^a - \Gamma^\alpha\mathcal{G}^r\Sigma^<\mathcal{G}^a\Big\} \\ &= -\frac{\mathrm{i}e}{h}\int \mathrm{d}E\,\mathrm{Tr}\Big\{\Sigma_\alpha^< \mathcal{G}^r(\Gamma^L+\Gamma^R)\mathcal{G}^a - \Gamma^\alpha\mathcal{G}^r(\Sigma_L^< + \Sigma_R^<)\mathcal{G}^a\Big\}, \end{aligned} \tag{2.145}$$

where we made use of Eq. (2.134). Noting that according to Eq. (2.103) the lesser self-energy is $\Sigma_\alpha^< = \mathrm{i}f_\alpha\Gamma^\alpha$, we finally recover the Landauer current formula

$$I = \frac{e}{h}\int \mathrm{d}E\,\mathrm{Tr}\Big\{\Gamma^L\mathcal{G}^r\Gamma^R\mathcal{G}^a\Big\}\Big(f_L - f_R\Big) = \frac{e}{h}\int \mathrm{d}E\,\mathcal{T}(E)\Big(f_L - f_R\Big). \tag{2.146}$$

Hence, the Meir-Wingreen formula (2.138) and the Landauer formula (2.146) for the current are equivalent within the Hartree-Fock approximation. Numerically we rather use Eq. (2.142) than the Landauer formula for computing the current, as the latter involves a matrix product of four matrices, whereas for the former only two matrices have to be multiplied, which have the rank of the lead cross section in units of lattice sites.

CHAPTER 3

Short-range interactions and the 0.7 anomaly

The 0.7 anomaly is a small plateau-like feature appearing in the conductance traces of quantum point contacts at a value of around $0.7 \times G_0$. In this chapter we introduce a model based on delta-like electron-electron interactions and use it to calculate transport properties of quantum point contacts. We show that the resulting conductance curves reproduce the 0.7 anomaly and that the model gives rise to spin splitting and a local spin polarization in the system. We present results concerning the magnetic field and temperature dependence of the 0.7 structure and calculate the shot noise characteristics. The results are compared with conductance curves for long-range Coulomb interactions and we discuss transport of ultracold fermionic atoms, which can also be described by the introduced model.

3.1 Phenomenology of the 0.7 anomaly

One of the most prominent quantum phenomena in mesoscopic physics is the effect of conductance quantization in quasi-one-dimensional systems. Such systems are characterized by a strong confinement of the electrons in the directions perpendicular to the propagation axis. If the length of the narrow channel is large compared to its width the system is called quantum wire, whereas short constrictions, as shown in Fig. 3.1, are named quantum point contacts. The realization of quantum wires or point contacts is usually based on the semiconductor heterostructure technology, where a two-dimensional electron gas (2DEG) forms at the interface between two different semiconductor materials such as GaAs and AlGaAs. With additional gates on top of the heterostructure one can create an electrostatic potential and thus define the shape of the confinement potential inside the 2DEG. By applying a negative voltage to the top-gates one can deplete the electrons from a region underneath the electrodes as indicated in Fig. 3.1 and the electrostatic potential forms a constriction. The effective width of the constriction can be controlled by varying the gate voltage.

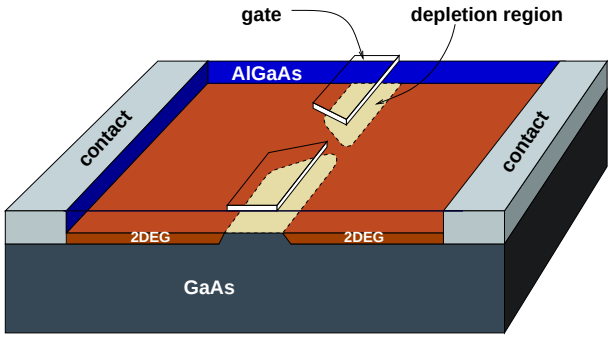

Figure 3.1: A heterostructure made of GaAs and AlGaAs with top-gates forming a quantum point contact.

The conductance $G = \mathrm{d}I/\mathrm{d}V|_{V=0}$ of a quantum point contact measured as a function of the gate voltage exhibits plateaus at integer multiples of the conductance quantum $G_0 = 2e^2/h$ [6, 7, 65]. These steps are well understood in terms of noninteracting electrons [35]. According to the Landauer formula (2.127) the conductance is proportional to the total transmission. If the transmission probability of each transverse mode in the narrowing is unity, the conductance is related to the number of conducting transverse modes or channels. By tuning the gate voltage the effective width and hence the number of channels in the constriction is changed, which then results in a step-like conductance curve. But experimental conductance traces frequently show an additional plateau-like feature below the first conductance step at a value of around $0.7 \times G_0$. Typical conductance curves for different magnetic fields are shown in Fig. 3.2. This so-called *"0.7 anomaly"* was first investigated experimentally in 1996 by Thomas *et al.* [37] who related this anomaly to the spin degree of freedom of the electrons. Since those first measurements there has been much experimental [37, 66–84] and theoretical

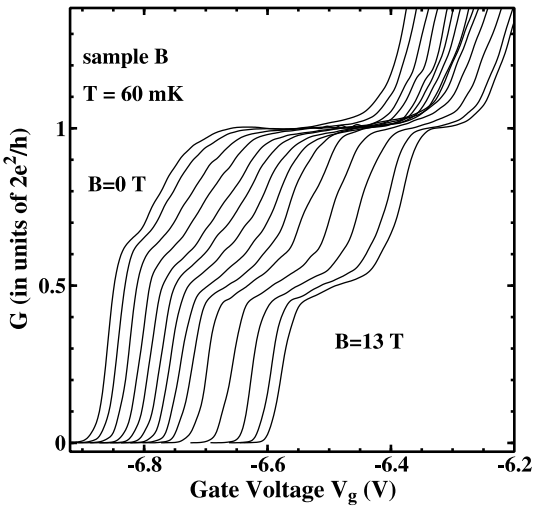

Figure 3.2: The first conductance step of a quantum point contact measured as a function of the gate voltage for various magnetic fields, from Ref. [37]. The different curves are horizontally offset for clarity.

[85–114] effort to explain the origin of this effect. However, a complete understanding is still missing to date and the variety of different interpretations and dissenting publications [115, 116] shows that the explanation of the 0.7 anomaly is a controversial issue.

In the pioneering measurements of the Pepper group [37] the magnetic field and temperature dependence of the 0.7 structure was investigated. They found that the 0.7-feature develops smoothly into the Zeeman spin-split plateau at $0.5 \times G_0$ by applying an in-plane magnetic field, as demonstrated in Fig. 3.2. The 0.5-plateau at high magnetic fields is due to the Zeeman splitting, see Eq. (2.83). The energy levels of the opposite spins are shifted according to

$$E_n^\sigma = E_n^0 + \sigma E_Z \tag{3.1}$$

where $\sigma = \pm 1/2$ is the spin quantum number and E_n^0 are the unperturbed energy levels. The Zeeman energy $E_Z = g\mu_B B$ with effective gyromagnetic factor g and Bohr magneton $\mu_B = e\hbar/(2m_0)$ gives the energy difference between the up- and down-levels. So for a positive magnetic field B the down-electrons contribute to the conductance at an energy of $E_n^0 - E_Z/2$, whereas the up-electrons are transmitted at energies higher than $E_n^0 + E_Z/2$. This leads to a $G_0/2$-plateau where in the regime of the first half-step the transmission is spin-polarized. The fact that the 0.7 plateau widens and evolves continuously towards the value of $0.5 \times G_0$ in the presence of a magnetic field made the authors of Ref. [37] conjecture that the 0.7 anomaly is related to the electron spin. They assumed the presence of a partial spin polarization in one-dimensional systems. In addition, a peculiar temperature dependence of the 0.7-feature was found: Although finite temperatures usually tend to wash out any structures in physical ob-

servables, within a certain range the 0.7-plateau gets more pronounced with increasing temperature T.

In pursuing experiments [66, 69, 72, 73] the conductance characteristics in the presence of finite source-drain voltages V was investigated. The measured quantities are the differential conductance $\mathrm{d}I/\mathrm{d}V$ as a function of V and the transconductance $\mathrm{d}G/\mathrm{d}V_\mathrm{g}$ as a function of V and gate voltage V_g. The experimental results indicate the presence of spin splitting for the lowest energy level, meaning that the degeneracy between the up- and down-energy level is lifted. Moreover, the differential conductance traces exhibit a zero bias anomaly in many samples [74, 75, 77, 78, 83], which manifests in a peak around $V = 0$. The appearance of the zero bias anomaly was related to a Kondo-correlated state [74] and also the temperature dependence of the 0.7 structure showed a similar scaling behavior as for the Kondo effect in quantum dots. The temperature scaling can be quantified by the use of a scaling parameter T_K, the Kondo temperature. In a later experiment the spin-resolved contributions to the conductance were measured [75], where an additional quantum point contact was used as a detector of electrons. Since electrons with opposite spins have a different cyclotron radius in the presence of spin-orbit interaction, one can spatially split the orbits of the up- and down-electrons. By tuning a perpendicular magnetic field it is possible to detect particles of one certain spin. They found that in the regime of the 0.7 structure the up- and down-contributions to the conductance are different, which supports the idea of a spontaneous spin splitting in such systems. The result of a static spin polarization contradicts the Kondo interpretation, where the polarization is dynamic. In recent experiments the shot noise characteristics of quantum point contacts exhibiting a 0.7 feature was investigated [76–78]. The experimentalists found a noise suppression in the regime where the 0.7 feature appears, indicating a polarized transmission of electrons in the single particle picture. It was furthermore found that features related to the 0.7 anomaly appear at high magnetic fields as well [79–81]. These so-called *0.7 analogs* occur at higher values of the conductance, e.g. $G \approx 1.2 \times G_0$, when subbands of electrons with opposite spins cross due to the Zeeman splitting.

On the theoretical side there is great variety of different approaches towards the 0.7 anomaly. In an early publication Wang and Berggren showed that the Coulomb interaction among the electrons in a homogeneous quantum wire can cause spin splitting [85]. They used density functional theory (DFT) on the Hartree-Fock level taking into account the classical Coulomb interaction and the exchange term in local density approximation. This work was followed by more sophisticated DFT calculations [86–99] where the quantum point contact was either modelled by a saddle-point potential [86, 89], or realistic electrostatic gate potentials were included [88, 90, 92, 95], and correlation potentials were considered [89, 90, 92, 93, 95]. A common result of the DFT approach is the splitting of the energy levels with different spins leading to a local spin polarization inside the quantum point contact. The spin splitting furthermore gives rise to differently transmitting channels of the up- and down-electrons which manifests in a 0.7 feature in the total conductance. However, to our knowledge there are no DFT results showing the correct temperature dependence, as it is observed in experiments.

The finding of spin-split energy levels was used to formulate a phenomenological model [101] which was later adapted and reformulated [102, 103]. In the latter spin splitting model the author assumes that the degenerate energy levels of the first subband start to split linearly with the gate voltage as soon as the chemical potential crosses the energy level. The only free parameter in this model is the splitting rate. By adjusting this parameter it is possible to reproduce the experimentally observed magnetic field and temperature behavior of the 0.7 anomaly. Also the shot noise suppression is correctly described by this model [77, 78].

Due to the local spin polarization in the quantum point contact found in DFT calculations [86, 88–91, 93, 95, 97–99] the idea of Kondo physics in quantum point contacts came into consideration [97, 98, 117]. The Kondo effect in metals [118] or quantum dots [119] occurs when a single spin is localized in the system, e.g. through an impurity atom with an unpaired electron. Meir and coworkers interpret the DFT findings as a localized spin and describe the quantum point contact by an Anderson Hamiltonian [120] with energy levels coupled to leads including onsite interactions [97]. They evaluate the transport properties of the model Hamiltonian in the Kondo regime with a singly occupied site. Arguments in favor of a Kondo interpretation of the 0.7 anomaly are the experimentally observed zero-bias anomaly in the differential conductance and the temperature scaling [74] which can be qualitatively reproduced by the Kondo model [97]. The model also accounts for the shot noise suppression at the 0.7 structure [100].

Further theoretical approaches are based on interaction with phonons [104], the formation of a Wigner crystal [107–109], or on Hubbard-like models revealing a magnetic moment in the quantum point contact [105, 106], and giving rise to a suppression of the conductance towards $0.75 \times G_0$ [110]. Our approach is based on the Green function formalism for electronic transport in the presence of short-range electron-electron interactions, which is incorporated on the Hartree-Fock level.

3.2 The model of interacting electrons

We aim to describe the influence of short-range electron-electron interactions on the transport properties of quantum point contacts. Our starting point is a general effective mass single-particle Hamiltonian for electrons with charge $-e$ confined in a 2DEG in the presence of an in-plane magnetic field $B(\vec{r})$

$$H_0^\sigma = -\frac{\hbar^2}{2m}\vec{\nabla}^2 + U(\vec{r}) + g\mu_B B(\vec{r})\sigma. \tag{3.2}$$

The first term accounts for the free motion of the electrons with effective mass m within the 2DEG, $U(\vec{r})$ is the confinement potential defining the geometry of the system, and the last term, known as the Zeeman term, acts like an additional magnetic field dependent potential, which has a different sign for the different spins. Here, $\sigma = \pm 1/2$ is the spin quantum number, g is the effective gyromagnetic factor, and $\mu_B = e\hbar/(2m_0)$

is the Bohr magneton with m_0 being the free electron mass. The 2DEG is located in the (x, z)-plane of our coordinate system, where the x-direction is the direction of transport and $\vec{r} = (x, z)$ denotes a vector within that plane. As we consider an in-plane magnetic field, we can choose the vector potential

$$\vec{A}(\vec{r}) = \begin{pmatrix} -yB(x) \\ 0 \\ 0 \end{pmatrix} \text{ so that } \vec{B} = \vec{\nabla} \times \vec{A}(\vec{r}) = \begin{pmatrix} 0 \\ 0 \\ B(x) \end{pmatrix}. \tag{3.3}$$

Because the 2DEG is located at $y = 0$ the $\vec{A}$-field vanishes and we do not have to consider the orbital contribution of the magnetic field which modifies the momentum operator $-\mathrm{i}\hbar\vec{\nabla} \rightarrow -\mathrm{i}\hbar\vec{\nabla} + e\vec{A}$, as shown in Eq. (2.68). This holds as long as the confinement of the 2DEG is so strong that the spreading of the wave function in y-direction is much smaller than the cyclotron radius $r_C = \hbar k_F/(eB)$. The potential $U(\vec{r})$ we use for our calculations is a hard-wall confinement potential which is zero inside the scatterer and infinite outside the system. The geometry used for the calculations is discussed later in this section.

In addition to the Hamiltonian (3.2) for noninteracting particles we include short-range interactions with an interaction potential

$$w(\vec{r}, \vec{r}\,') = \gamma\delta(\vec{r} - \vec{r}\,'), \tag{3.4}$$

where γ gives interaction strength. This choice of the interaction can be interpreted as a simple model for an efficiently screened Coulomb potential. In a homogeneous 2DEG the screening length λ_S in Thomas-Fermi approximation is given by [121]

$$\lambda_S = \frac{2\pi\varepsilon_0\varepsilon\hbar^2}{me^2}, \tag{3.5}$$

where ε is the material specific dielectric constant. For GaAs the dielectric constant is $\varepsilon = 13$ and the effective mass is $m = 0.07m_0$ [122] resulting in a screening length of $\lambda_S \approx 5\,\mathrm{nm}$. This length scale has to be compared to the width of the constriction, which is controlled by the gate voltage. From source-drain bias measurements one can obtain the energy level spacing in the quantum point contact and by approximating the electrostatic confinement potential by a parabolic potential $U_z = (1/2)m\omega^2 z^2$, one can extract a typical value for the confinement frequency of $\omega \approx 4 \times 10^{12}\,\mathrm{s}^{-1}$ [67]. Thus, when the first subband crosses the Fermi energy the width of the transverse confinement is

$$W = 2\sqrt{\hbar/(m\omega)} \approx 40\,\mathrm{nm}, \tag{3.6}$$

where we used $m = 0.07m_0$ for GaAs. Although the screening length is smaller than the system size, we do not expect to get an accurate description of the physics with this simple model. However, the motivation for choosing that kind of interaction is twofold: on the one hand it provides a comparatively simple approach to interactions which

results in an intuitive understanding of spin splitting due to the repulsive interactions between different spins, as seen later in Eq. (3.11). On the other hand this choice of the interaction is suitable to treat neutral fermionic atoms which interact via a contact potential, as discussed in Sec. 3.5.3.

The interaction strength γ entering our model can be estimated by comparison with a screened Coulomb potential

$$w_{\mathrm{C}}(\vec{r},\vec{r}\,') = \frac{e^2}{4\pi\varepsilon_0\varepsilon}\frac{\mathrm{e}^{-|\vec{r}-\vec{r}\,'|/\lambda_S}}{|\vec{r}-\vec{r}\,'|}. \tag{3.7}$$

The total interaction energy of an electron located at $\vec{r}\,'$ is given by integrating the interaction potential over the full two-dimensional space. In the case of delta interactions the total interaction energy gives

$$\int \mathrm{d}^2r\; w(\vec{r},\vec{r}\,') = \gamma. \tag{3.8}$$

Equating this with the total energy in the presence of a screened Coulomb interaction, Eq. (3.7), we obtain

$$\gamma = \frac{e^2}{4\pi\varepsilon_0\varepsilon}\int \mathrm{d}^2r\;\frac{\mathrm{e}^{-|\vec{r}-\vec{r}\,'|/\lambda_S}}{|\vec{r}-\vec{r}\,'|} = \frac{e^2\lambda_S}{2\varepsilon_0\varepsilon}. \tag{3.9}$$

Inserting the Thomas-Fermi screening length from Eq. (3.5) yields

$$\gamma = 2\pi\frac{\hbar^2}{2m}. \tag{3.10}$$

This value represents a rough estimation for the interaction constant as there are two approximations involved. First of all, the Thomas-Fermi screening length of a 2DEG is density independent. Going beyond this level of approximation one finds a reduced screening at low densities resulting in a larger screening length [121]. As we are interested in the regime where the first channel in the quantum point contact opens, the density is expected to be fairly low. Second, the screening in two-dimensional systems is less efficient than in three dimensions resulting in an r^{-3} law for the asymptotic behavior of the interaction potential [121]. However, the total interaction energy does not differ drastically from the one obtained by exponential screening. Both effects would give rise to a slightly higher value for γ. For our numerical calculations we shall stick to the order of magnitude provided by Eq. (3.10), and we find significant effects of the interaction already at values around $\gamma = 4.5\times\hbar^2/(2m)$, about 30% smaller than the estimated value $2\pi\times\hbar^2/(2m)$.

The interaction is incorporated in our calculations on the Hartree-Fock level. The corresponding interaction self-energy entering the Green function formalism is derived in Appendix A. For the choice of delta interactions the self-energy is local, so that the

interaction can be treated like an additional potential which is according to Eq. (A.14) given by

$$V_{\mathrm{int}}^{\sigma}(\vec{r}) = \gamma n_{-\sigma}(\vec{r}). \tag{3.11}$$

The interaction potential which is seen by electrons with spin σ is proportional to the density of electrons with opposite spin $-\sigma$. This repulsive interaction between different spins tends to destabilize an equal population of up- and down-electrons. If the number of down-electrons is slightly higher than the number of up-electrons in the system, the up-electrons are repelled from the system resulting in an even stronger imbalance between the different spins. This mechanism is responsible for the spin splitting as we will show later in this chapter.

In the implementation we use a discretized space and rescale all quantities with appropriate lattice units as described in Sec. 2.4.1, in order to obtain dimensionless quantities. The dimensionless density is then given by $\tilde{n}(\vec{r_j}) = a^2 n(\vec{r_j})$, which scales with the lattice constant a. The Hamiltonian is given in units of $\hbar^2/(2ma^2)$ and the dimensionless coupling constant is $\tilde{\gamma} = (2m/\hbar^2)\gamma$, so that the dimensionless interaction potential reads

$$\widetilde{V}_{\mathrm{int}}^{\sigma}(\vec{r_j}) = \frac{2ma^2}{\hbar^2}\gamma n_{-\sigma}(\vec{r_j}) = \tilde{\gamma}\tilde{n}_{-\sigma}(\vec{r_j}) \tag{3.12}$$

Hence, the interaction potential is independent of the numerical grid as it does not scale with the lattice constant a.

The geometry mimicking a quantum point contact which is used in our calculations is shown in Fig. 3.3 and it consists of three different regions: attached to the left lead there is a narrowing part where the width decreases linearly over 24 lattice sites from

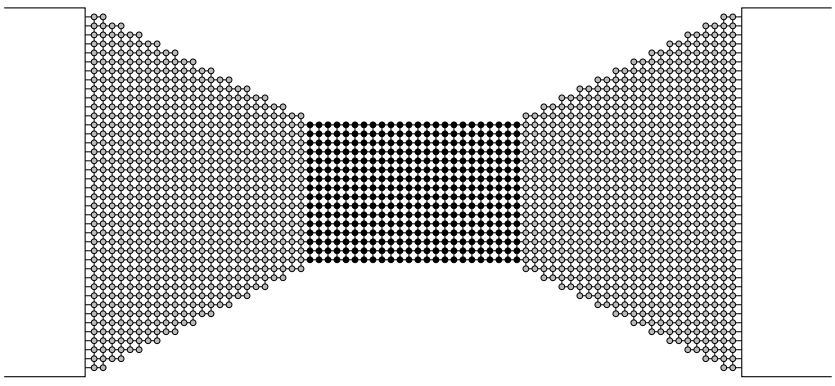

Figure 3.3: The geometry of the system in discretized representation. A linear constriction with a short wire of length $24a$ and a width of 16 sites in the center. In the narrowing regions marked by the grey filled spots the interaction is switched on and off. The 40 sites wide leads are indicated by the white bars to the left and to the right of the system.

$41a$ to $17a$[1], with a being the lattice constant of the numerical grid. In that part of the system which is marked by grey filled points the interaction strength is gradually switched on according to the sinusoidal function

$$s_L(x) = \sin^2\left(\frac{x\pi}{2L}\right), \tag{3.13}$$

that continuously switches from 0 to 1 over a distance of L, in our case $L = 24a$. After the narrowing there is a short quantum wire with width $17a$ and length $24a$, where the electrons are fully interacting according to the effective potential in Eq. (3.11). The system widens linearly before it is connected to the right lead. In that region the coupling constant is reduced according to an analog expression of Eq. (3.13).

In the experiments the conductance is typically measured as a function of the gate voltage, which changes the geometry of the system, whereas the chemical potential is fixed. For the simulations it is favorable to vary the chemical potential and do not change the geometry. Those two methods are equivalent as both change the number of occupied transverse channels in the quantum point contact. The numerical procedure to obtain the transport properties in presence of electron-electron interactions is based on the self-consistent solution of the retarded Green function and the particle density. Since the interaction in the considered case acts like an additional local potential, Eq. (3.11), the retarded Green function in discretized representation can be obtained by matrix inversion

$$\mathcal{G}_0^r = [E - H_0^\sigma - V_{\text{int}}^\sigma - \Sigma_L^r(E) - \Sigma_R^r(E)]^{-1}, \tag{3.14}$$

according to Eq. (2.95). Here, H_0^σ is the noninteracting part of the Hamiltonian given in Eq. (3.2) and $\Sigma_{L(R)}^r$ are the self-energies due to the coupling to the left (right) lead, which are defined in Eq. (2.94). From the retarded Green function one gets the lesser function by the kinetic equation (2.101) which gives the particle density, Eq. (2.116), and therefore defines the interaction potential through Eq. (3.11). Thus, the interaction potential V_{int}^σ is determined by the retarded Green function, and in turn the interaction potential is necessary to compute the retarded Green function. Hence, the equations for the Green function and the interaction potential have to solved self-consistently. This is done using an iterative scheme which is visualized by the flowchart in Fig. 3.4. We start with an initial guess for the interaction potential, e.g. $V_{\text{int}}^{\sigma(0)}(\vec{r}) \equiv 0$, and calculate the retarded Green function by means of Eq. (3.14). Using Eqs. (2.101), (2.116), and (3.11) we obtain a new value for the interaction potential $V_{\text{int}}^{\sigma(1)}(\vec{r})$. With this new value of the interaction potential we restart the above described cycle and repeat it, until we reach convergence. The convergence criterion is fulfilled, if the maximum of the squared relative deviation is smaller than 10^{-5},

$$\max_{\vec{r}} \left(\frac{V_{\text{int}}^{\sigma(N)}(\vec{r}) - V_{\text{int}}^{\sigma(N-1)}(\vec{r})}{V_{\text{int}}^{\sigma(N)}(\vec{r})} \right)^2 < 10^{-5}. \tag{3.15}$$

[1]Note: the width which is represented by M lattice sites is $(M+1)a$.

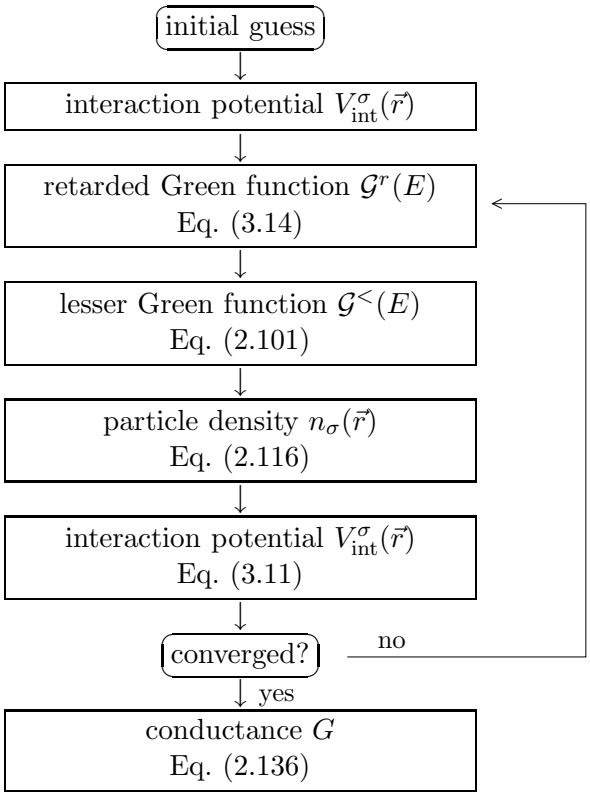

Figure 3.4: Flowchart of the self-consistent calculation scheme to obtain the interaction potential and the conductance.

In order to improve the convergence properties it is advantageous to use the converged interaction potential of the previous value of the chemical potential μ as starting point for the next step, since for two nearby values of μ the interaction potential is expected to be similar. Furthermore it is necessary to include a damping in the iteration scheme,

$$V_{\mathrm{int}}^{\sigma(N)}(\vec{r}) = V_{\mathrm{int}}^{\sigma(N)}(\vec{r}) + \Omega^N \left[V_{\mathrm{int}}^{\sigma(N-1)}(\vec{r}) - V_{\mathrm{int}}^{\sigma(N)}(\vec{r}) \right], \tag{3.16}$$

which includes a fraction Ω^N of the old value of the interaction potential. This fraction gets smaller in each iteration step and in our simulations we used $\Omega = 0.6$ in order to achieve a well-behaved convergence.

3.3 Numerical results

3.3.1 Influence of the interaction strength

The experimental conductance traces show a small shoulder-like feature at a value of around $0.7 \times G_0$ as shown in Fig. 3.2. The actual position of the 0.7 structure has proven to vary between $0.5 \times G_0$ and $0.7 \times G_0$, depending on the carrier density and the

wire length [72, 89, 91, 93]. Using the above described model of interacting electrons we calculate the conductance at zero temperature. It is convenient to use the energy of the first transverse mode in the narrow region of the scatterer of width W as the energy unit,

$$E_1 = \frac{\hbar^2\pi^2}{2mW^2}. \tag{3.17}$$

To break the symmetry between electrons with different spins it is common to apply a small magnetic field [89, 93, 95]. In our simulations the Zeeman energy has a value $E_Z = g\mu_B B = 0.0015\,E_1$. The case of zero magnetic field is discussed separately in Sec. 3.3.4.

The resulting conductance curves are shown in Fig. 3.5 for different interaction strengths γ. They exhibit an additional feature below the first plateau for sufficiently high interaction constants, which are within the physically relevant regime, see Eq. (3.10). The transconductance $\partial G/\partial\mu$ evolves from a single peak to a double-peak structure, reflecting the appearance of an additional plateau. The lowest value of the interaction strength for which a second peak occurs in the transconductance is $\gamma = 3.9 \times \hbar^2/(2m)$, and the corresponding plateau height is $0.76 \times G_0$. With increasing interaction constant the 0.7 plateau gets wider and it evolves towards lower conductance values, $0.58 \times G_0$ for $\gamma = 4.7 \times \hbar^2/(2m)$. Hence, the position and the width of the 0.7 plateau depends on the interaction strength γ.

For selected values of γ the spin-resolved contributions to the conductance are

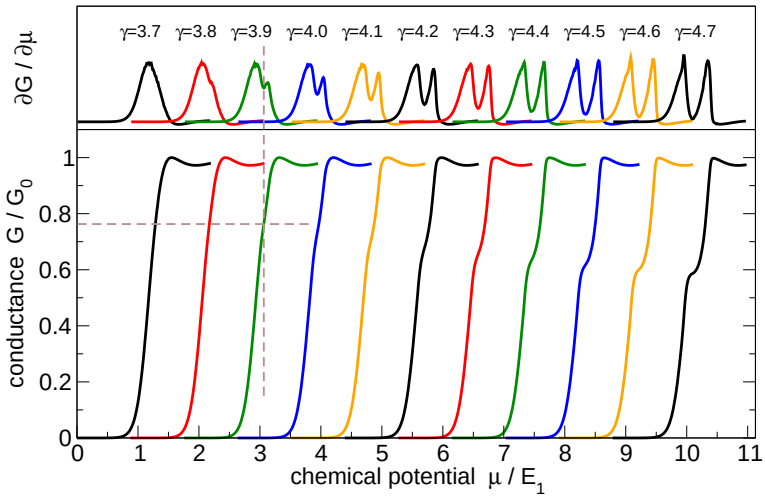

Figure 3.5: Lower panel: conductance traces for different interaction constants $\gamma = 3.7 \ldots 4.7$ in units of $\hbar^2/(2m)$. Upper panel: transconductance $\partial G/\partial\mu$ in arbitrary units for the corresponding values of γ. The different traces are horizontally offset for clarity. The dashed lines mark the position of the "plateau" for the lowest value of γ, where the transconductance has a double-peak shape.

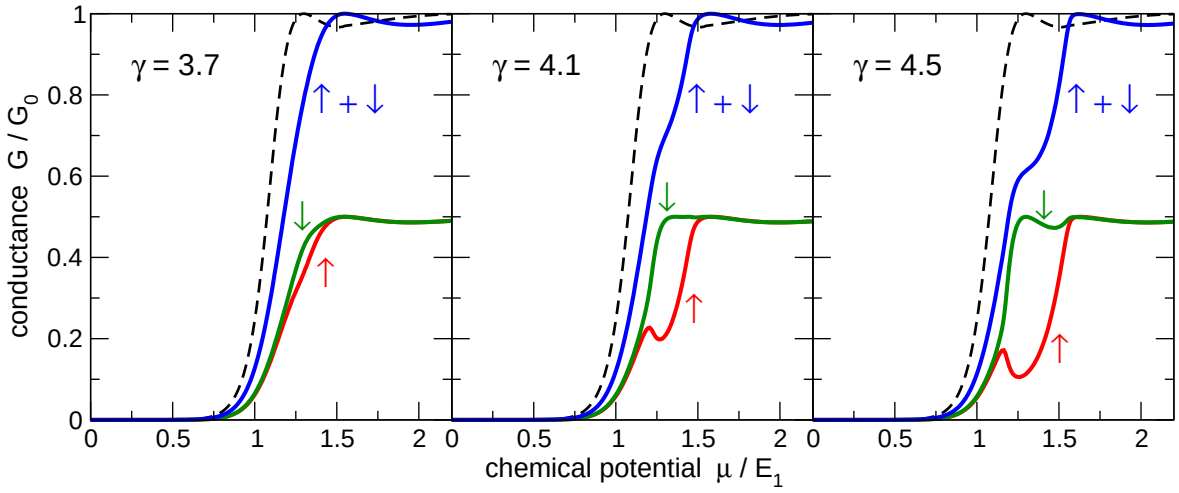

Figure 3.6: Spin-resolved conductance traces for different interaction strengths $\gamma = 3.7$, $\gamma = 4.1$, and $\gamma = 4.5$ in units of $\hbar^2/(2m)$ from left to right. The green and red curves are the up- and down-contributions, respectively, and the blue line shows the total conductance. The dashed black curve shows the conductance of noninteracting electrons.

displayed in Fig. 3.6. For the lowest value of the interaction constant $\gamma = 3.7 \times \hbar^2/(2m)$ there is no 0.7 feature in the total conductance. However, a small difference between the up- and down-contribution is visible, which is not due to the Zeeman splitting. The Zeeman energy of the applied magnetic field is approximately two orders of magnitude smaller than the observed energy difference in the conductance traces. Therefore, the repulsive electron-electron interaction causes the splitting. Moreover, the conductance curves exhibit an overall shift towards higher energies with respect to the noninteracting case. With increasing coupling constant the difference between the up- and down-contribution to the conductance gets larger and in parallel a plateau evolves in the total conductance. The spin-resolved conductance curves are in agreement with DFT results [89, 91, 93, 95, 96] and with conductance traces of a model assuming a Gaussian spin splitting [70].

3.3.2 Level splitting and polarization

The repulsive interaction between different spins provides an intuitive explanation of the mechanism causing the spin splitting. Due to the small but finite magnetic field the transverse energy levels experience a shift of $\pm E_Z/2$ for the different spins. This causes an imbalance in the occupation of electrons with different spins: since for a positive magnetic field the energy level of the down-electrons is the lower one, there are slightly more down-electrons in the system than up-electrons. Due to the interaction potential (3.11) this results in a higher potential barrier for the up-electrons which tends to increase the initial imbalance of carriers in the constriction. We define the effective

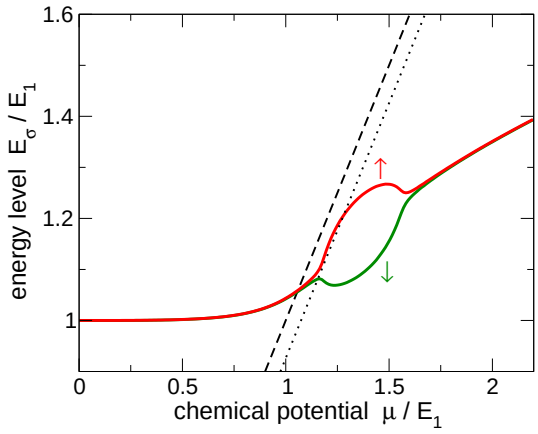

Figure 3.7: Energy levels of the up-electrons (upper red line) and down-electrons (lower green line) according to Eq. (3.18) for $\gamma = 4.5 \times \hbar^2/(2m)$. The dashed line displays the chemical potential, and the dotted line marks the shifted chemical potential $\mu - 0.074\,E_1$ (see text).

transverse energy levels as

$$E_\sigma = E_1 + \sigma E_Z + \langle V^\sigma_{\rm int}(\vec{r})\rangle, \tag{3.18}$$

where $\langle \ldots \rangle$ denotes a spatial average over the fully interacting region. Here, E_1 is the first transverse mode in the narrow part of the device, see Eq. (3.17), σE_Z is the Zeeman shift, in our case $E_Z = 0.0015\,E_1$, and the last term is the average interaction energy felt by an electron with spin σ. In Fig. 3.7 we see that the energy levels of the different spins first evolve parallel and are bent upwards due to the interaction energy with increasing μ. In the region where the chemical potential crosses the energy levels, the occupation gets large and the repulsion of electrons with opposite spins becomes important. In that range the energy levels start to split distinctly; this region coincides with the energy range, where the up- and down-electrons contribute differently to the conductance, as shown in Fig. 3.6. When the chemical potential is well above both energy levels, the splitting vanishes and the interaction energy is identical for both spin species.

After the onset of spin splitting the upper energy level evolves parallel to the chemical potential within a substantial energy range. If we consider the fact that E_1 is the first transverse mode only for an infinite system of width W, we may shift the energies in Eq. (3.18). From Fig. 3.6 we see that the "center" of the first subband, that is the energy where the conductance in the noninteracting case is $G_0/2$, is located at $1.074\,E_1$. For the plot of the energy levels this can be accounted for by a downward shift of the chemical potential by $0.074\,E_1$, which is represented by the dotted line in Fig. 3.7. The *pinning* of the upper energy level to the shifted value of the chemical potential is even more obvious. There is experimental evidence for the occurrence of level pinning [82, 84] and it is an essential ingredient for the spin splitting models [101–103] in order

to get a 0.7 plateau. Moreover we see that the level splitting sets in as soon as the shifted chemical potential crosses the energy levels, which supports the assumption of the spin splitting models.

The energy level pinning provides an intuitive explanation for the appearance of the anomalous plateau at values around $0.7 \times G_0$. Due to the geometry of the system the transverse energy levels are not sharp, but exhibit a broadening which is in our case of the order of $E_1/2$, as seen in Fig. 3.6. In the region where the upper energy level is pinned to the chemical potential only about one half of the broadened upper level is below μ. Hence, only a fraction of one half of the spin-up level contributes to the conductance, whereas the spin-down level is fully transmitting. This results in a conductance plateau at around $(1 + 0.5)e^2/h = 0.75 \times G_0$ in the range of the level pinning.

Like in DFT results [86, 88–91, 93, 95, 97–99] we find a local spin polarization inside the constriction at chemical potentials where the 0.7 structure appears. We calculate the particle densities and the polarization $n_\downarrow(\vec{r}) - n_\uparrow(\vec{r})$ for $\mu = 1.32\,E_1$, where the spin splitting is maximal, see Figs. 3.6 and 3.7. The result in Fig. 3.8 shows that the density of up-electrons is strongly suppressed inside the constriction whereas the

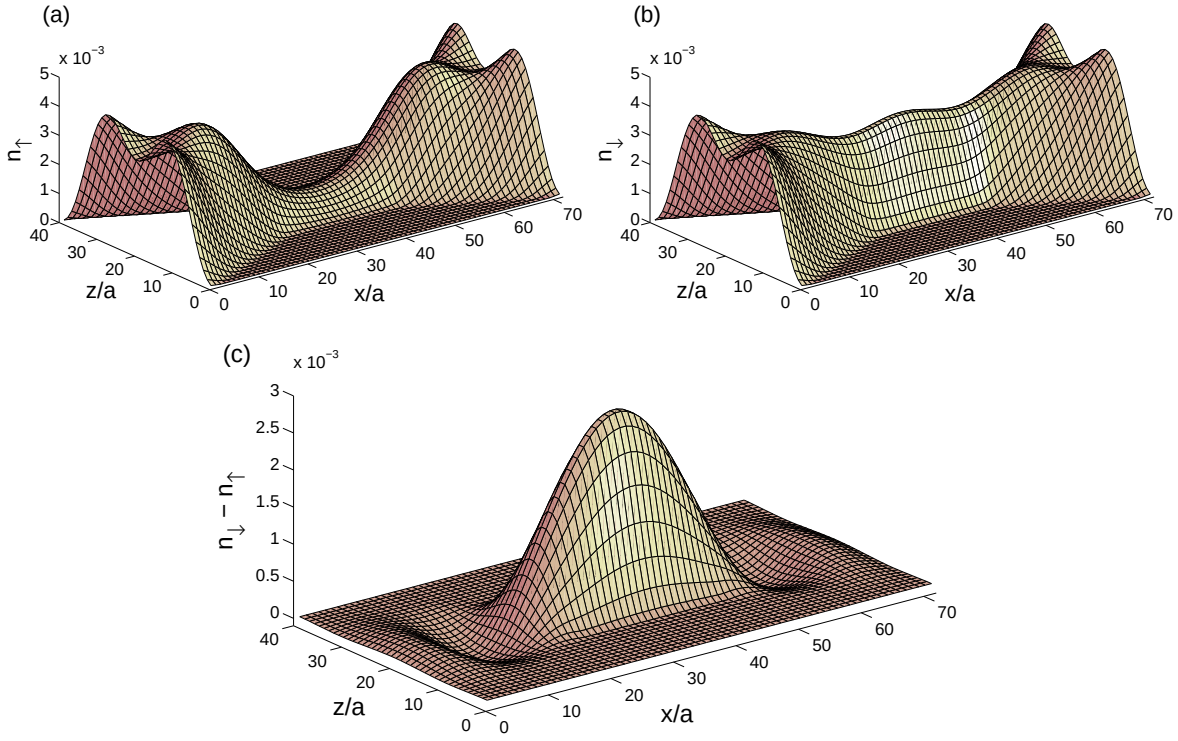

Figure 3.8: (a) Density of the up-electrons; (b) density of the down-electrons in units of a^{-2} for $\mu = 1.32\,E_1$ and $\gamma = 4.5 \times \hbar^2/(2m)$, with the x-axis being the direction of transport. (c) Polarization $n_\downarrow(\vec{r}) - n_\uparrow(\vec{r})$ in the system.

density of spin-down electrons is almost flat along the direction of transport. This results in a finite spin polarization at the center of the constriction.

3.3.3 Magnetic field dependence and the 0.7 analog

In the experiments the 0.7 structure evolves into the Zeeman spin-split plateau at $0.5 \times G_0$ in the presence of an in-plane magnetic field as shown in Fig. 3.2. This 0.5 plateau at high magnetic fields is well understood in terms of noninteracting electrons. Due to the Zeeman term, see Eq. (3.2), the energy levels of electrons with opposite spins are shifted to $E_1 \pm E_Z/2$. Therefore electrons with different spins start to contribute to the conductance at different values of the chemical potential. Thus, at the 0.5 plateau the transport is spin-polarized and the width of the plateau is of the order of the Zeeman energy $E_Z = g\mu_B B$. Our result in Fig. 3.9 shows that the small shoulder at around $G = 0.65 \times G_0$ for $E_Z = 0$ evolves into a wide plateau at $G = G_0/2$, in line with experimental findings [37, 66–68, 74, 75]. Also the spin splitting models [101–103] and the Kondo model [97] obtain equivalent results.

For a more quantitative comparison between our results and experimental data it is useful to rescale our quantities and give the magnetic fields in units of Tesla. Therefore we have to associate an energy value with $E_1 = \hbar^2\pi^2/(2mW^2)$ by inserting the estimation $W \approx 40\,\mathrm{nm}$ from Eq. (3.6). The magnetic field is then given by

$$B = \frac{E_Z}{g\mu_B} = \frac{\hbar\pi^2}{eg(m/m_0)W^2}\frac{E_Z}{E_1}. \tag{3.19}$$

Using $m/m_0 = 0.07$ for GaAs [122] and $g = 1$ for the modified g-factor in the narrow channel limit [37, 66] we find that the highest magnetic field with $E_Z = 0.18\,E_1$

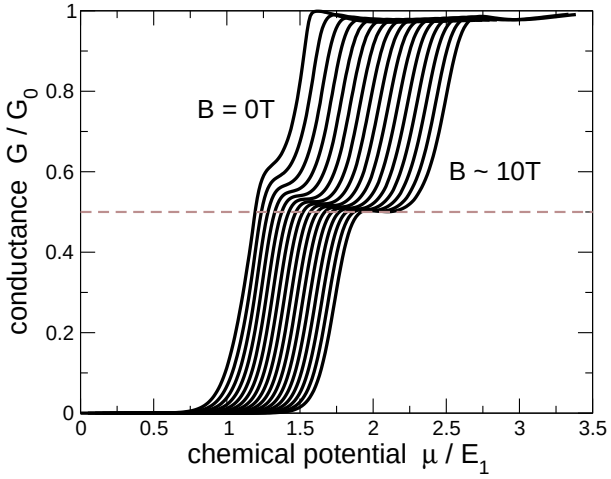

Figure 3.9: Conductance traces for increasing magnetic fields corresponding to $E_Z = 0 \ldots 0.18\,E_1$ in steps of $0.012\,E_1$ from left to right with $\gamma = 4.5 \times \hbar^2/(2m)$. The curves are horizontally offset by $0.05\,E_1$ for clarity.

corresponds to $B \approx 10\,\mathrm{T}$, comparable with the experimental findings.

In the regime of very high magnetic fields additional features appear in the conductance traces. When the Zeeman energy is comparable with the level spacing $E_2 - E_1$, the transverse energy levels carrying different spins intersect in a single particle picture, as sketched in Fig. 3.10. A setup where the level spacing is of the order of the

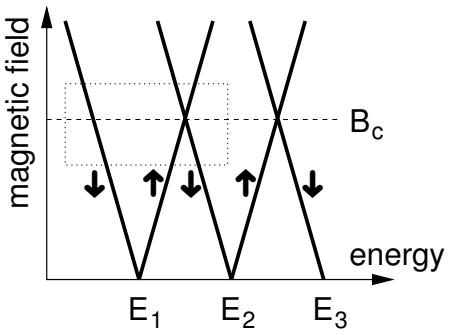

Figure 3.10: Sketch of the evolution of the transverse energy levels $E_n^{\uparrow,\downarrow}$ in a magnetic field. The dashed line marks the critical field where the crossing happens. The dotted rectangle indicates the parameter range plotted in Fig. 3.12.

Zeeman energy has to be wider than the above estimated value of 40 nm, so that the level splitting gets small enough. At the crossings the arrangement of energy levels is similar to that in the usual situation of the 0.7 anomaly: two energy levels carrying opposite spins are nearby and as the energy levels are populated, due to the repulsive interaction they can split. The interaction effects at the crossings of Zeeman split energy levels have been studied experimentally [79–81] and a conductance feature similar to the 0.7 structure, named the 0.7 analog, was found. The analog appears at conductance values around $(0.5 + 0.7) \times G_0 = 1.2 \times G_0$, as the $1\downarrow$ level is fully transmitting and the interactions involve only the $1\uparrow$ and $2\downarrow$ levels. In addition to the 0.7 analog, a complement structure is often present in experiments [79–81].

Our results in Fig. 3.11 exhibit a 0.7 analog structure at strong magnetic fields $E_Z/E_1 = 1.70 \ldots 1.93$. Going from small to large values of E_Z we see that the conductance plateau at G_0 becomes narrower and is shifted towards $1.5 \times G_0$ until it disappears at a value of $E_Z \approx 1.81\,E_1$. In that regime the observed structure is referred to as the 0.7 complement. By increasing the magnetic field further, the shoulder reappears and evolves back towards the plateau at G_0. Hence, in that range it has the same magnetic field dependence as the ordinary 0.7 anomaly, wherefore it is called 0.7 analog. The characteristics of the analog structure is in line with experimental observations [79–81], the complement structure, however, shows a different behavior. We find that the complement structure continuously rises from G_0 towards $1.5 \times G_0$, whereas in experiments it drops from G_0 to $0.5 \times G_0$ with increasing magnetic fields. The symmetry between analog and complement in our model can be understood from the arrangement of the energy levels. If the magnetic field is smaller than a critical field where the $1\uparrow$ and $2\downarrow$ levels cross, $E_Z \approx 1.81\,E_1$, the $2\downarrow$ level is energetically higher than the $1\uparrow$ level. As soon as the $1\uparrow$ level is populated, the $2\downarrow$ level rises in energy due to the repulsive interaction with the up-electrons in the system according to Eq. (3.11). In the case of magnetic fields which are higher than the critical field the energy levels change their roles and

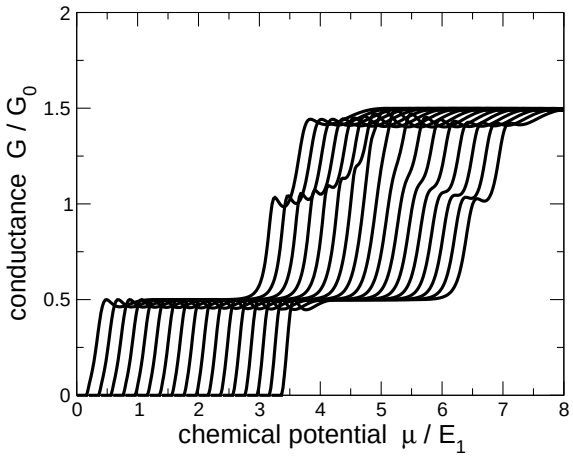

Figure 3.11: Conductance traces for increasing magnetic fields $E_Z/E_1 = 1.70 \ldots 1.93$ in steps of 0.014 from left to right with $\gamma = 4.5 \times \hbar^2/(2m)$. The different curves are horizontally offset by $0.2\,E_1$.

the $2\downarrow$ level is populated first. This causes the $1\uparrow$ to shift upward in energy. However this shift is smaller than for the case of the complement, since there are already down-electrons in the system from the occupied $1\downarrow$ level, resulting in a smaller relative change of the number of down-electrons. This consideration explains the symmetry between 0.7 analog and complement, and also the fact that the complement structure is more pronounced than the analog, as observed in Fig. 3.11.

A grayscale plot of the transconductance $\partial G/\partial\mu$ as shown in Fig. 3.12 visualizes the energy levels, which are sketched in Fig. 3.10. Here the dark colors mark the parameters where the transconductance is large, which is the case at the conductance steps. The light colors correspond to the plateaus, where the slope of G is small. Since the steps appear where the chemical potential crosses a transverse energy level, the dark regions in Fig. 3.12 indicate the location of the energy levels. The left dark stripe is the first step in the conductance corresponding to the $1\downarrow$ level. The two crossing branches in the center of Fig. 3.12 represent the $1\uparrow$ and $2\downarrow$ level. Both branches exhibit a discontinuity in the vicinity of the crossing: the $2\downarrow$ branch is discontinuous at a magnetic field slightly below the crossing, the $1\uparrow$ branch at fields slightly above. Such a discontinuity at the crossing of the different subbands is also found in the transconductance plots of the experimentalists [79–81], and it can be accounted for by DFT calculations [92] and the spin splitting model [103]. In the experiments, however, the $2\downarrow$ branch is continuous and the discontinuity only appears in the $1\uparrow$ branch. The observed discontinuity indicates a rearrangement of the energy levels close to the crossing and therefore favors the idea of spin splitting as the mechanism responsible for the 0.7 anomaly and the analog. Moreover, the fact that a 0.7 analog occurs at such high magnetic fields where Kondo correlations are assumed to be negligible and those analog structures are not accompanied by a zero-bias anomaly questions the Kondo interpretation of the 0.7 anomaly [79].

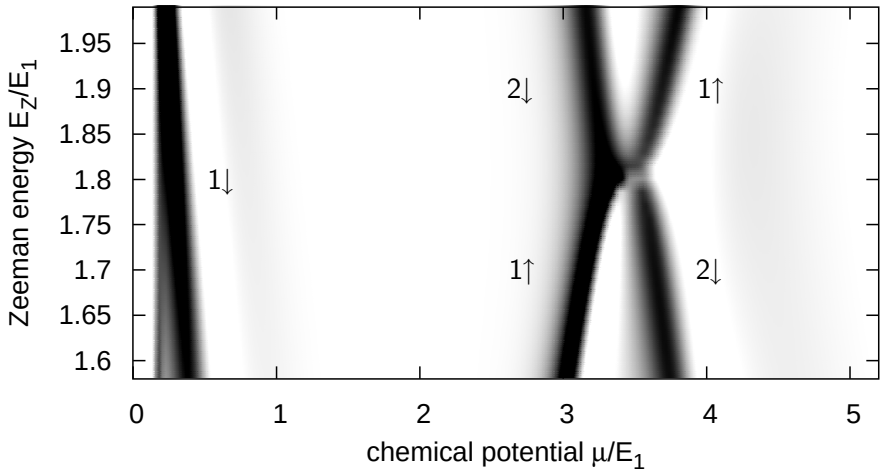

Figure 3.12: Transconductance $\partial G/\partial\mu$ as a function of the chemical potential and the Zeeman energy for $\gamma = 4.5 \times \hbar^2/(2m)$. Light colors refer to small values of $\partial G/\partial\mu$ (conductance plateau), and dark colors to large values (conductance step).

3.3.4 Zero field case

In the case of zero magnetic field the Hamiltonian (3.2) together with the interaction potential (3.11) is strictly symmetric with respect to the spin quantum number σ. Therefore the results in that case have to be identical for both spins. Indeed, the spin-resolved conductance curves of the zero field calculation show no difference as displayed by the dashed line in Fig. 3.13. A common way to break the symmetry is the application of a small magnetic field [89, 93, 95], what we used in the preceding sections. We now investigate the stability of the symmetric solution of the zero field case. For that purpose we apply a small magnetic field $E_Z/E_1 = 0.0015/s$ only during the first five iteration steps of the self-consistency procedure, where s labels the number of the iteration step. After the fifth self-consistency step we turn off the magnetic field $E_Z = 0$ and continue the iteration until convergence is reached. The results in Fig. 3.13 show that this disturbance is sufficient to obtain an asymmetric solution with respect to the different spins. The conductance traces are aligned with the zero field curves for low chemical potentials μ. When the first conductance channel opens the up- and down-contributions start to split at $\mu = 1.18\,E_1$ resulting in a 0.7 structure in the total conductance. At chemical potentials above the first conductance step the spin splitting vanishes. In total, the resulting conductance curve is very similar to that obtained for a static magnetic field in Fig. 3.6. The main difference is the abrupt onset of spin splitting compared to the static case. Hence, the symmetric solution is unstable against any small disturbance of the balance between up- and down-electrons, which may lead to a spontaneous spin polarization in an energy range where the first channel opens.

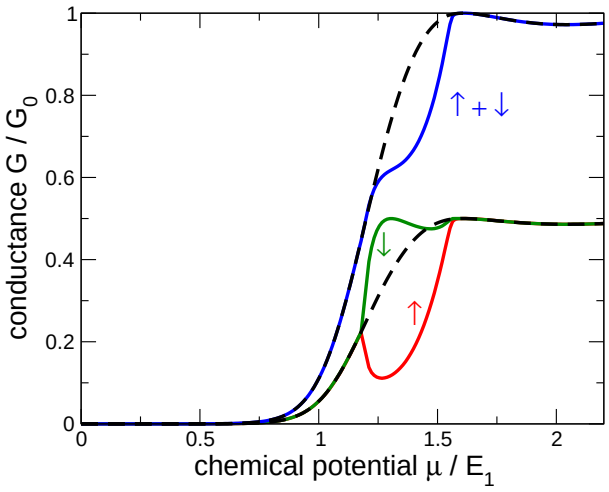

Figure 3.13: The spin-resolved conductance (lower dashed line), which is identical for both spin orientations, and the total conductance (upper dashed line) for $B = 0$. The red and green lines show the up-and down-contribution to the conductance after a small magnetic disturbance (see text), the blue line represents the total conductance in that case. The interaction strength is $\gamma = 4.5 \times \hbar^2/(2m)$.

In our numerical results the down-contribution of the conductance dominates as we apply a positive magnetic field. Changing the sign of the magnetic field the different spin directions would change their roles, but the total conductance is unaffected. In an experimental situation there are various possible mechanisms that can cause an imbalance in the number of up- and down-electrons. Residual magnetic fields in the experimental setup or temporal current fluctuations might change the ratio of electrons with opposite spins. Also spin-orbit interaction or magnetic impurities as well as nuclear spins and dynamic nuclear polarization can cause a small spin splitting in the system. Due to the instability of the spin symmetric solution, any small imbalance of up- and down-electrons in the device is sufficient to obtain spin splitting and observe a 0.7 anomaly.

3.3.5 Shot noise

Shot noise denotes the current fluctuations which arise due to the discreteness of the electric charge. In a quantum transport experiment of single electrons across a scatterer with transparency $\mathcal{T}$ we can only give a probabilistic prediction about the outcome. The average fraction of transmitted particles is given by $\mathcal{T}$, but due to the stochastic nature of the transmission process there are fluctuations around the expectation value. The origin of shot noise therefore is the partitioning of an incoming beam of particles into a transmitted and reflected one. Thus shot noise is also referred to as *partition noise*. In order to quantify the noise let us consider a single channel transport

experiment across a barrier with transmission probability $\mathcal{T}$. The occupation of the transmitted channel will be denoted by n_T, where due to the Pauli principle the possible values are $n_T \in \{0, 1\}$ for a single transmission event. For that reason we obtain the relation

$$n_T^2 = n_T. \tag{3.20}$$

In the case of a continuous beam of incoming electrons the average occupation $\langle n_T \rangle$ of the transmitting channel is determined by the transmission,

$$\langle n_T \rangle = \mathcal{T}. \tag{3.21}$$

The magnitude of the fluctuations around the expectation value is given by

$$\langle n_T^2 \rangle - \langle n_T \rangle^2 = \langle n_T \rangle - \langle n_T \rangle^2 = \mathcal{T} - \mathcal{T}^2 = \mathcal{T}(1 - \mathcal{T}), \tag{3.22}$$

where we made use of Eqs. (3.20) and (3.21). Hence, the noise is maximal for $\mathcal{T} = 1/2$ and it vanishes for $\mathcal{T} = 0$ and $\mathcal{T} = 1$, as in that cases there is no partitioning taking place and all incoming particles are either reflected or transmitted.

The above considerations can be generalized to an arbitrary multi-channel two-terminal device within the framework of the Landauer-Büttiker theory [123], where the noise power takes the form

$$S = \frac{2e^2}{h} \sum_{n,\sigma} \int \mathrm{d}E \; \mathcal{T}_{n,\sigma}(E) \Big(1 - \mathcal{T}_{n,\sigma}(E)\Big) \Big(f_L(E,\mu) - f_R(E,\mu)\Big)^2. \tag{3.23}$$

Here, $f_{L(R)}$ is the Fermi distribution function of the left (right) contact and $\mathcal{T}_{n,\sigma}$ denotes the transmission probability of a particle with spin σ in eigenchannel n. If the energy scale on which the transmission functions $\mathcal{T}_{n,\sigma}(E)$ vary is large compared to the temperature $k_B T$ and the applied source-drain voltage eV, the transmissions can be treated as constants. Then the energy integral over the distribution functions can be performed, yielding

$$S = 2\mathcal{N} \frac{2e^2}{h} \left[eV \coth\left(\frac{eV}{2k_B T}\right) - 2k_B T \right], \tag{3.24}$$

with the noise factor defined as

$$\mathcal{N} = \frac{1}{2} \sum_{n,\sigma} \mathcal{T}_{n,\sigma}(1 - \mathcal{T}_{n,\sigma}). \tag{3.25}$$

The noise factor is the multi-channel generalization of Eq. (3.22). An equivalent quantity to measure the noise is the so-called Fano factor

$$\mathcal{F} = \frac{\sum_{n,\sigma} \mathcal{T}_{n,\sigma}(1 - \mathcal{T}_{n,\sigma})}{\sum_{n,\sigma} \mathcal{T}_{n,\sigma}}, \tag{3.26}$$

which is normalized to Schottky's noise result of uncorrelated particles [123].

If we restrict ourselves to the single mode case with two spin directions, which is the interesting regime for the 0.7 anomaly, the noise factor reduces to

$$\mathcal{N} = \frac{1}{2}\big[\mathcal{T}_\uparrow(1-\mathcal{T}_\uparrow) + \mathcal{T}_\downarrow(1-\mathcal{T}_\downarrow)\big]. \tag{3.27}$$

Simultaneous measurements of the noise and the conductance of a quantum system provide information about the spin polarization in the system. The conductance is proportional to the total transmission irrespective of the individual contributions of the up- and down-electrons. Defining the mean transmission

$$\bar{\mathcal{T}} = \frac{1}{2}\big(\mathcal{T}_\uparrow + \mathcal{T}_\downarrow\big) \tag{3.28}$$

the conductance may be written as $G = G_0\bar{\mathcal{T}}$, see Eq. (2.126). The noise factor, Eq. (3.27), in terms of $\bar{\mathcal{T}}$ reads

$$\mathcal{N} = \bar{\mathcal{T}}\big(1-\bar{\mathcal{T}}\big) - \frac{1}{4}\big(\mathcal{T}_\uparrow - \mathcal{T}_\downarrow\big)^2, \tag{3.29}$$

where the second term is directly related to the spin polarization. In the case of unpolarized transmission $\mathcal{T}_\uparrow = \mathcal{T}_\downarrow = \bar{\mathcal{T}}$ the noise factor is given by the first term of Eq. (3.29), $\mathcal{N} = \bar{\mathcal{T}}\big(1-\bar{\mathcal{T}}\big)$. In the presence of spin polarization the noise factor acquires a negative correction of $\frac{1}{4}\big(\mathcal{T}_\uparrow - \mathcal{T}_\downarrow\big)^2$. In an analog way the Fano factor in the single mode case can be rewritten in the form

$$\mathcal{F} = \big(1-\bar{\mathcal{T}}\big) - \frac{\big(\mathcal{T}_\uparrow - \mathcal{T}_\downarrow\big)^2}{4\bar{\mathcal{T}}}, \tag{3.30}$$

where also the second term represents a correction due to polarized transmission.

We now write down the noise factor and the Fano factor in the two limiting cases of unpolarized and fully polarized transmission. In the former case the spin-resolved transmissions are identical, $\mathcal{T}_\uparrow = \mathcal{T}_\downarrow = \bar{\mathcal{T}}$, and in both equations (3.29) and (3.30) the second term vanishes. So we end up with

$$\mathcal{N}_{\text{unpol}} = \bar{\mathcal{T}}\big(1-\bar{\mathcal{T}}\big) \quad \text{and} \quad \mathcal{F}_{\text{unpol}} = \big(1-\bar{\mathcal{T}}\big) \tag{3.31}$$

for the case of unpolarized transmission. The contrary situation of fully polarized transmission is characterized by the fact that up-electrons start to contribute to the conductance when the down-channel is already fully transmitting,

$$\begin{aligned} &\mathcal{T}_\uparrow = 0 \quad \text{and} \quad \mathcal{T}_\downarrow = 2\bar{\mathcal{T}} \qquad \text{for} \quad \bar{\mathcal{T}} < 1/2 \\ &\mathcal{T}_\uparrow = 2\bar{\mathcal{T}} - 1 \quad \text{and} \quad \mathcal{T}_\downarrow = 1 \quad \text{for} \quad \bar{\mathcal{T}} > 1/2. \end{aligned} \tag{3.32}$$

Using these relations we find for the noise factor and the Fano factor in the polarized case

$$\mathcal{N}_{\mathrm{pol}} = \begin{cases} \bar{\mathcal{T}}\left(1-2\bar{\mathcal{T}}\right) & \text{for} \quad \bar{\mathcal{T}} < 1/2 \\ 3\bar{\mathcal{T}} - 2\bar{\mathcal{T}}^2 - 1 & \text{for} \quad \bar{\mathcal{T}} > 1/2 \end{cases}$$
$$\mathcal{F}_{\mathrm{pol}} = \begin{cases} 1-2\bar{\mathcal{T}} & \text{for} \quad \bar{\mathcal{T}} < 1/2 \\ 3-2\bar{\mathcal{T}} - 1/\bar{\mathcal{T}} & \text{for} \quad \bar{\mathcal{T}} > 1/2. \end{cases} \tag{3.33}$$

If the transmission is partially polarized the corresponding noise and Fano factors are expected to have values in between the two limiting results stated in Eqs. (3.31) and (3.33).

In recent experiments the shot noise characteristics of quantum point contacts exhibiting a 0.7 anomaly was investigated [76–78]. In the earlier work [76] the authors show the Fano factor in the range of the first conductance step for different magnetic fields. Their result is shown in Fig. 3.14(b), where the plotted quantity F^+ is an upper bound of the Fano factor, and the white circles correspond to data including thermal noise. They find a suppression of noise at conductance values around $0.7 \times G_0$, which gets stronger with increasing magnetic field. In subsequent experiments [77, 78] the noise factor was measured by fitting the current fluctuations with Eq. (3.24) using $\mathcal{N}$ as fitting parameter. The result depicted in Fig. 3.15(b) also shows a suppression of the noise in the regime of the 0.7 structure in agreement with the previous experiment. By applying strong magnetic fields the noise factor converges towards the values for fully polarized transmission given by Eq. (3.33).

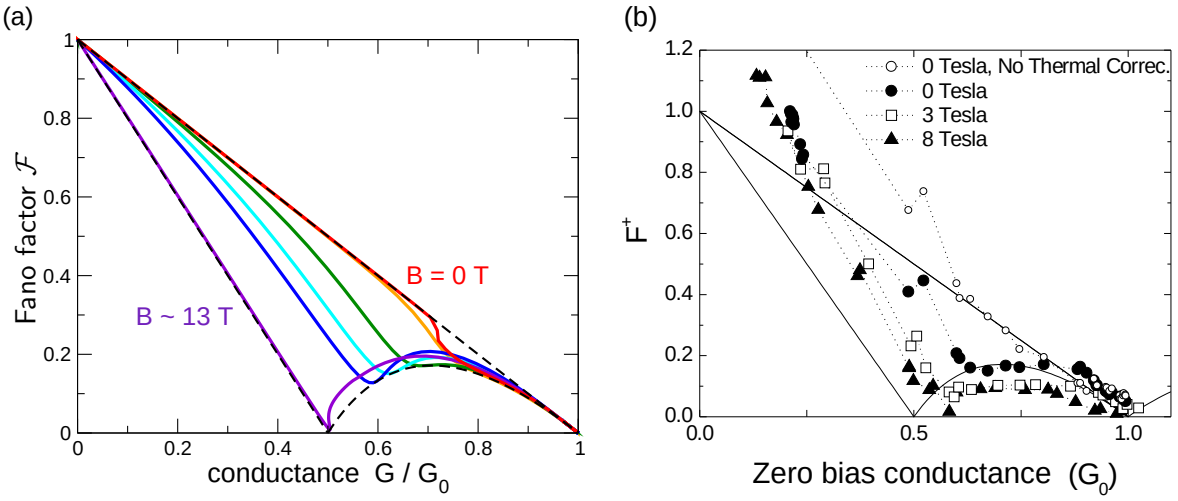

Figure 3.14: (a) Fano factor for $\gamma = 4.0 \times \hbar^2/(2m)$ and different magnetic fields with Zeeman energies $E_Z/E_1 = 0.0,\ 0.0015,\ 0.012,\ 0.023,\ 0.035,\ 0.23$ from top to bottom. The upper dashed line corresponds to unpolarized transmission, Eq. (3.31), the lower dashed line to fully polarized transmission, Eq. (3.33). (b) Experimental result for the Fano factor from [76].

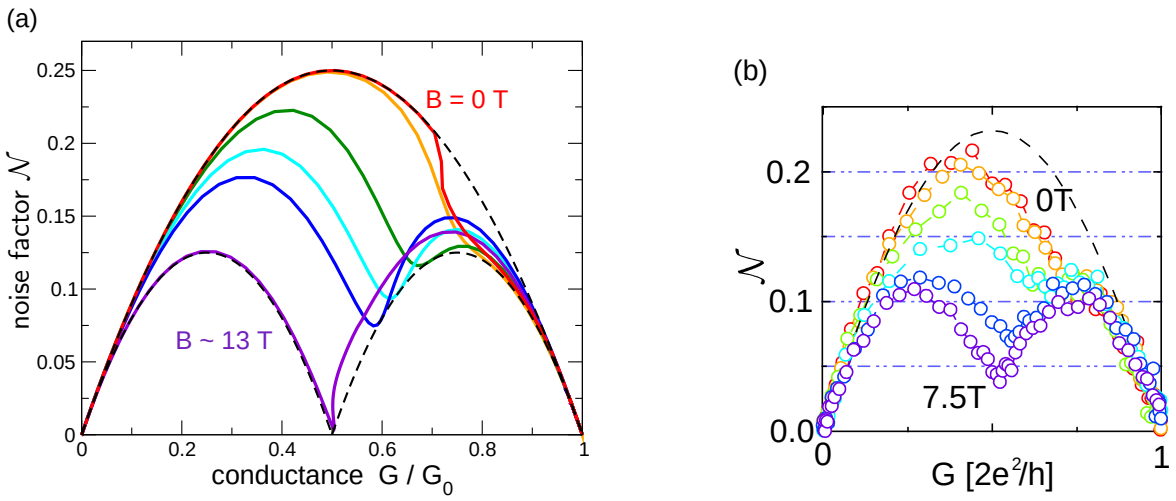

Figure 3.15: (a) Noise factor for the same parameters as described in the caption of Fig. 3.14. The dashed lines show the noise factor for unpolarized and fully polarized transmission, according to Eqs. (3.31) and (3.33). (b) Experimental result for the noise factor from [77].

The Fano factor and noise factor obtained within our model are depicted in Figs. 3.14(a) and 3.15(a) as a function of $G/G_0 = \bar{\mathcal{T}}$. We see that for $B = 0$ the Fano factor and noise factor follow the analytical curve for unpolarized transmission in the regime of low conductances. For conductance values $G \geq 0.7 \times G_0$ the noise is suppressed indicating a partially spin-polarized transmission of electrons according to Eqs. (3.29) and (3.30). By applying a magnetic field the polarization in the system increases. The noise factor evolves from an asymmetric single dome to a symmetric double dome shape and eventually converges towards the values of fully polarized transmission for strong magnetic fields. The Fano factor exhibits the same crossover from partial to full polarization with increasing magnetic field. The maximum B-field in the above results with $E_Z = 0.23\, E_1$ is of the order of $B \approx 13\,\mathrm{T}$, according to Eq. (3.19). The high field curves show a small ambiguousness close to $G = G_0/2$, which is due to resonances in the conductance curves. Such resonances are common for the transmission across barriers or non-uniform geometries. They appear in the conductance traces of noninteracting particles in Fig. 3.6, and also occur at the 0.5 plateau in the high field regime, so that the noise and Fano factors can have two different values for one conductance value close to $G = 0.5 \times G_0$ leading to the observed structure in the noise data for $E_Z = 0.23\, E_1$.

The obtained numerical results are in very good agreement with experimental observations, both for the Fano factor [76] and the noise factor [77, 78]. The shot noise characteristics can also be accounted for by Reilly's spin splitting model [102, 103] where the results are shown in Refs. [77, 78]. However, the observed shot noise suppression at the 0.7 anomaly does not necessarily provide evidence for the presence of a static spin polarization, as also in the framework of the Kondo model the shot noise characteristics can be reproduced [100].

3.3.6 Temperature dependence

The 0.7 anomaly is accompanied by a peculiar temperature dependence: within a certain range the 0.7 plateau gets more pronounced if the temperature is increased [37, 66, 68, 69, 74, 76]. This behavior can be reproduced by the spin splitting models [101, 102] as well as by the Kondo model [97] and by the consideration of electron-phonon interactions [104]. However, to our knowledge there are no DFT results exhibiting such a temperature behavior [89].

For treating finite temperatures, the conductance formula (2.127) has to be modified. Starting from the Landauer formula for the current, Eq. (2.146), for a small applied bias V we get for one spin component σ

$$I_\sigma = \frac{e}{h} \int \mathrm{d}E\, \mathcal{T}_\sigma(E) \big[f(E - eV/2, \mu) - f(E + eV/2, \mu) \big]. \tag{3.34}$$

After a Taylor expansion of the Fermi functions appearing in the current formula we get for the conductance

$$G_\sigma = \frac{I_\sigma}{V} = \frac{e^2}{h} \int \mathrm{d}E\, \mathcal{T}_\sigma(E) \left(-\frac{\partial f(E, \mu)}{\partial E} \right). \tag{3.35}$$

The derivative of the Fermi function is peaked around the chemical potential μ and has a width of the order of $k_B T$. Hence, the transmission function for energies within a few $k_B T$ around the chemical potential contributes to the conductance in the finite temperature regime. In the limit $T \to 0$ the factor $(-\partial f / \partial E)$ converges towards the delta function $\delta(E - \mu)$ and we recover the regular Landauer conductance formula (2.127). The second point where the temperature enters is the calculation of the particle density by means of Eq. (2.116). Due to the dissipation-fluctuation theorem (2.27) and the connection with the local density of states $d(\vec{r}, E)$, Eq. (2.105), the particle density can be expressed by an integral over the local density of states

$$n(\vec{r}) = \int \mathrm{d}E\, d(\vec{r}, E) f(E, \mu). \tag{3.36}$$

At $T = 0$ the Fermi function truncates the integral at $E = \mu$, whereas for finite temperatures this cutoff is smoothed out within an energy range of a few $k_B T$ around the chemical potential.

If we include finite temperatures in our calculations we find a reduction of the spin splitting as shown in Fig. 3.16. The difference between the transmission of up- and down-electrons is reduced with increasing temperature which makes the 0.7 plateau less pronounced. This result contradicts the experimental findings. As DFT calculations are also not able to capture this phenomenon it is possible that a mean-field description is not sufficient to explain the temperature dependence. There are recent approaches beyond mean-field that qualitatively get the correct temperature behavior [112, 113]. On the one hand it was shown that the consideration of relaxation processes in the

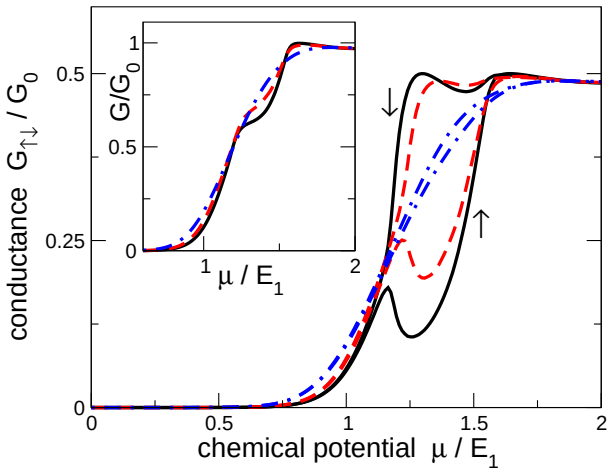

Figure 3.16: The conductance contributions $G_\uparrow$ and $G_\downarrow$ for interaction constant $\gamma = 4.5 \times \hbar^2/(2m)$ and for different temperatures $k_BT = 0$ (solid black line), $k_BT = 0.029\,E_1$ (dashed red line), and $k_BT = 0.058\,E_1$ (dashed-dotted blue line). The inset shows the corresponding total conductance $G = G_\uparrow + G_\downarrow$.

leads can give a temperature correction in the right direction [112]. For an applied source-drain bias electrons are injected into the outgoing lead with energies above the bias-shifted Fermi level. They equilibrate within a characteristic time scale τ in order to restore the thermodynamic equilibrium distribution given by the Fermi function. For delta-like electron-electron interactions, which are restricted to the center of the constriction of a quantum point contact, this relaxation gives a correction to the conductance proportional to $-T^2$, which is strongly enhanced for conductance values $0.5 \leq G/G_0 \leq 1.0$. On the other hand also non momentum-conserving interaction processes can give a conductance correction proportional to $-T^2$ [113]. This follows from second order perturbation theory of the electron-electron interaction for that type of processes.

In contrast to our approach, the spin splitting models qualitatively yield the correct temperature dependence [101, 102]. In the model approach, however, the temperature affects only the computation of the conductance whereas the spin splitting is assumed to be temperature independent. In our calculation the temperature also enters in the computation of the electron density, see Eq. (3.36), where energies up to several k_BT above the Fermi level contribute. Hence, the densities and thus the interaction potentials depend on the temperature which results in a temperature dependent spin splitting. The spin gap vanishes at temperatures $k_BT \approx 0.08\ E_1$. Second, the spin splitting models assume sharp energy levels with step-like transmission functions $T_\sigma(E) = \Theta(E - E_\sigma)$, where $\Theta(x)$ is the Heaviside step-function. Finite temperatures lead to a smearing of the conductance and, according to Ref. [101], a 0.7 structure is found for temperatures smaller than the spin gap, $k_BT < |E_\uparrow - E_\downarrow|$. In our model the energy levels exhibit a

broadening due to the geometry of the system even at zero temperature, $k_BT = 0$. The broadening is of the order $E_1/2$ (see e.g. Fig. 3.6), larger than the level splitting (see Fig. 3.7). Hence, allowing for finite temperatures the broadening is further enhanced which leads to a decrease of the 0.7 plateau.

3.4 Connection with Coulomb interaction

Recalling the estimations of the typical width of the constriction in a quantum point contact $W \approx 40\,\mathrm{nm}$ and the Thomas-Fermi screening length in a 2DEG $\lambda_S \approx 5\,\mathrm{nm}$, see Sec. 3.2, the assumption of a delta-like interaction potential might seem too crude for the description of such systems. For that reason we also performed simulations with full Coulomb interactions in Hartree-Fock approximation. Like in the previous calculations the interaction is switched on and off within the narrowing part of the geometry in Fig. 3.3. The corresponding interaction self-energy is derived in Appendix A and is usually written as a sum of the Hartree term

$$\Sigma^H_{\mathrm{int}}(\vec{r}_1, \vec{r}_2) = \delta(\vec{r}_1 - \vec{r}_2)\, \frac{e^2}{4\pi\varepsilon\varepsilon_0} \sum_{\sigma'} \int \mathrm{d}^2 r' \frac{n_{\sigma'}(\vec{r}\,')}{|\vec{r}_1 - \vec{r}\,'|}, \tag{3.37}$$

which gives the classical Coulomb interaction of an electron at $\vec{r}_1$ with the electron distribution in the system, see Eq. (A.11), and the Fock term

$$\Sigma^{F,\sigma}_{\mathrm{int}}(\vec{r}_1, \vec{r}_2) = -\frac{e^2}{4\pi\varepsilon\varepsilon_0} \int \frac{\mathrm{d}E'}{2\pi\hbar}\, \frac{(-\mathrm{i}\hbar)\mathcal{G}^<_{\sigma,\sigma}(\vec{r}_1, \vec{r}_2; E')}{|\vec{r}_1 - \vec{r}_2|}, \tag{3.38}$$

which accounts for the exchange interactions. Whereas both contributions to the interaction self-energy are diagonal in the case of a delta potential, the Fock self-energy is non-diagonal for Coulomb interaction. Therefore, the recursive strategy to evaluate the retarded Green function cannot by applied, see Appendix B. Instead, the matrix inversion in Eq. (3.14) to obtain $\mathcal{G}^r$ has to be performed in one step, which results in an enormous increase of the computation time. In order to reduce the numerical effort we doubled the lattice constant $a \to 2a$ for the geometry shown in Fig. 3.3, so that the size of the Hamiltonian matrix and the Green function is scaled down to about one quarter of the original size.

The dimensionless coupling constant γ_C for Coulomb interaction is defined in the following chapter in Eq. (4.18)

$$\gamma_C = \frac{2ma}{\hbar^2} \frac{e^2}{4\pi\varepsilon\varepsilon_0}. \tag{3.39}$$

It scales with the lattice constant a and can be estimated to $\gamma_C \approx 0.9$ for GaAs parameters $m = 0.07 m_0$ and $\varepsilon = 13$ [122]. For the estimation we used $a = 4.4\,\mathrm{nm}$, which corresponds to a constriction width of 40 nm. The results obtained for different interaction constants are shown in Fig. 3.17, where the values of γ_C were below the

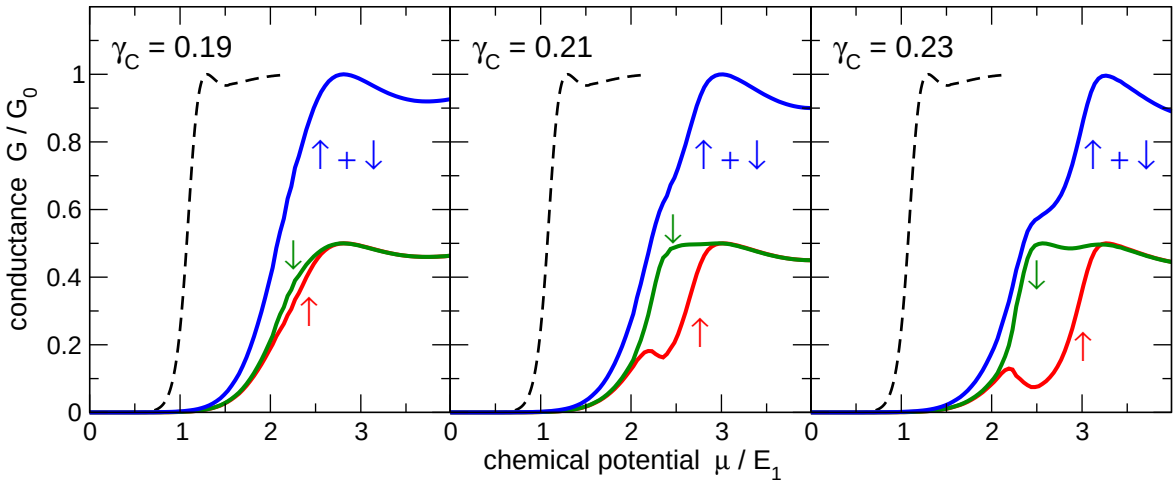

Figure 3.17: Spin-resolved conductance traces for different interaction strengths $\gamma_C = 0.19$, $\gamma_C = 0.21$, and $\gamma_C = 0.23$ from left to right. The green and red curves are the up- and down-contributions, respectively, and the blue lines show the total conductances. The dashed black curve shows the conductance of noninteracting electrons.

estimated value. So even in the presence of screening of the exchange splitting, which is induced by higher order corrections of the interaction beyond the Hartree-Fock level, a comparable spin splitting may be obtained by larger values of γ_C. The resulting conductance curves in Fig. 3.17 show a similar behavior as the results for delta interactions displayed in Fig. 3.6. With increasing coupling constant the difference in the up- and down-contribution of the conductance gets more pronounced. At the same time a shoulder evolves in the total conductance. Compared to the previous results for contact interactions in Fig. 3.6 the conductance curves are shifted towards higher values of the chemical potential μ. As we do not assume any kind of screening, there is a cutoff for the range of the Coulomb potential only through the size of the system. This leads to a larger effective screening length compared to the Thomas-Fermi length, Eq. (3.5), giving an enhanced total interaction energy, see Eq. (3.9), which explains the shift in the conductance curves.

Furthermore, we did simulations where we replaced the Coulomb interaction by a Yukawa potential $w(\vec{r},\vec{r}\,') \sim \mathrm{e}^{-|\vec{r}-\vec{r}\,'|/\lambda}/|\vec{r}-\vec{r}\,'|$ with different screening lengths λ. We found that with decreasing screening length λ the results continuously evolve towards the results obtained for delta interactions. So the effect of spin splitting remains robust even in the limit without screening. This suggests that the central mechanism responsible for spin splitting is the repulsive interaction between electrons with different spins, which is the only kind of interaction present in the short-range limit, see Eq. (3.11). Also in the case of Coulomb interaction there is a contribution of the interaction potential which is proportional to the density of the particles with opposite spin. Writing the Hartree self-energy (3.37) in discretized form we get for the short-range contribution

of the integral

$$\left[\Sigma_{\mathrm{int}}^{H}\right]_{i,j}^{\mathrm{short}} = \delta_{i,j}\frac{e^2}{4\pi\varepsilon\varepsilon_0}\frac{1}{a}\,C\sum_{\sigma'}\tilde{n}_{\sigma'}(\tilde{\vec{r}}_j), \tag{3.40}$$

where $C \approx 3.525$ comes from the integration of the interaction potential over one lattice cell of area a^2 around $\vec{r}_j$, see Eq. (4.16). Analogously, we find for the short-range part $i = j$ of the Fock self-energy

$$\left[\Sigma_{\mathrm{int}}^{F,\sigma}\right]_{i,j}^{\mathrm{short}} = -\delta_{i,j}\frac{e^2}{4\pi\varepsilon\varepsilon_0}\frac{1}{a}\,C\tilde{n}_{\sigma}(\tilde{\vec{r}}_j), \tag{3.41}$$

where we replaced $-i/(2\pi)\int \mathrm{d}E'\mathcal{G}^{<}_{\sigma,\sigma}(\vec{r},\vec{r};E')$ by the electron density $n_\sigma(\vec{r})$, according to Eq. (2.116). Hence, in the short-range contribution of the Coulomb potential we find a cancellation of the interaction self-energy of equal spins, leading to

$$\left[\Sigma_{\mathrm{int}}^{\sigma}\right]_{i,j}^{\mathrm{short}} = \delta_{i,j}\frac{Ce^2}{4\pi a\varepsilon\varepsilon_0}\,\tilde{n}_{-\sigma}(\tilde{\vec{r}}_j), \tag{3.42}$$

similar to the self-energy (A.14) we obtain for delta-like interactions. In addition there are the long-range contributions of the Coulomb potential to both the Hartree and the Fock self-energies. In the case of screened Coulomb interactions the long-range part gets smaller for shorter and shorter screening lengths λ. In the limit $\lambda \to 0$ only the short-range contribution of the interaction potential given in Eq. (3.42) remains. Due to the qualitative agreement of the results obtained with delta interactions and Coulomb interactions we may conclude that the repulsion between electrons with opposite spins, which is present in both types of interaction, is responsible for the appearance of spin splitting.

3.5 Discussion

3.5.1 General features of the model

The presented model describes transport of locally interacting electrons. In Hartree-Fock approximation only electrons with different spins are interacting repulsively. This suggests a very intuitive physical picture: if the scattering region is predominantly occupied by one spin species, electrons with the opposite spin are repelled from the constriction. So this kind of interaction favors an asymmetric population of the quantum point contact with respect to the different spins. Despite its simplicity the model is adequate to qualitatively explain different aspects of the 0.7 anomaly. We show how the interaction can cause an asymmetry between the spin-up and spin-down transmission resulting in a shoulder in the total conductance. We find a spin splitting in the energy levels which results in a local spin polarization inside the quantum point contact. The magnetic field dependence of the 0.7 feature is well reproduced and for

strong magnetic fields the conductance traces show additional features resembling the so-called 0.7 analog. At zero magnetic field we find an instability phenomenon which may lead to a spontaneous spin polarization. Our model also accounts for the shot noise suppression at the 0.7 plateau and both the Fano factor and the noise factor are in good agreement with experimental observations.

It is known that the Hartree-Fock approximation usually overestimates the effect of exchange interactions [85]. Therefore one expects that spin splitting is weakened if corrections beyond Hartree-Fock are included. For a two-site model with Hubbard-like interactions coupled to leads the spin splitting, which is present in the mean-field description, even vanishes after employing exact methods [124]. This is in accordance with the Lieb-Mattis theorem [125], which forbids a ferromagnetic ground state for strictly one dimensional systems. In the experimental situation, however, the geometry is quasi-one-dimensional, where the wave functions are spread over a finite width in the transverse directions. Such systems may exhibit magnetic features [105–107]. It was shown by exact methods that Hubbard chains that are not restricted to one dimension can have a ferromagnetic ground state [109, 126]. So in our system, which is based on a two-dimensional description, a spin-polarized ground state is possible. For both short-range interactions and Coulomb interaction the coupling constant used in the calculations was smaller than the estimated value, see Eqs. (3.10) and (3.39). Therefore, if part of the exchange interaction is screened by higher order corrections, the results concerning spin splitting may be restored by the assumption of a stronger interaction constant.

In our calculations we did not consider the influence of background charges so far. In the case of ultracold fermionic atoms, which is discussed later in Sec. 3.5.3, there are no charges involved at all, so the interaction is fully covered by Eq. (3.4). For the case of electrons in a 2DEG, however, there are the positively charged ions of the donors, which generate an additional electrostatic potential. To study the consequences of background charges we performed simulations with a constant background charge density n_{BG} which exactly compensates the total number of electrons in the system

$$\int \mathrm{d}^2 r \, n_{\mathrm{BG}} = \int \mathrm{d}^2 r \, n(\vec{r}), \tag{3.43}$$

giving rise to an electrically neutral device. Therefore, n_{BG} also has to be adjusted self-consistently, and the effective interaction potential, Eq. (3.11), has to be modified to $V^{\sigma}_{\mathrm{int}}(\vec{r}) = \gamma[n_{-\sigma}(\vec{r}) - n_{\mathrm{BG}}]$. The outcome of the calculations including a constant background charge density in Fig. 3.18 shows that the qualitative nature of the results concerning spin splitting and the 0.7 feature remains unchanged. In the absence of background charges we find a shift of the conductance curves towards higher energies, compared to the results of noninteracting electrons, see also Fig. 3.6. This is due to the interaction potential $V_{\mathrm{int}}(\vec{r})$ acting like an extra barrier with an average height proportional to the total number of electrons in the system. With the inclusion of a positive charge background the total number of charges in the system and therefore

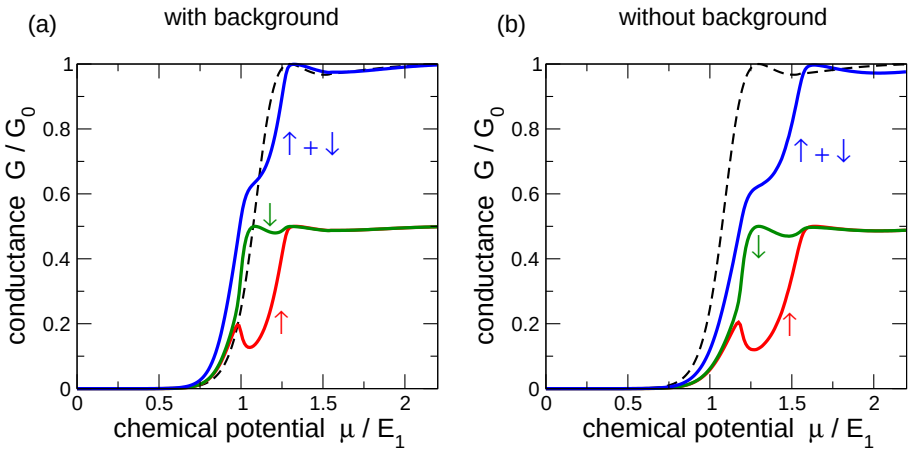

Figure 3.18: (a) Spin-resolved conductance curves including a constant background charge density. (b) Conductance traces without background charges, same as in Fig. 3.6. The green and red curves are the up- and down-contributions, respectively, and the blue lines show the total conductances. The dashed black curve shows the conductance of noninteracting electrons. In both cases the interaction constant is $\gamma = 4.5 \times \hbar^2/(2m)$.

also the average height of the barrier is zero. Hence, the first conductance step is located at a chemical potential comparable to the noninteracting case, see Fig. 3.18(a).

3.5.2 Limitations of the model

Although many features of the 0.7 anomaly can be successfully reproduced by our model, there are some aspects beyond the capability of our approach. The most important one is the temperature dependence of the 0.7 feature which is not correctly accounted for in our results. Whereas the experimentalists see an emphasis of the 0.7 plateau with increasing temperature, in our results the 0.7 feature is smeared out and vanishes at finite temperatures. The fact that DFT results on the T-dependence are similar to ours suggests that the weakening of the 0.7 structure might be a common problem of mean-field approaches. This assumption is confirmed by approaches beyond mean-field, that are able to reproduce the correct tendency of the conductance for finite temperatures. There is the Kondo model [97] that predicts a widening of the 0.7 plateau for increasing temperature. Also transport calculations including second order interaction effects for non momentum-conserving processes [113] find T-dependent corrections of the conductance in the right direction. Moreover, the consideration of relaxation processes of the electrons in the leads [112] can reproduce the observed temperature dependence. In a complementary approach, interactions with phonons were used to explain the temperature behavior of the 0.7 anomaly [104]. Thus, there are various approaches beyond the scope of our model giving a possible explanation of the temperature induced enhancement of the 0.7 structure.

Another drawback of our model can be found in the description of the high magnetic field regime. Although our results nicely reproduce the 0.7 analog structure in qualitative agreement with experimental findings [79–81], it fails to explain the complement structure, which is often present in experiments. The 0.7 complement is a small shoulder that evolves from a conductance value of G_0 down to $0.5 \times G_0$ with increasing magnetic field. In our results it shows the opposite tendency and develops upwards to $1.5 \times G_0$. Also the grayscale plot of the transconductance in the high field regime, Fig. 3.12, shows details deviant from experimental results. In agreement with measurements [79–81], with DFT results [92], and the spin splitting model [103] we find a discontinuity in the transconductance close to the crossing of the $1\uparrow$ and the $2\downarrow$ levels. The discontinuity appears in both branches to the right of the crossing, whereas in experiments the $2\downarrow$ branch is found to be continuous. Also in the DFT and spin splitting results the discontinuity appears only in the $1\uparrow$ branch. Our results reflect the symmetry of the model with respect to magnetic field strengths above and below the level crossing. This also leads to the symmetry of the 0.7 analog and complement.

The differential conductance $\partial I/\partial V$ of quantum point contacts often exhibits a peak at zero source-drain bias $V = 0$, the so-called zero-bias anomaly. This peak cannot be reproduced by our model and besides the Kondo model none of the standard approaches can describe this phenomenon. Due to the similarity with the Kondo effect in quantum dots [119], the finding of the zero bias anomaly was interpreted as a strong argument in favor of Kondo physics. In a recent work it was shown that only second order perturbation theory in the interaction is sufficient to account for a zero-bias anomaly, if non momentum-conserving processes are considered [113]. Moreover, there are experimental results questioning the Kondo interpretation of the 0.7 anomaly. On the one hand, a stationary spin-polarized current was measured in the regime of the 0.7 structure [75], in contradiction to a dynamic spin polarization in the case of Kondo physics. On the other hand, at high magnetic fields, where Kondo correlations are expected not to play a role, 0.7 analogs can be observed [79–81], which are not accompanied by a zero-bias anomaly. In very recent measurements the dependence of the 0.7 anomaly on the lateral position of the one-dimensional wire in the 2DEG was investigated by applying different voltages to both split gates separately [83]. It was found that the 0.7 structure remains rather stable, whereas the zero-bias peak changes its structure and can even vanish, depending on the position. This indicates that both features, the 0.7 anomaly and the zero-bias anomaly, are rather independent from each other than caused by a common mechanism.

3.5.3 Transport of cold fermionic atoms

The introduced model of interacting particles was used to describe electrons in the presence of an efficiently screened Coulomb interaction. Moreover, the Hamiltonian (3.2) with the delta-like interaction potential, Eq. (3.4), is particularly devised to describe ultracold fermionic atoms. Due to the charge neutrality there are no long-range interactions between the atoms. Only contact interactions play a role, which occur

when atoms get so close that the electronic clouds of different atoms start to overlap. That kind of interactions is very well described by a delta-like interaction potential, which leads for Bose-Einstein condensates to the well established Gross-Pitaevskii equation [127]. This nonlinear Schrödinger equation describes the dynamics of Bose-Einstein condensates in the presence of short-range interactions on the Hartree-Fock level. Transport properties of such systems may be obtained by a direct solution of the nonlinear wave equation for the wave function $\psi(\vec{x})$ [128, 129]. In the case of fermionic atoms, since the system is not described by a single macroscopic wave function $\psi(\vec{x})$, it is preferable to use the Green function approach where the interaction is included in a self-consistent way, as described in Sec. 3.2.

Neutral fermionic atoms, such as ^{6}Li for instance, can nowadays be routinely confined within magnetic or optical trapping potentials and cooled down to temperatures close to the BCS transition [130]. In magnetic traps the atoms with opposite spins see a trapping potential with different sign, so that only atoms with one spin direction are trapped. In the context of the 0.7 anomaly the repulsive interaction between particles with different spin plays a crucial role, therefore optical rather than magnetic techniques for the confinement would be required in order to trap both spin species of the fermionic atoms. Optical confinement potentials are typically generated by means of counter-propagating laser beams, where standing waves emerge forming a so-called optical lattice. A quasi-two-dimensional configuration could, for instance, be realized by a rather strong one-dimensional optical lattice which creates a sequence of disk-like confinement geometries for the atoms, and a wave guide with a constriction could be induced by additional laser beams that are focused onto the disk within which the atoms are confined. According to Ref. [131], the effective interaction constant that characterizes the contact potential (3.4) would, in the case of two-dimensional ultracold fermionic atoms, be given by

$$\gamma \simeq \frac{4\pi\hbar^2}{m} \frac{1}{\sqrt{2\pi}(a_\perp/a_s) + \ln(\hbar\omega_\perp/(\pi E))}. \tag{3.44}$$

Here, m is the mass of the atom, $\omega_\perp$ denotes the frequency of the harmonic confinement in the transverse direction (perpendicular to the quasi-two-dimensional disk of atoms), $a_\perp = \sqrt{\hbar/(m\omega_\perp)}$ is the corresponding oscillator length, E denotes the total energy of the collision process in the center-of-mass frame, and a_s represents the s-wave scattering length between two atoms with different spin. Both length scales, a_s and $a_\perp$, can be manipulated via Feshbach tuning (see e.g. Ref. [132]) as well as through the intensity of the optical lattice. It would therefore be possible to realize configurations for which the effective interaction strength γ is of the order of the values that were discussed in Sec. 3.3.

To measure the atomic 0.7 anomaly, we propose to prepare the fermionic atoms in a large double-well trap sketched in Fig. 3.19 that is optically created within the two-dimensional confinement geometry. If one of the wells is energetically lowered, atoms can escape from one well to the other through a small "bottleneck" created by the central barrier, which corresponds to the constriction of Fig. 3.3. By varying

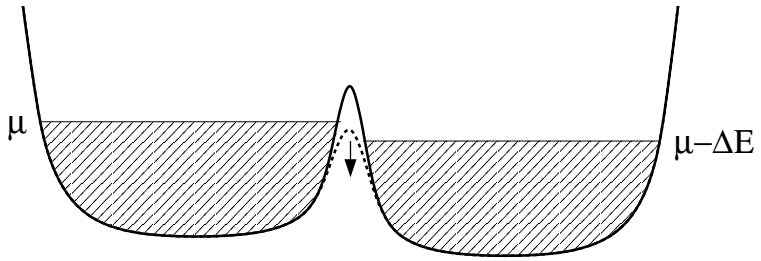

Figure 3.19: Double-well potential filled with cold atoms up to the Fermi level μ. The right well is shifted downward by ΔE and the height of the central barrier can be controlled.

the height of the central barrier different transport regimes can be realized. For high barriers the transport is blocked, and there is a crossover from a tunneling regime for barrier heights comparable to the chemical potential μ to an open regime at low barriers. This crossover regime is the interesting region for the atomic 0.7 anomaly. Counting the number of atoms that are transported across the bottleneck within a finite time scale should give rise to a current of atoms close to the Fermi level, as long as the energy shift ΔE is small. This current can be directly translated into an "atomic conductance" in a similar way as in Ref. [133], which would for noninteracting atoms also display a step-like behavior when the height of the constriction is lowered by optical techniques. Magnetic fields can again be used to break the symmetry between spin-up and spin-down fermions. An experimental challenge for such a setup is the measurement of the atomic current through the bottleneck.

As phonons are clearly absent in such a setup, any observed feature in the 0.7 anomaly that is not reproducible by mean-field approaches would necessarily be due to correlations. Therefore, transport experiments with ultracold fermionic atoms are a way to discriminate between different interpretations of the 0.7 anomaly and they can provide new insight into the central mechanism that underlies this phenomenon.

CHAPTER 4

The self-consistent potential drop

In a biased system the charges rearrange and thereby create an electrostatic potential referred to as the voltage drop between the contacts. For a rigorous description of the electrostatics of the device, the potential drop has to be determined self-consistently with the electron distribution. In this chapter we first explain the effect of an external bias on the energy spectrum of the leads and the device. We then consider the classical electrostatic problem of the biased system, which coincides with the Hartree approximation for electron-electron interactions. A recursive scheme for the self-consistent determination of the potential drop and the charge distribution based on the Newton-Raphson method is introduced. At the end of the chapter the presented procedure is applied in order to compute the electrostatic potential drop in a quantum wire.

4.1 A biased nanosystem

An interesting observable for the transport properties of a mesoscopic system is the IV-characteristics, which provides the relation between the current I and the applied voltage V. Often it is sufficient to restrict oneself to the linear regime around zero bias, where the current depends linearly on the voltage, $I = GV$. In that case the conductance G is obtained from the equilibrium properties of the considered system, which is characterized by an overall chemical potential μ. If we divide the system into device and leads, as sketched in Fig. 2.4, the states in both leads are in equilibrium occupied up to the chemical potential. As the electrons in the device are provided by the leads, also the states in the device are populated up to μ.

If a source-drain bias V is applied between the left and right contact, the energy spectra of the leads are shifted by eV with respect to each other, as sketched in Fig. 4.1. In that case the central device is differently populated by the left and right lead.

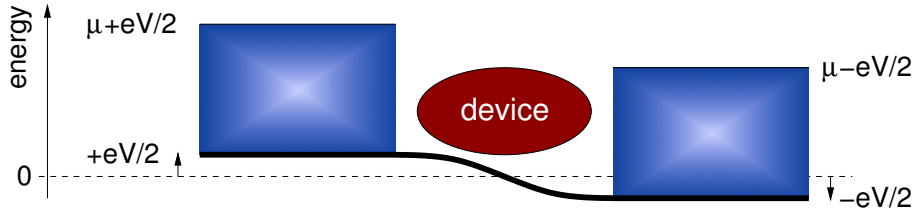

Figure 4.1: A biased mesoscopic device between two leads which are energetically shifted by $\pm eV/2$. The dashed line indicates the band bottom of the leads in equilibrium.

Therefore it is not possible to define a chemical potential inside the system. In fact, the distribution function in a nonequilibrium situation typically has a two-step shape, as shown in Fig. 2.1, rather than the shape of a Fermi function. The reason is that for energies within the bias window, that are energies between $\mu - eV/2$ and $\mu + eV/2$, the device is populated from only one of the two leads. This, in addition, implicates that in a biased system charge neutrality does not necessarily have to be maintained. Due to the shift of the energy spectrum of the contacts, the states above μ in the device are partly populated, whereas states below μ are partly depopulated. This may give rise to an excess or lack of charges in the device, if the density of states of the device is asymmetric in the vicinity of the Fermi level μ.

The band bottom of the leads has values $\pm eV/2$ far away from the device; in the device region it continuously drops from $+eV/2$ to $-eV/2$, as indicated in Fig. 4.1. This transition of the band bottom is referred to as the *potential drop*. The potential drop adjusts in a self-consistent way with the arrangement of charges in the system. For that reason it is unimportant how the energy spectrum of the leads are shifted with respect to the equilibrium situation. The voltage drop just depends on the relative difference of the band bottoms of the two leads. We choose a symmetric shift $\pm eV/2$ of both leads, so that the energy shift of the central region is minimized. There are

different heuristic model approaches to account for the potential drop, like a linear drop [134] or a step-like drop at the interfaces between contact and device [135]. A more elaborate model assumes that the potential drop is proportional to the gradient of the zero-bias potential [40], see Eq. (4.38). In the following sections we will present a possibility to consider the electrostatics of a two-dimensional system and calculate the potential drop self-consistently with the electron distribution in the device.

4.2 The electrostatic potential

The electrostatics of a classical charge distribution $\rho(\vec{x})$ is governed by the Poisson equation

$$\vec{\nabla}^2 V_{\mathrm{es}}^{\mathrm{tot}}(\vec{x}) = \frac{e}{\varepsilon\varepsilon_0}\rho(\vec{x}), \tag{4.1}$$

where $V_{\mathrm{es}}^{\mathrm{tot}}(\vec{x})$ is the electrostatic potential and ε is the material dependent dielectric constant. For a two-dimensional mesoscopic device the charge distribution consists of the electron density $n(\vec{x}) = n(x,z)\delta(y)$ and the background charge density $n_{\mathrm{BG}}(\vec{x})$,

$$\rho(\vec{x}) = -e\big[n(\vec{x}) - n_{\mathrm{BG}}(\vec{x})\big]. \tag{4.2}$$

The background charge density is in general not known a priori. On the basis of a charge neutral 2DEG one may assume a constant density of positive background charges given by

$$n_{\mathrm{2D}} = 2(\mathrm{spin}) \times \frac{m}{2\pi\hbar^2}\mu. \tag{4.3}$$

This choice, however, implicates two major problems for the simulation of quasi-one-dimensional systems: on the one hand, the charge density in the transverse direction of the device is not uniform, see Fig. 4.5. Hence, the electrostatic potential exhibits oscillations in the transverse direction and it is impossible reach a flat potential at the lead surfaces, unless we admit very large widths, which is numerically elaborate. On the other hand, the charge density in a quasi-one-dimensional system is always lower than the density of a 2DEG, as demonstrated in Fig. 4.2. The charge density in a homogeneous stripe of width W is, according to Eq. (2.112), given by

$$n_{\mathrm{1D}} = 2(\mathrm{spin}) \times \int_{-\infty}^{\mu} \mathrm{d}E\, d(E) = \frac{2}{\pi\hbar W}\sum_k \sqrt{2m(\mu - E_k)}. \tag{4.4}$$

Due to this mismatch, even in the multi-channel limit, there is always an excess of positive charges in the device. This leads to an attractive potential in the device accompanied by unphysical effects for the electrostatic potential at the boundaries of the simulated area.

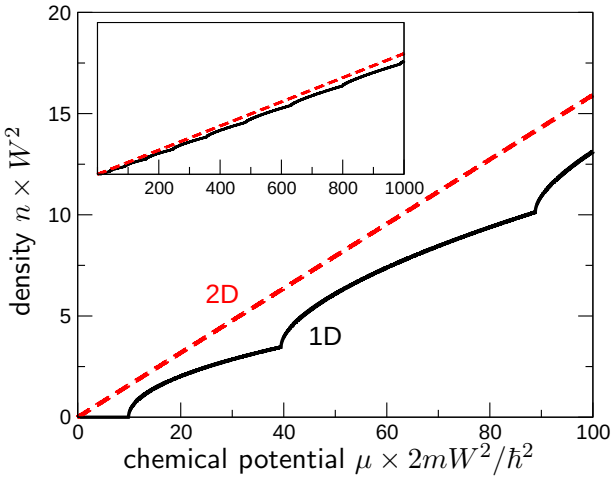

Figure 4.2: The 1D (black solid line) and 2D (red dashed line) electron density in units of W^{-2} as a function of the chemical potential μ. The inset shows the graphs for a wider range of μ.

Instead of making an explicit choice for the background charge density, we shall include the electrostatic potential due the equilibrium charge distribution of both the electrons and the ions in the confinement potential $U(\vec{x})$. This is the standard argument used for equilibrium quantum transport, which legitimates the choice of a hard-wall confinement potential [36]. The electrostatics in an unbiased system is then described by the Poisson equation

$$\vec{\nabla}^2 V_{\rm es}^0(\vec{x}) = -\frac{e^2}{\varepsilon\varepsilon_0}\big[n_0(\vec{x}) - n_{\rm BG}(\vec{x})\big], \tag{4.5}$$

where $n_0(\vec{x})$ is the equilibrium charge density. The sum of the resulting potential $V_{\rm es}^0(\vec{x})$ and the top-gate potentials defining the geometry represents the effective confinement potential $U(\vec{x})$. The latter will be modelled by a hard-wall potential and therefore $V_{\rm es}^0(\vec{x})$ does not have to be considered explicitly. If a finite external bias is applied, the charges in the system rearrange. Let $\delta n(\vec{x}) = n(\vec{x}) - n_0(\vec{x})$ denote the charge rearrangement, then the Poisson equation for the nonequilibrium case reads

$$\vec{\nabla}^2 V_{\rm es}^{\rm tot}(\vec{x}) = -\frac{e^2}{\varepsilon\varepsilon_0}\big[\delta n(\vec{x}) + n_0(\vec{x}) - n_{\rm BG}(\vec{x})\big] = \vec{\nabla}^2\big[V_{\rm es}^0(\vec{x}) + V_{\rm es}(\vec{x})\big], \tag{4.6}$$

where the effective electrostatic potential defined as

$$V_{\rm es}(\vec{x}) = V_{\rm es}^{\rm tot}(\vec{x}) - V_{\rm es}^0(\vec{x}) \tag{4.7}$$

represents the change of the potential with respect to the equilibrium situation. In the Poisson equation (4.6) for the biased system the equilibrium part, Eq. (4.5), cancels and we end up with a Poisson equation for the effective potential

$$\vec{\nabla}^2 V_{\rm es}(\vec{x}) = -\frac{e^2}{\varepsilon\varepsilon_0}\big[n(\vec{x}) - n_0(\vec{x})\big], \tag{4.8}$$

which does not explicitly depend on the background density $n_{\mathrm{BG}}(\vec{x})$. The potential drop is then given by the effective electrostatic potential $V_{\mathrm{es}}(\vec{x})$ due to the charge rearrangement $n(\vec{x}) - n_0(\vec{x})$, similar as in Refs. [31, 136].

Let us first consider a situation with a definite boundary between device and leads, like for instance a molecular wire between bulk metal electrodes [137–140]. For such a geometry the electrodes can be regarded as equipotentials and the boundary conditions for $V_{\mathrm{es}}(\vec{x})$ are well defined. It is convenient to write the total effective electrostatic potential as a sum of two contributions

$$V_{\mathrm{es}}(\vec{x}) = V_{\mathrm{bias}}(\vec{x}) + V_e(\vec{x}), \tag{4.9}$$

where $V_{\mathrm{bias}}(\vec{x})$ is the potential in the absence of any charges between the electrodes. It obeys the Laplace equation, which is obtained from the Poisson equation (4.1) by substituting $\rho(\vec{x}) \equiv 0$,

$$\vec{\nabla}^2 V_{\mathrm{bias}}(\vec{x}) = 0, \tag{4.10}$$

with boundary conditions $V_{\mathrm{bias}}(x = 0) = eV/2$ and $V_{\mathrm{bias}}(x = L) = -eV/2$. Here, L is the distance between the electrodes and V denotes the applied voltage. In the case of three-dimensional contacts, V_{bias} has the shape of linear ramp between the contact surfaces,

$$V_{\mathrm{bias}}(x) = \frac{eV}{2} - eV\frac{x}{L}. \tag{4.11}$$

The potential $V_e(\vec{x})$ is created by the charges in the device, thus it is the solution of the Poisson equation

$$\vec{\nabla}^2 V_e(\vec{x}) = -\frac{e^2}{\varepsilon\varepsilon_0}\big[n(\vec{x}) - n_0(\vec{x})\big], \tag{4.12}$$

with zero boundary conditions at the interfaces of the contacts. Hence, the total effective electrostatic potential $V_{\mathrm{es}}(\vec{x})$ respects both the charges in the device and the influence of the contacts, and it is a continuous function at the lead surfaces.

However, in many situations there is no strict border between leads and device, like in a quantum point contact depicted in Fig. 3.1. There the "device" is the narrow constriction and the leads can be regarded as the 2DEG connecting the metallic contacts with the constriction. The electron density in the leads usually is larger than the density in the device, giving rise to a screening of the electrostatic potential induced by the contacts. Therefore the potential in the leads is expected to become flat far away from the device. Typically, a part of the leads is included into the so-called *extended device*, which has to be large enough to get a constant electrostatic potential close to the interface of the leads. A further explanation is given with the example of the quantum wire in Sec. 4.4.

The electrostatic potential V_e due to the charges in the device can be obtained by the solution of the Poisson equation (4.12). If the considered system was isotropic in

the y-direction, the particle density would not depend on y and the Poisson equation would be reduced to a two-dimensional equation in the (x, z)-plane. Then it could be numerically solved on the grid of the 2DEG. In our case the particle density is non-uniform along the direction perpendicular to the 2DEG, $n(\vec{x}) = n(x, z)\delta(y)$, which requires a full three-dimensional treatment of the Poisson equation. This is numerically extremely demanding. Therefore we use the known solution of the Poisson equation for the boundary conditions of a vanishing potential at infinity

$$V_e(\vec{x}) = \frac{e^2}{4\pi\varepsilon\varepsilon_0} \int \mathrm{d}^3x' \, \frac{n(\vec{x}') - n_0(\vec{x}')}{|\vec{x} - \vec{x}'|}. \tag{4.13}$$

This precisely corresponds to the Hartree self-energy for the Coulomb potential, see Eq. (A.11). The solution keeps its form, if we insert the delta function in the y-component for both $n(\vec{x})$ and $n_0(\vec{x})$, and perform the y-integration,

$$V_e(\vec{r}) = \frac{e^2}{4\pi\varepsilon\varepsilon_0} \int \mathrm{d}^2r' \, \frac{n(\vec{r}') - n_0(\vec{r}')}{|\vec{r} - \vec{r}'|}, \tag{4.14}$$

where again $\vec{r}$ denotes a vector within the plane of the 2DEG. The dimensionless electrostatic potential for the discretized spatial coordinates is obtained by replacing the integral by a sum

$$\widetilde{V}_e(\tilde{\vec{r}}_j) = \frac{2ma^2}{\hbar^2} \frac{e^2}{4\pi\varepsilon\varepsilon_0} \left(\sum_{i \neq j} \frac{\tilde{n}(\tilde{\vec{r}}_i) - \tilde{n}_0(\tilde{\vec{r}}_i)}{a|\tilde{\vec{r}}_i - \tilde{\vec{r}}_j|} + \frac{1}{a^2} \int\limits_{\text{site } j} \mathrm{d}^2r \, \frac{\tilde{n}(\tilde{\vec{r}}_j) - \tilde{n}_0(\tilde{\vec{r}}_j)}{|\vec{r} - \vec{r}_j|} \right), \tag{4.15}$$

where the second term separately accounts for the divergent short-range contribution of the potential. The remaining integral can be calculated to yield [136]

$$C = \frac{1}{a} \int\limits_{-a/2}^{a/2} \int\limits_{-a/2}^{a/2} \frac{\mathrm{d}x \, \mathrm{d}y}{\sqrt{x^2 + y^2}} = \frac{4}{a} \int\limits_{-\pi/4}^{\pi/4} \mathrm{d}\theta \int\limits_{0}^{a/(2\cos\theta)} \mathrm{d}r \; r \frac{1}{r} = 2 \ln \frac{\sqrt{2} + 1}{\sqrt{2} - 1} \approx 3.525. \tag{4.16}$$

So the final expression for the dimensionless electrostatic potential, including the contribution from the contacts, Eq. (4.11), reads

$$\widetilde{V}_{\text{es}}(\tilde{\vec{r}}_j) = \widetilde{V}_{\text{bias}}(\tilde{\vec{r}}_j) + \gamma_C \left(\sum_{i \neq j} \frac{\tilde{n}(\tilde{\vec{r}}_i) - \tilde{n}_0(\tilde{\vec{r}}_i)}{|\tilde{\vec{r}}_i - \tilde{\vec{r}}_j|} + C\big[\tilde{n}(\tilde{\vec{r}}_j) - \tilde{n}_0(\tilde{\vec{r}}_j)\big] \right), \tag{4.17}$$

where the interaction strength

$$\gamma_C = \frac{2ma}{\hbar^2} \frac{e^2}{4\pi\varepsilon\varepsilon_0} \tag{4.18}$$

scales linearly with the lattice constant a.

In conclusion, the electrostatic potential drop consists of two parts: a linear contribution $V_{\text{bias}}(\vec{r})$ due to the contacts, Eq. (4.11), and a contribution $V_e(\vec{r})$ due to the charge redistribution in the device. The second part depends on the difference of the nonequilibrium and the equilibrium electron density, according to Eq. (4.14). It is expected that the rearrangement of charges in the leads, where the density is high, is marginal, such that the total electrostatic potential $V_{\text{es}}(\vec{r})$ becomes flat in the leads. This defines a natural cutoff for the length of the extended device.

4.3 The self-consistent calculation scheme

The full Hamiltonian of a two-dimensional system in the presence of an in-plane magnetic field $B(\vec{r})$ and including the electrostatic potential $V_{\text{es}}(\vec{r})$ reads

$$\mathcal{H}^\sigma = -\frac{\hbar^2}{2m}\vec{\nabla}^2 + U(\vec{r}) + V_{\text{es}}(\vec{r}) + g\mu_B B(\vec{r})\sigma. \tag{4.19}$$

According to Eq. (2.95), the retarded Green function is obtained by matrix inversion

$$\mathcal{G}^r_\sigma(E) = \left[E - \mathcal{H}^\sigma - \Sigma_L(E - eV/2) - \Sigma_R(E + eV/2)\right]^{-1}, \tag{4.20}$$

where the arguments of lead self-energies are shifted by $\pm eV/2$ due to the applied voltage. Because the electron-electron interaction enters through a local potential $V_{\text{es}}(\vec{r})$, the recursive algorithm described in Appendix C can be employed to evaluate $\mathcal{G}^r(E)$. Knowing the retarded Green function, the lesser Green function can be computed by means of the kinetic equation (2.101), which then gives the particle density using Eq. (2.116). The particle density determines the electrostatic potential, according to Eq. (4.17), which in turn enters the retarded Green function. Therefore, the equations for the Green function, Eq. (4.20), and the electrostatic potential, Eq. (4.17), have to be solved self-consistently. Similar to the procedure sketched in Fig. 3.4, we start with an initial guess for $V_{\text{es}}(\vec{r})$ and iterate between the computation of the retarded Green function and the electrostatic potential, in order to achieve a self-consistent solution. However, the system of Poisson equation and Green function is highly nonlinear and it is known, that a simple alternating solution of the two relevant equations does typically not converge [141]. Because the system of equations is very sensitive to small changes, one important condition is to know the electron density with high accuracy. Since in the following chapter we aim to calculate transport properties of quantum dot like geometries with a peaked density of states, it is inevitable to use the complex contour integration described in Sec. 2.5.2 to determine the electron density in the system.

In order to improve the convergence properties, one possibility is the method of underrelaxation, which includes a fraction Ω of the electrostatic potential of the previous iteration step,

$$V^{(N)}_{\text{es}}(\vec{r}) = V^{(N)}_{\text{es}}(\vec{r}) + \Omega\left[V^{(N-1)}_{\text{es}}(\vec{r}) - V^{(N)}_{\text{es}}(\vec{r})\right]. \tag{4.21}$$

Here, N labels the number of the self-consistency step. The damping factor Ω has to be chosen close to unity in order to reach convergence. This means that a lot of iterations are necessary which is connected with an enormous consumption of computing time.

An alternative, which has proven to be much more efficient than the method of underrelaxation, is the Newton-Raphson method [58, 141]. This procedure in general provides an iterative scheme to find the root of a nonlinear function $f(x)$, involving the first order Taylor expansion of the function. Starting with a given value $x^{(N)}$ for the approximate root, one gets the next value $x^{(N+1)}$ by the so-called Newton-Raphson equation [63]

$$x^{(N+1)} = x^{(N)} - \frac{f(x^{(N)})}{f'(x^{(N)})}. \tag{4.22}$$

This can easily be generalized to multi-dimensional functions $\vec{f}(\vec{x})$, where the system of linear equations

$$\sum_k \left.\frac{\partial f_j}{\partial x_k}\right|_{\vec{x}^{(N)}} \Delta x_k^{(N)} = -f_j(\vec{x}^{(N)}) \tag{4.23}$$

has to be solved for the vector $\Delta\vec{x}^{(N)}$. This defines the new value $\vec{x}^{(N+1)}$ of the root by

$$\vec{x}^{(N+1)} = \vec{x}^{(N)} + \Delta\vec{x}^{(N)}. \tag{4.24}$$

In Refs. [58, 141] the Newton-Raphson method is used to numerically solve the Poisson equation on a grid. We shall adapt this method to the evaluation of the electrostatic potential by means of Eq. (4.17), which we rewrite to

$$F_j = \widetilde{V}_{\mathrm{es},j} - \widetilde{V}_{\mathrm{bias},j} - \sum_i \varphi_{i,j}\left[\tilde{n}_i - \tilde{n}_{0,i}\right] = 0, \tag{4.25}$$

with

$$\varphi_{i,j} = \begin{cases} \gamma_C/|\tilde{\vec{r}}_i - \tilde{\vec{r}}_j| & \text{for } i \neq j \\ C\gamma_C & \text{for } i = j. \end{cases} \tag{4.26}$$

In order to solve the above equation (4.25), we use the Newton-Raphson equation (4.23) to get

$$\sum_k \frac{\partial F_j}{\partial \widetilde{V}_{\mathrm{es},k}} \Delta\widetilde{V}_{\mathrm{es},k} = -F_j. \tag{4.27}$$

Since $\tilde{n}_0$ and $\widetilde{V}_{\mathrm{bias}}$ do not depend on the electrostatic potential, the derivative yields

$$\frac{\partial F_j}{\partial \widetilde{V}_{\mathrm{es},k}} = \delta_{j,k} - \sum_i \varphi_{i,j} \frac{\partial \tilde{n}_i}{\partial \widetilde{V}_{\mathrm{es},k}}. \tag{4.28}$$

The Jacobian $\partial\tilde{n}_i/\partial\widetilde{V}_{\mathrm{es},k}$ we evaluate using a Thomas-Fermi approximation, similar as in Refs. [58, 141]. For that reason we approximate the system locally by a homogeneous wire with width $W(x)$ and with a shifted energy spectrum $E + u^\sigma(\vec{r})$, where $u^\sigma(\vec{r}) = V_{\mathrm{es}}(\vec{r}) + U(\vec{r}) + g\mu_B B(\vec{r})\sigma$ contains all relevant potentials. The Thomas-Fermi particle density then yields

$$n^\sigma_{\mathrm{TF}}(\vec{r}) = \int \mathrm{d}E\, d(\vec{r}, E) f(E, \mu^\sigma(\vec{r}) - u^\sigma(\vec{r})). \tag{4.29}$$

Inserting the explicit form of the density of states, Eq. (2.111), and using $f(E,\mu) = \Theta(\mu - E)$ for $T = 0$, we obtain

$$n^\sigma_{\mathrm{TF}}(\vec{r}) = \frac{2}{\pi\hbar W(x)} \sum_l \sin^2\left(\frac{l\pi z}{W(x)}\right) \sqrt{2m\big(\mu^\sigma(\vec{r}) - u^\sigma(\vec{r}) - E_l\big)}. \tag{4.30}$$

The local chemical potential $\mu^\sigma(\vec{r})$ is an auxiliary quantity which is obtained from the above relation after inserting the potential $u^\sigma(\vec{r})$ and equating the Thomas-Fermi density with the actual particle density in the system. Rewriting Eq. (4.30) in dimensionless form, we find

$$\tilde{n}^\sigma_i = \frac{2}{\pi\widetilde{W}} \sum_l \sin^2\left(\frac{l\pi\tilde{z}_i}{\widetilde{W}}\right) \sqrt{\tilde{\mu}^\sigma_i - \widetilde{V}_{\mathrm{es},i} - \tilde{u}^\sigma_{0,i} - \frac{\pi^2 l^2}{\widetilde{W}^2}}, \tag{4.31}$$

with $u_0(\vec{r}) = U(\vec{r}) + g\mu_B B(\vec{r})\sigma$. The Jacobian in Eq. (4.28) which is necessary for the Newton-Raphson method follows to be

$$\frac{\partial\tilde{n}^\sigma_i}{\partial\widetilde{V}_{\mathrm{es},k}} = -\frac{\delta_{i,k}}{\pi\widetilde{W}} \sum_l \sin^2\left(\frac{l\pi\tilde{z}_i}{\widetilde{W}}\right) \left[\tilde{\mu}^\sigma_i - \widetilde{V}_{\mathrm{es},i} - \tilde{u}^\sigma_{0,i} - \frac{\pi^2 l^2}{\widetilde{W}^2}\right]^{-1/2}. \tag{4.32}$$

One iteration step of the self-consistency procedure to get from an electrostatic potential $\widetilde{V}^{(N)}_{\mathrm{es}}(\vec{r})$ to the next value $\widetilde{V}^{(N+1)}_{\mathrm{es}}(\vec{r})$ consists of several substeps:

① from a given electrostatic potential $\widetilde{V}^{(N)}_{\mathrm{es}}(\vec{r})$ we calculate the retarded Green function by means of Eq. (4.20);

② using the kinetic equation (2.101), we obtain the lesser Green function, which allows us to compute the particle density from Eq. (2.116);

③ inserting both the potential $\widetilde{V}^{(N)}_{\mathrm{es}}(\vec{r})$ and the particle density $\tilde{n}^\sigma(\vec{r})$ into Eq. (4.31) we can extract the local chemical potential $\tilde{\mu}^\sigma(\vec{r})$ on the basis of the Thomas-Fermi approximation;

④ using $\widetilde{V}^{(N)}_{\mathrm{es}}(\vec{r})$ and $\tilde{\mu}^\sigma(\vec{r})$ we obtain the Jacobian $\partial\tilde{n}_j/\partial\widetilde{V}_{\mathrm{es},k}$, which is needed for the Newton-Raphson equation;

⑤ the Jacobian enters the Newton-Raphson equation (4.27) which takes the form

$$\sum_k \left[\delta_{j,k} - \varphi_{j,k} \frac{\partial \tilde{n}_k}{\partial \widetilde{V}_{\mathrm{es},k}} \right] \Delta \widetilde{V}_{\mathrm{es},k} = -F_j. \tag{4.33}$$

This system of linear equations is solved for $\Delta \widetilde{V}_{\mathrm{es},k}$;

⑥ the new value of the electrostatic potential is obtained from the previous one by

$$\widetilde{V}_{\mathrm{es}}^{(N+1)}(\vec{r}) = \widetilde{V}_{\mathrm{es}}^{(N)}(\vec{r}) + \Delta \widetilde{V}_{\mathrm{es}}(\vec{r}). \tag{4.34}$$

This procedure has to be iterated until the results for the electrostatic potential are converged. The convergence criterion is fulfilled if the square of the maximum relative deviation of the electrostatic potential with respect to the previous step is smaller than 10^{-5},

$$\max_{\vec{r}} \left(\frac{\widetilde{V}_{\mathrm{es}}^{(N)}(\vec{r}) - \widetilde{V}_{\mathrm{es}}^{(N-1)}(\vec{r})}{\widetilde{V}_{\mathrm{es}}^{(N)}(\vec{r})} \right)^2 < 10^{-5}. \tag{4.35}$$

This method significantly improves the convergence properties of the self-consistent computation of transport and electrostatic properties of two-dimensional systems. Although the Newton-Raphson scheme requires the additional computation of a local chemical potential and the solution of a linear system of coupled equations (4.33), it gives rise to an overall speed-up of the numerical routine.

4.4 Example: potential drop in a quantum wire

In this section we apply the previously defined method in order to compute the potential drop in a quantum wire. A standard way to define a quantum wire is the use of split-gates on top of the 2DEG, which are negatively biased with a voltage V_G. The electrostatic potential created by two infinitely long electrodes with a spacing w is given by

$$V_{\mathrm{es}}^G(z) = eV_G - \frac{eV_G}{\pi} \left(\arctan \frac{w/2 + z}{d} + \arctan \frac{w/2 - z}{d} \right), \tag{4.36}$$

where the 2DEG is located at a depth d underneath the gates [142]. Fig. 4.3 shows the gate potential for $w = 0.5\,\mu$m and $d = 0.1\,\mu$m. We see that in addition to the transverse confinement in z-direction there is an energy offset U_0 with respect to the case of zero gate voltage.

We model the quantum wire by a hard-wall confinement potential $U(\vec{r})$ with varying width along the direction of transport, as sketched in Fig. 4.4. The simulated system consists of 5 different parts: in the center there is the actual narrow wire with a width

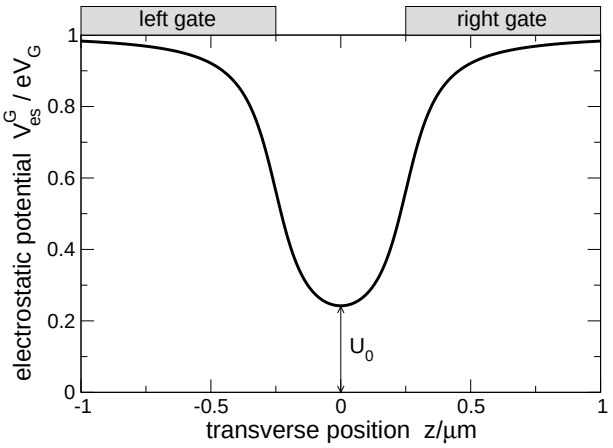

Figure 4.3: Split-gate potential according to Eq. (4.36) for an electrode spacing $w = 0.5\,\mu$m and a distance $d = 0.1\,\mu$m between the 2DEG and the gates.

$W = 0.25\,\mu$m and a length $L_{\text{wire}} = 1\,\mu$m. At both ends of the wire the system widens to $3W$ over a length of $L_c = 0.5\,\mu$m according to the previously defined switching function $s_L(x)$, Eq. (3.13). There the system is attached to the semi-infinite leads with width $3W$, where a fraction of length L_{inter} is included into the extended device. In order to consider the potential offset U_0 indicated in Fig. 4.3, the confinement potential is assumed to have a finite value $U_0 = 0.17\,$meV inside the wire, which is adiabatically switched off at the transition to the wide leads according to Eq. (3.13). The confinement potential is also sketched in Fig. 4.4. The chosen chemical potential is $\mu = 0.30\,$meV,

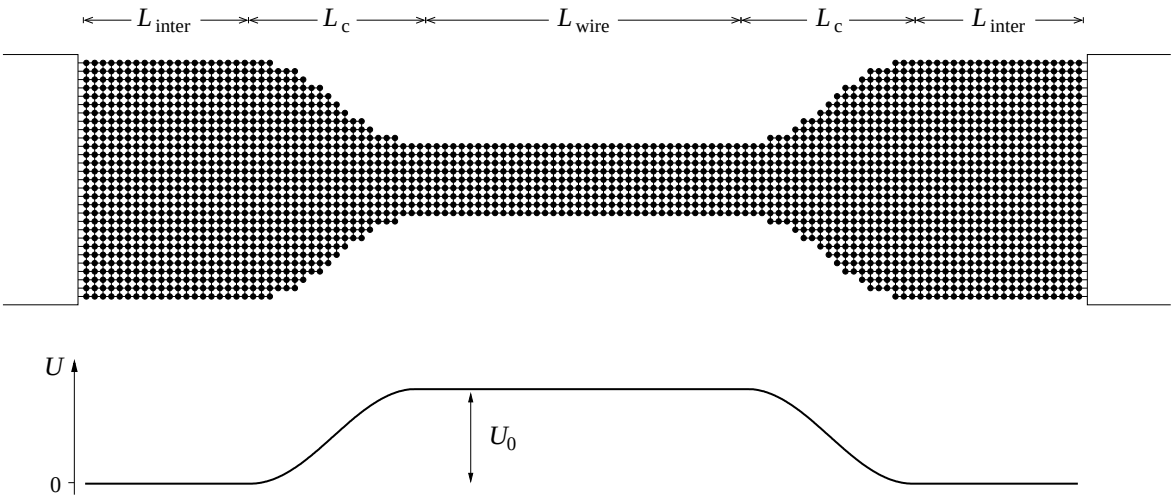

Figure 4.4: Geometry of the quantum wire in discrete representation. The graph below shows the variation of the confinement potential U along the wire.

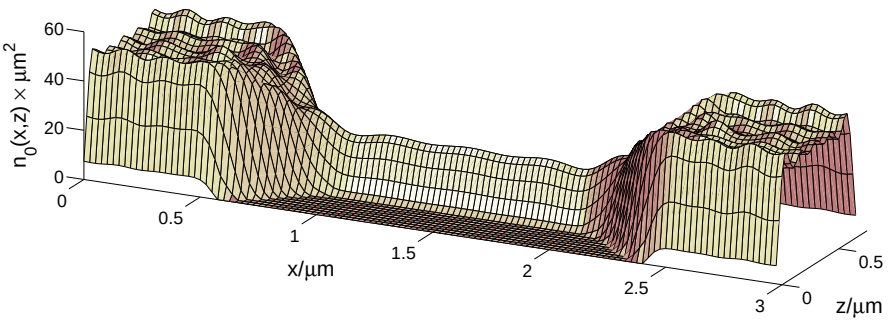

Figure 4.5: The equilibrium electron density of the quantum wire for a chemical potential $\mu = 0.30\,\mathrm{meV}$.

so that one transverse channel in the wire and 5 channels in the leads are open. The equilibrium electron density $n_0(\vec{r})$ for $V = 0$ is displayed in Fig. 4.5. It shows small Friedel oscillations along the wire and moreover the density is considerably higher in the leads than in the wire.

In order to investigate the influence of L_{inter} on the results, we calculate the potential drop $V_{\mathrm{es}}(\vec{r})$ for different values of L_{inter}. Fig. 4.6 shows a plot of the electrostatic potential $\overline{V}_{\mathrm{es}}(x)$, where the bar refers to an average over the transverse coordinate,

$$\overline{V}_{\mathrm{es}}(x) = \int \frac{\mathrm{d}z}{W(x)} V_{\mathrm{es}}(x,z). \tag{4.37}$$

Although the bias potential $V_{\mathrm{bias}}(x)$, that drops linearly over the entire length of the system, see Eq. (4.11), is different for the three cases, the resulting potentials $\overline{V}_{\mathrm{es}}(x)$

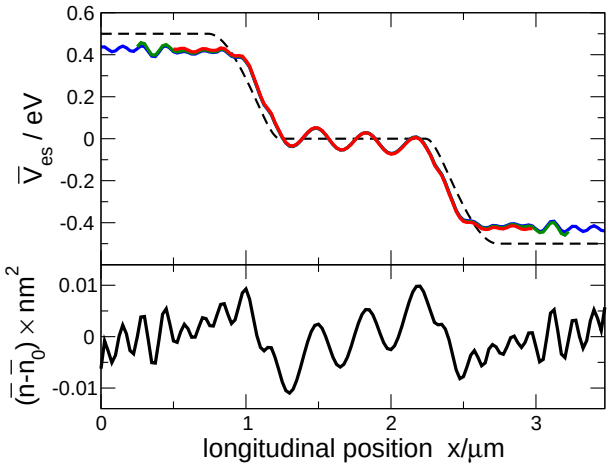

Figure 4.6: Upper panel: potential drop for $V = 0.0087\,\mathrm{mV}$ and different lengths $L_{\mathrm{inter}} = 0.25\,\mu\mathrm{m}$ (red), $0.5\,\mu\mathrm{m}$ (green), and $0.75\,\mu\mathrm{m}$ (blue). The dashed line is the potential drop according to Linke's model, Eq. (4.38). Lower panel: charge redistribution in the system.

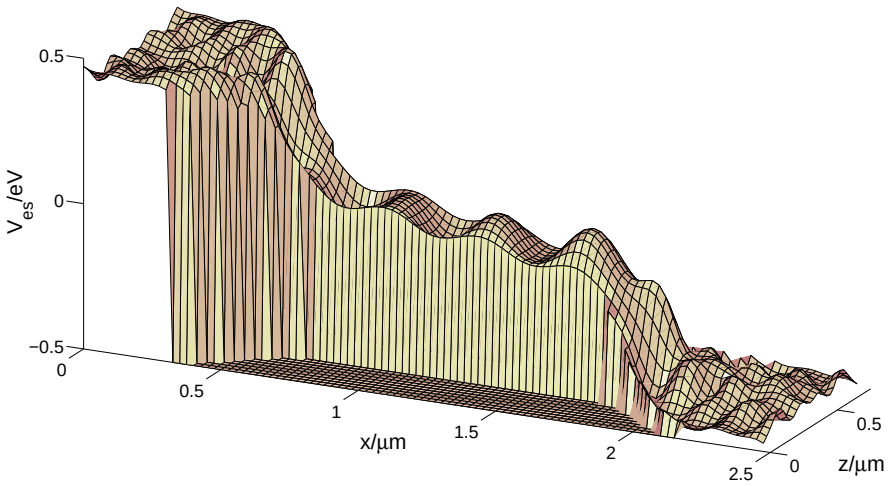

Figure 4.7: The full electrostatic potential for $V = 0.0087\,\mathrm{mV}$ and $L_{\mathrm{inter}} = 0.25\,\mu\mathrm{m}$, corresponding to the red curve in Fig. 4.6.

agree very well. Therefore, including about $0.25\,\mu$m of the leads into the extended device is sufficient to obtain a robust result for that system; a further enlargement of the extended device does not bring along any significant changes in the electrostatic potential.

The results demonstrate that the potential drop is efficiently screened inside the leads due to the high particle density. The screening is induced by a charge accumulation at the narrowing part of the system as shown in the lower panel of Fig. 4.6. The electrons pile up or deplete at the interfaces between the wide leads and the narrow quantum wire. This causes a flat potential in the leads already after a few tens of nanometers. We shall note that the potential saturates at a value with a modulus slightly smaller than $eV/2$, and moreover it is not constant along the transverse direction, as seen in the 3D-plot in Fig. 4.7. Therefore, the transition between lead and system is not precisely continuous, but the magnitude of the discontinuity at the interface is small compared to the applied voltage. In the results for the ratchet systems in the following chapter the mismatch at the leads is even smaller. The curves in Fig. 4.6 indicate that the potential predominantly drops at the narrowing part of the device. Within the quantum wire the charges redistribute to generate a lack of electrons at the left end and an excess of electrons at the right end. Therefore the potential inside the wire appears to be flat, apart from Friedel oscillations reflecting the oscillations in the density, see Fig. 4.5. These findings are in line with other results on narrow wires [137, 139, 143–145] or atomic chains [138, 140, 144] in the presence of large source-drain voltages.

The observed behavior, that the potential primarily drops where the confinement varies, can be explained by scattering. If the confinement potential is flat, there is no source of backscattering, so that the electrons can rearrange in order to screen the potential drop. This is not the case in the presence of a gradient of the confinement,

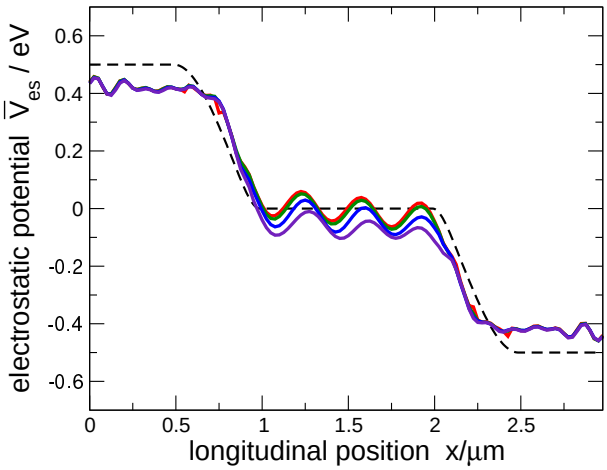

Figure 4.8: Potential drop normalized to the applied voltage eV, for $V = 0.0017\,\mathrm{mV}$ (red), $0.0087\,\mathrm{mV}$ (green), $0.026\,\mathrm{mV}$ (blue), and $0.052\,\mathrm{mV}$ (violet). The dashed line shows the potential drop according to Linke's model, Eq. (4.38)

either through an onsite potential as sketched in Fig. 4.4 or through changes of the width[1]. This observation was used by Linke *et al.* to formulate a model [40], where they assumed that the potential drop is proportional to the gradient of the confinement potential $U(x)$

$$V_{\mathrm{es}}^{\mathrm{Linke}}(x) = eV\left(\frac{1}{2} - \frac{\int_0^x \mathrm{d}x' \left|\frac{\partial}{\partial x'}U(x')\right|}{\int_0^L \mathrm{d}x' \left|\frac{\partial}{\partial x'}U(x')\right|}\right). \tag{4.38}$$

Here, L denotes the length of the system. In the presence of magnetic fields the Zeeman potential can also be included in the above formula [44]. The resulting potential drop is displayed by the dashed line in Figs. 4.6 and 4.8, and it appears to coincide very well with the overall behavior obtained by the self-consistent calculations.

Another interesting issue is the scaling behavior of the potential drop for different voltages V. The curves in Fig. 4.8 show the electrostatic potential V_{es} for different values of the applied voltage, where the smallest and largest voltage differ by a factor of 30. We see that in the whole range the voltage drop scales almost linearly with the voltage V. In the central part of the wire a downward trend of the potential can be observed with increasing voltage.

The approach to determine the electrostatic potential drop self-consistently with the electron distribution in the system, which is described within this chapter, works well for a quantum wire. The numerical procedure converges steadily for a reasonable

[1] In a system with non-uniform width the effective energy of the first transverse subband, Eq. (3.17), is approximately modified according to $E_1(x) = \hbar^2\pi^2/(2mW^2(x))$, which corresponds to the presence of a potential barrier.

parameter range, however for high voltages $eV > 0.07\,\mathrm{meV}$ no convergence could be achieved. The obtained results show that the major part of the potential drops at the interfaces between the leads and the narrow wire, where the confinement potential has a nonvanishing gradient. This behavior can qualitatively be explained by the enhanced backscattering at regions, where the geometry of the system changes. The results of Linke's model based on that idea coincides very well with the course structure of the potential drop obtained self-consistently within our approach.

CHAPTER 5

Quantum ratchet systems

The subject of this chapter is the investigation of ballistic ratchet systems based on mesoscopic electronic devices that can rectify an unbiased external AC driving. After a short introduction into the generalities of ratchets we consider two different devices: a charge ratchet based on a triangular quantum dot and a double-dot structure acting as a spin ratchet. In both situations we compute the net charge or spin current, respectively, averaged over one period of the driving. The current is calculated after the self-consistent determination of the electrostatic potential in the presence of an external voltage. For the charge ratchet we obtain a finite net current, where the sign and the magnitude depends strongly on the chemical potential and the driving amplitude. The spin ratchet produces a finite net spin current, whereas the charge current vanishes. The sign and magnitude of the spin current can be controlled by the rocking amplitude.

5.1 Directed transport in asymmetric potentials

Systems that can extract useable work like a directed current out of fluctuating forces are referred to as *Brownian motors* or *ratchets* [146–148]. The forces acting on the system can be of different origin, like thermal noise or external driving, however their average has to vanish. One important condition for the appearance of a ratchet effect is a broken spatial inversion symmetry along the direction of transport. This is typically realized by an asymmetric potential $U(x)$, the so-called ratchet potential. A classical particle with mass m in the presence of thermal noise $\xi(t)$ is described by Newton's equation

$$m\ddot{x}(t) = -U'(x(t)) - \eta\dot{x}(t) + \xi(t). \tag{5.1}$$

The force acting on the particle consists of the static force due to the gradient of the ratchet potential $U(x)$, a viscous friction with friction coefficient η and a fluctuating force $\xi(t)$ due to the thermal noise. As the latter two contributions both originate from the interactions with a huge thermal environment, they are not independent. The fluctuations $\xi(t)$ are typically modelled by a Gaussian white noise [146] with zero mean

$$\langle \xi(t) \rangle = 0, \tag{5.2}$$

which is connected with the friction constant through the dissipation-fluctuation relation

$$\langle \xi(t)\xi(t') \rangle = 2\eta k_B T \delta(t - t'). \tag{5.3}$$

The noise therefore is uncorrelated in time.

The presence of an asymmetric potential, however, is not sufficient in order to observe a ratchet effect, i.e. directed motion generated by fluctuating forces. This was pointed out in a *Gedankenexperiment* by Smoluchowski and Feynman [149] who considered a ratchet and pawl device as depicted in Fig. 5.1 surrounded by a gas at temperature T. Due to the Brownian motion of the gas molecules, they randomly hit the paddles of the device. In absence of the pawl the axis performs unbiased random rotations caused by the impact of the gas molecules on the paddles. Because of the asymmetric shape of the gear wheel, which plays the role of the ratchet potential $U(x)$ in Eq. (5.1), the device has a (classically) preferred direction of motion in the presence of the pawl. Therefore, it might seem convincing at first glance, that such a device can operate as a rectifier of motion.

However, if the device is scaled down to microscopic size, all energies are rescaled as well. Then also the pawl and the spring exhibit thermal fluctuations and a thorough analysis [149] shows, that the preferred "forward" motion imposed by the asymmetric gear wheel is exactly compensated by a favored "backward" motion due to thermal fluctuations of the pawl. This results in a zero net rotation of the device. Therefore

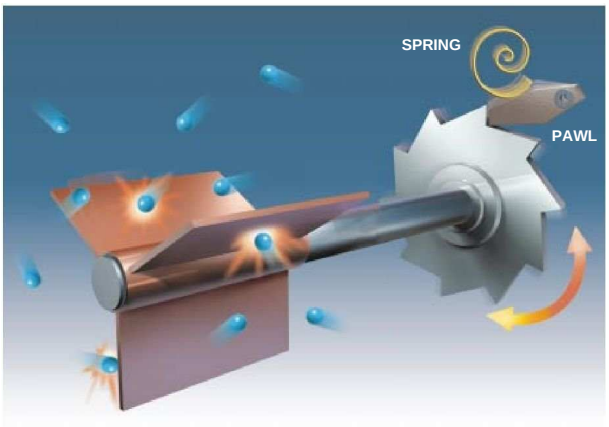

Figure 5.1: Ratchet and pawl device: gas molecules randomly hit the paddle and the pawl is supposed to rectify the motion. Picture taken from [150].

the considered system respects the second law of thermodynamics which states that no work can be extracted from a system in thermal equilibrium.

As a consequence, in addition to the presence of an asymmetric potential, the system has to be driven out of thermal equilibrium in order to observe a ratchet effect. This can, for instance, be achieved by a temperature gradient in the system, where the paddles and the pawl are kept in an environment with different temperatures [149]. Furthermore, an external driving can force the system out of equilibrium, where one distinguishes two fundamental types of driving: On the one hand, ratchets with a time-periodically varying potential $U(x, f(t))$ are called *pulsating ratchets*. A possible realization are so-called on-off ratchets, where the ratchet potential is periodically switched on and off, giving rise to a net current of particles in one direction. On the other hand, systems with a static potential $U(x)$ and an additional periodic or stochastic driving force are called *tilting ratchets*; in the case of a periodic driving they are named *rocking ratchets*. Such a driving can be realized by applying an AC voltage to an electrical device. In all possible realizations of a ratchet a finite net current can be obtained for a vanishing average driving. The sign of the net current crucially depends on the external parameters like the temperature and the driving amplitude or frequency in a non-trivial way. The direction of the net current can change as a function of those parameters, which is known as *current inversion*.

Whereas the above presented model in Eq. (5.1) is purely classical, the original idea of ratchets can be extended to the realm of quantum ratchets [151]. Both the fluctuating force and the dissipation are then introduced by the coupling to a heat bath, which is typically modelled by an ensemble of harmonic oscillators.

Besides the original definition of ratchets, where Brownian motion plays the dominant role, also ballistic systems rectifying unbiased AC driving are named ratchets or rectifiers. In such systems the dissipation exclusively takes place inside the contacts, and the electron dynamics in the device is ballistic. Electronic ratchets have been realized by periodic structures [40] and single quantum dots [38, 39, 152], where a rectifying behavior was observed. Recently, also *spin ratchets* were proposed [41–46], which can generate a directed spin current, while the net charge current vanishes,

if certain symmetries are preserved. Concerning the spin ratchets also the effect of dissipation is analyzed [153].

In this chapter we will consider ballistic non-periodic mesoscopic ratchet devices built on two-dimensional electron gases (2DEGs). In Sec. 5.3 we investigate the coherent transport properties of a triangular quantum dot, similar to the one used in experiments [38, 39], exposed to a periodic driving beyond the linear response regime. Our results show a ratchet effect and we find current inversions by changing the amplitude of the driving or the chemical potential. In the subsequent section we consider a symmetric double-dot device in the presence of an asymmetric magnetic field. We observe a resonance in the net spin current through the device, whereas the net charge current vanishes.

5.2 Coherent ratchet devices and adiabatic driving

It was demonstrated experimentally that mesoscopic devices realized by patterned 2DEGs can be used as ratchet systems [38–40], if the symmetry along the direction of transport is broken. In such devices the inelastic mean free path typically is larger than the length of the system so that electrons are transported through the system without inelastic scattering. Therefore, we restrict ourselves to the ballistic regime where the transport properties are dominated by the coherent transmission of electrons. In the absence of thermal noise and dissipation, the electrons are only subject to an external driving, which is realized by an AC voltage $V(t)$. To fulfill the conditions of a ratchet device, the rocking is time-periodic with a period $\mathscr{T}$ and has zero mean,

$$\langle V(t)\rangle = \frac{1}{\mathscr{T}}\int_0^{\mathscr{T}} \mathrm{d}t\, V(t) = 0. \tag{5.4}$$

Here, the brackets $\langle \ldots \rangle$ denote an average over one period of driving in the external voltage. The system is described by a time-dependent Hamiltonian

$$\mathcal{H}^\sigma(t) = -\frac{\hbar^2}{2m}\vec{\nabla}^2 + U(\vec{r}) + V_{\mathrm{es}}(\vec{r},t) + g\mu_B B(\vec{r})\sigma, \tag{5.5}$$

where $V_{\mathrm{es}}(\vec{r},t)$ is the electrostatic potential due to the driving $V(t)$. For our purpose we consider an adiabatic rocking, where the rocking period $\mathscr{T}$ is much larger than the time τ_{st} which is necessary to reach a steady-state,

$$\mathscr{T} \gg \tau_{\mathrm{st}}. \tag{5.6}$$

In that regime, the time variable t plays the role of a parameter, and the current $I(t) = I(V(t))$ is given by the steady-state current for the applied voltage $V(t)$. The net current is then obtained by

$$I_{\mathrm{net}} = \langle I(t)\rangle = \frac{1}{\mathscr{T}}\int_0^{\mathscr{T}} \mathrm{d}t\, I(t). \tag{5.7}$$

For simplicity we assume a square wave rocking

$$V(t) = \begin{cases} +V & \text{for } \nu\mathscr{T} \leq t < (\nu + 1/2)\mathscr{T} \quad \text{(first half period)} \\ -V & \text{for } (\nu + 1/2)\mathscr{T} \leq t < (\nu + 1)\mathscr{T} \quad \text{(second half period)} \end{cases} \tag{5.8}$$

with $\nu \in \mathbb{Z}$, like in the experiments [40]. Then the computation of the net current is reduced to an arithmetic average

$$I_{\text{net}} = \frac{1}{2}\Big[I(+V) + I(-V)\Big]. \tag{5.9}$$

The notion of "adiabatic driving" in the presence of the abrupt changes of $V(t)$ is justified, since the equilibration time τ_{st} to reach a steady-state after the switching is small compared to the driving period, according to Eq. (5.6). Then the current contribution directly following the switching events can be neglected for the computation of the net current.

As already mentioned in the previous section, a nonequilibrium driving is necessary in order to observe a ratchet effect. For electronic devices acting as ratchets this means that the amplitude of the applied AC voltage has to be sufficiently large to reach a situation beyond the linear response regime. In linear response the current is proportional to the applied voltage, $I = GV$, with the conductance G as proportionality factor. Therefore, in the presence of an unbiased adiabatic driving $\langle V(t)\rangle = 0$, see Eq. (5.4), also the net current vanishes,

$$I_{\text{net}} = \langle I(t)\rangle = G\langle V(t)\rangle = 0. \tag{5.10}$$

Hence, electronic devices can operate as ratchets only in the nonlinear regime, where it is important to consider the electrostatic potential drop between the source and drain contacts. This can be done using heuristic models like the assumption of a linear drop or Linke's model which emanates from a potential drop proportional to the gradient of the zero-bias potential, Eq. (4.38). The actual profile of the electrostatic potential has proven to be important, also for the qualitative understanding of the resulting current. If one considers the quantum mechanical transmission of electrons across a potential barrier there are two distinct contributions to the current: a *classical* one which is only influenced by the height of the barrier, and a *quantum mechanical* contribution due to tunneling at energies lower than the barrier height. The latter depends exponentially on the width of the barrier. In the presence of an external bias the potential barrier is deformed affecting both the height and the width of the barrier. So far, Linke's model was successfully employed to describe the experimental outcomes, but a full self-consistent treatment of the electrostatics is still lacking for such systems.

On the theoretical side the idea of mesoscopic ratchet systems was extended to include also the spin degree of freedom in recently proposed spin ratchets [41–46]. The spin degeneracy in that systems is broken either by spin-orbit interaction [41–43] or by magnetic fields [44–46]. The spin-orbit ratchets make use of transitions between the up- and down-branches of different transverse modes that occur when

electrons are transmitted across an adiabatic potential barrier. The Zeeman ratchets use spin-dependent asymmetric ratchet potentials created by magnetic fields. Applying phenomenological models for the voltage drop it was shown that for both types of spin ratchets a net spin current is produced by an external square wave driving. In our calculations presented in the following sections we include a self-consistent treatment of the electrostatics as discussed in Chapter 4. All calculations are carried out at zero temperature $T = 0$, where the Thomas-Fermi density entering the Jacobian for the Newton-Raphson method takes the form of Eq. (4.30). Moreover, to improve the convergence properties we combine the Newton-Raphson iteration scheme introduced in Sec. 4.3 with an underrelaxation according to Eq. (4.21) with a damping factor of $\Omega = 0.75$. Our results show a ratchet effect for both the charge and the spin ratchets and support the results obtained with heuristic models for the electrostatic potential.

5.3 A quantum dot charge ratchet

In this section we investigate the net charge current of an asymmetric mesoscopic device in the presence of a square wave rocking defined in Eq. (5.8). We choose a geometry similar to the device used in Refs. [38, 39] which consists of a triangular quantum dot

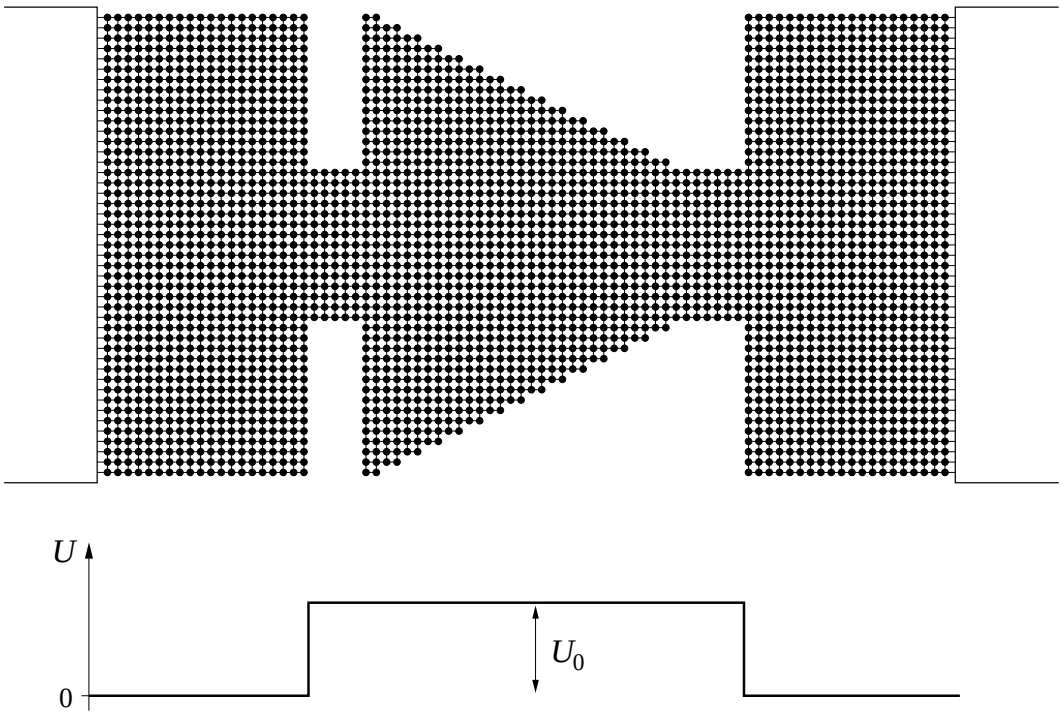

Figure 5.2: Triangular quantum dot connected to leads in lattice representation with lattice constant $a = 37\,\mathrm{nm}$. The confinement potential has an offset $U_0 = 0.04\,\mathrm{meV}$ with respect to the leads.

connected to leads via narrow quantum point contacts, as sketched in Fig. 5.2. The triangle is isosceles with angles of $\arctan(2) = 63.4°$, the width of the leads is $1.7\,\mu$m, and the point contacts are 592 nm wide. The actual device consisting of the dot and the point contacts are energetically offset from the leads by $U_0 = 0.04\,$meV, as indicated in Fig. 5.2.

The system is described by the Hamiltonian (5.5) with zero magnetic field $B(\vec{r}) \equiv 0$, so that the spins $\sigma = \pm 1/2$ are degenerate. The symmetry of the system along the direction of transport is clearly broken, so that the appearance of a ratchet effect is expected. Here the confinement potential plays the role of the ratchet potential. For a given source-drain voltage V we calculate the electrostatic potential profile $V_{\mathrm{es}}(\vec{r})$ self-consistently with the rearrangement of charges, as discussed in Sec. 4.3. Once the converged solution for $V_{\mathrm{es}}(\vec{r})$ is known, one can compute the current using the Meir-Wingreen formula (2.142). The net current $I_{\mathrm{net}} = [I(V)+I(-V)]/2$ as a function of the rocking amplitude V is shown in Fig. 5.3 for different values of the chemical potential μ, with 2-4 open channels in the quantum point contacts. The results indicate that the shape of the current curve strongly depends on the value of the chemical potential. For some fixed values of μ the net current changes its sign with increasing rocking amplitude V. The current traces for $\mu = 0.184\,$meV and $\mu = 0.236\,$meV exhibit one current inversion, for $\mu = 0.212\,$meV we can observe two inversion points. The sign of the net current is visualized in the colormap in Fig. 5.4 for the whole parameter range $V = 0 \ldots 0.04\,$mV and $\mu = 0.16 \ldots 0.3\,$meV. For high chemical potentials $\mu > 0.24\,$meV the net current is primarily positive, for $\mu < 0.24\,$meV we obtain a negative net current with several positive "islands". In conclusion, both the sign and the magnitude of the net current through the considered device can be manipulated by the chemical potential and the rocking amplitude.

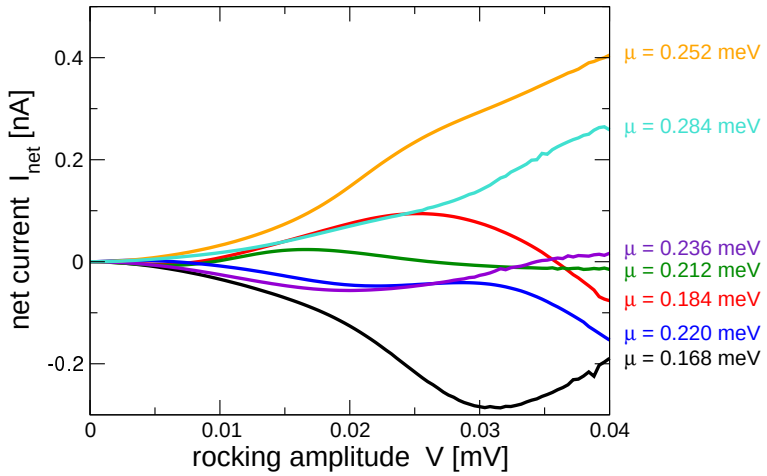

Figure 5.3: Net current as a function of the rocking amplitude V for various chemical potentials μ. The different traces are labeled by the corresponding values of μ.

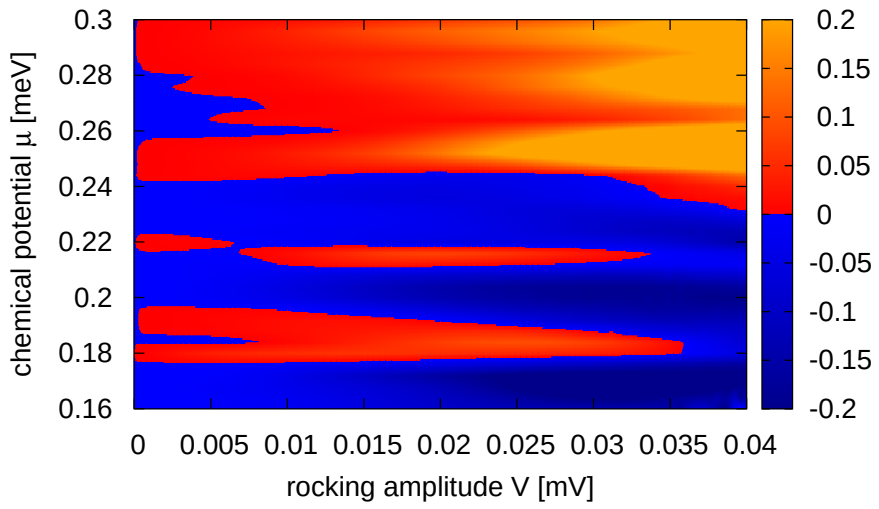

Figure 5.4: Net current as a function of the rocking amplitude V and the chemical potential μ. Red (bright) colors refer to positive values and blue (dark) colors to negative values of I_{net}.

These observations are in qualitative agreement with the experimental results in Refs. [38, 39]. There, net currents of the order of 1 nA were measured, slightly higher than in our results, where we compute currents of about 0.2 nA. This discrepancy arises from the different geometry of the experimental system. The experimental quantum point contact connecting the quantum dot to the leads had a width of about 1/15 of the side length of the triangle. For numerical reasons we used much wider point contacts of 1/3 of the side length in order to allow for 4 open channels in the narrow regions.

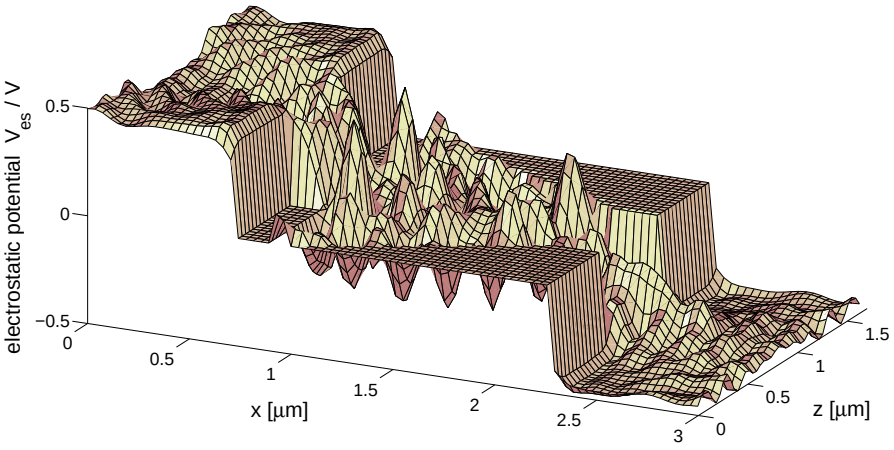

Figure 5.5: Electrostatic potential profile $V_{\text{es}}(\vec{r})$ obtained self-consistently for $\mu = 0.2\,\text{meV}$ and $V = 0.008\,\text{mV}$.

Compared to the width of the contacts the triangle in our simulations is smaller than in the experiments, leading to a "weaker" asymmetry along the direction of transport. This results in a reduced net current compared to the experimental results.

The typical profile of the self-consistent electrostatic potential is displayed in Fig. 5.5 for $\mu = 0.02\,\mathrm{meV}$ and $V = 0.008\,\mathrm{mV}$. The potential mainly drops at the point contacts and becomes almost flat in the leads. Inside the triangular dot we observe only a very weak overall slope of the potential. However, it exhibits strong fluctuations due to the non-uniform charge density in the system. These findings support the heuristic model by Linke *et al.* [38, 39] in which they assumed a step-like voltage drop at the point contacts and weak linear drop throughout the device. By means of this model the authors were also able to qualitatively describe the transport behavior observed in their experiments.

5.4 A resonant tunneling spin ratchet

In this section we extend the idea of the ratchet mechanism to systems which are not spin-degenerate. From the above considerations one may expect a different net current of electrons with opposite spins, if the electron dynamics takes place in a spin-dependent ratchet potential. This can for instance be realized by magnetic fields. The quantity of interest in this context is the spin current I_S, which is in the framework of the Landauer-Büttiker formalism given by [46]

$$I_S = \frac{e}{h}\int \mathrm{d}E\Big[f(E-eV/2,\mu) - f(E+eV/2,\mu)\Big]\sum_{\sigma=\uparrow,\downarrow}\Big(\mathcal{T}_{\uparrow,\sigma}(E) - \mathcal{T}_{\downarrow,\sigma}(E)\Big) \quad (5.11)$$

for a two terminal device[1]. The spin current involves both the spin conserving and non-conserving transmission events. Due to the possibility of spin-flip processes the spin current is usually not conserved throughout the system. The spin current thus depends on the position where it is evaluated. For our purposes we will neglect the spin-flip contributions as explained later in this section, $\mathcal{T}_{\uparrow,\downarrow} = \mathcal{T}_{\downarrow,\uparrow} = 0$, changing the spin current into a conserved quantity. The transmission and current contributions are then characterized by a single spin index σ, and the spin-dependent current contributions are obtained from the Meir-Wingreen formula (2.138) by the corresponding sub-matrices of the Green functions and the self-energies,

$$I_\sigma = \frac{e}{h}\int \mathrm{d}E\,\mathrm{Tr}\Big\{\Sigma^<_{L,\sigma}\mathcal{G}^>_\sigma - \Sigma^>_{L,\sigma}\mathcal{G}^<_\sigma\Big\}. \quad (5.12)$$

The spin current is then given by the difference of the up- and down-component,

$$I_S = I_\uparrow - I_\downarrow, \quad (5.13)$$

[1] Often the spin current is rescaled by a factor of $\hbar/(2e)$, see e.g. [46]

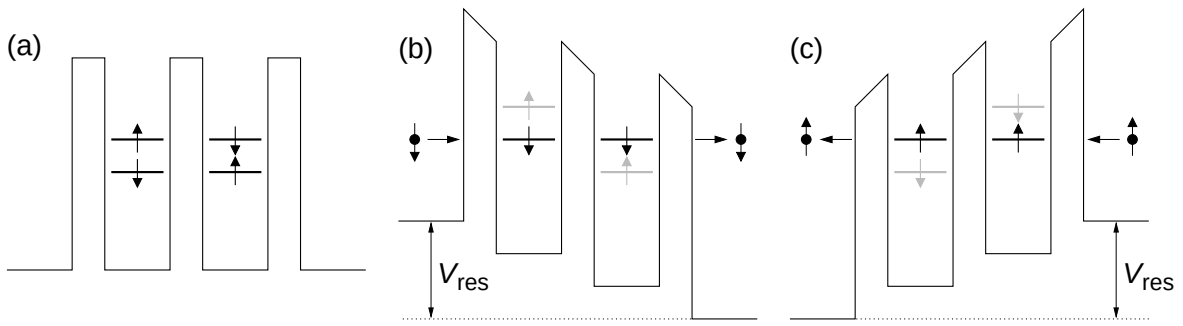

Figure 5.6: Working principle of the double-dot spin ratchet. (a) In equilibrium the energy levels are split due to the Zeeman term. (b) By applying an adequate positive voltage $+V_{\rm res}$ the down-levels are in resonance. (c) For the voltage $-V_{\rm res}$ up-electrons can be resonantly transported through the device in the opposite direction.

whereas the charge current is the sum of both

$$I = I_\uparrow + I_\downarrow. \tag{5.14}$$

A possible realization of a spin ratchet is a resonant tunneling structure, similar to the device in Ref. [154], consisting of two quantum dots coupled to each other and to the leads via tunneling barriers, as schematically drawn in Fig. 5.6(a). In the presence of a magnetic field B the discrete energy levels in the dots split by the Zeeman energy $E_Z = g\mu_B B$, where g is the effective gyromagnetic ratio. By applying an opposite field to the two quantum dots, the energy levels of the up- and down-electrons in the left and right dot are interchanged. An external voltage V shifts the energy levels of the two dots relative to each other. If we assume that the potential only drops across the tunneling barriers, one achieves a resonant situation when the voltage drop between the two dots equals the Zeeman energy E_Z, as depicted in Figs. 5.6 (b) and (c). The resonance voltage $V_{\rm res}$ is given by

$$\frac{1}{3} e V_{\rm res} = E_Z, \tag{5.15}$$

if a fraction of $1/3$ of the applied voltage drops at each barrier. In the resonant situation down-electrons are transported from left to right for a positive voltage and up-electrons flow from right to left for the corresponding negative voltage. This gives rise to a finite spin current I_S through the system in the presence of an external square wave driving with amplitude $V_{\rm res}$.

Within this section we will compute the transport properties of a double-dot spin ratchet quantum mechanically including a self-consistent determination of the potential drop respecting the charging effects for transport in the biased situation. The system under investigation consists of three serial quantum point contacts with a width $W(x) = 500\,\mathrm{nm} - 285\,\mathrm{nm}\cos^2[(x - x_0)\pi/475\,\mathrm{nm}]$ forming two coupled quantum dots

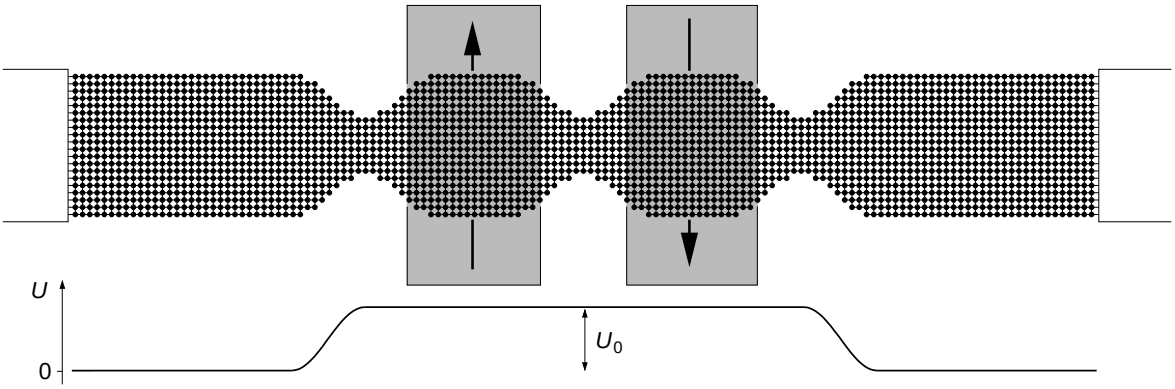

Figure 5.7: Geometry of the double-dot device in lattice representation with lattice constant $a = 24\,\mathrm{nm}$. The width of the waveguide is 500 nm and the three constrictions are 215 nm wide with a distance of 720 nm between each. The gray bars indicate the location of the magnetic stripes and the confinement potential $U(x)$ is shown below the system with $U_0 = 0.56\,\mathrm{meV}$.

connected to leads, as depicted in Fig. 5.7. The width of the leads is 500 nm, the distance between two neighboring quantum point contacts is 720 nm and the constrictions are 215 nm wide. The confinement potential is of hard-wall type and we include a potential offset $U_0 = 0.56\,\mathrm{meV}$ with respect to the band bottom of the leads, which drops at the leads according to the sinusoidal switching function (3.13). On top of the device there are ferromagnetic stripes with a constant magnetization $\vec{M}$ with opposite orientation. They are mounted upon the semiconductor heterostructure as sketched in Fig. 5.8. In ferromagnetic metals like dysprosium a magnetization up to about $\mu_0 M = 3\,\mathrm{T}$ can be created [155], where μ_0 is the magnetic permeability. The magnetization is oriented along the z-direction and gives rise to a magnetic field inside the 2DEG. The magnetic field of a ferromagnet with homogeneous magnetization $\vec{M}$ is

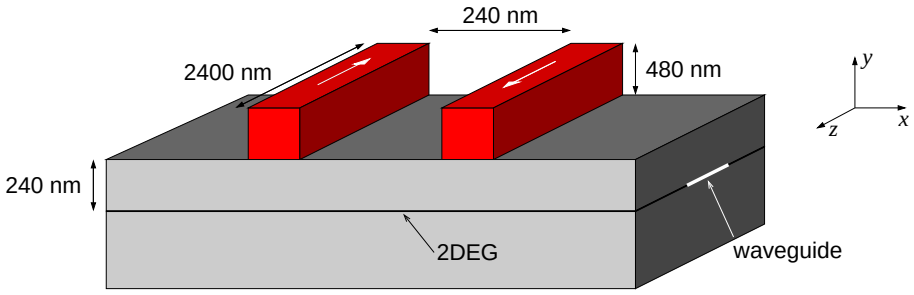

Figure 5.8: Semiconductor heterostructure with a 2DEG forming at the interface. On the top there are two ferromagnets across the waveguide which are oppositely magnetized as indicated by the white arrows. The magnetic stripes have a quadratic cross-section with a side length of 480 nm and a length of 2400 nm. Their distance to the 2DEG is 240 nm.

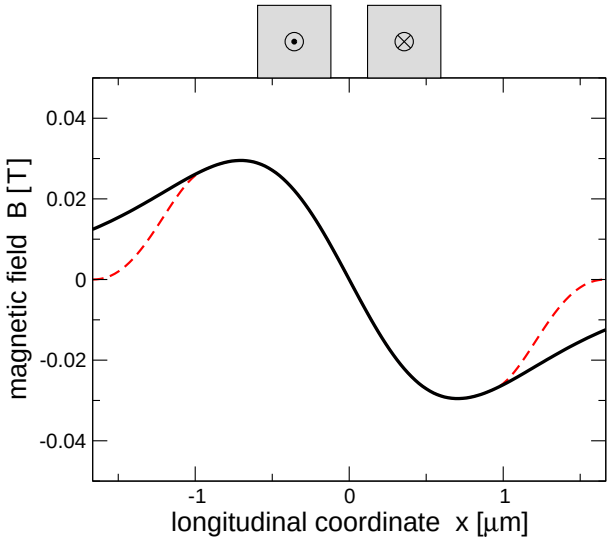

Figure 5.9: Magnetic field in the plane of the 2DEG created by the arrangement of ferromagnets shown in Fig. 5.8 with $\mu_0 M = 3\,\mathrm{T}$ at the central transverse position of the waveguide. The dashed line shows the field used for the simulations, which is truncated to the end of the scatterer. The gray squares indicate the position and the magnetization of the ferromagnets.

given by [156]

$$\vec{B}(\vec{x}) = -\frac{\mu_0}{4\pi}\vec{\nabla}\oint_S \mathrm{d}\vec{x}'\,\frac{\vec{M}\cdot\hat{u}(\vec{x}')}{|\vec{x}-\vec{x}'|}, \tag{5.16}$$

where the integral runs over the surface S of the magnetic stripe and $\hat{u}(\vec{x}')$ is the unit vector normal to the surface at position $\vec{x}'$. In this setup the x- and y-components of the magnetic field are small compared to the z-component [44] which allows us to consider the z-component only. Then the Zeeman term takes the form $g\mu_B B(\vec{r})\sigma$ with $B(\vec{r}) = B_z(\vec{r})$ and $\sigma = \pm 1/2$, as used in the Hamiltonian (5.5). In that case the Hamiltonian does not couple different spins, so that spin-flip processes are absent. Moreover it was shown in Ref. [44] that for symmetry reasons the spin-flip contributions induced by B_x and B_y cancel, if the confinement potential of the waveguide is symmetric in z-direction and the ferromagnets are precisely centered above the quantum wire.

The magnetic field present in the plane of the 2DEG due to two ferromagnetic stripes arranged as in Fig. 5.8 is calculated by means of Eq. (5.16). Since the ferromagnets are much longer than the width of the quantum wire, the magnetic field exhibits only a weak z-dependence. Therefore we use the field configuration in the transverse center of the system, shown in Fig. 5.9, as a z-independent quantity for our simulations. Moreover, for numerical reasons we truncate the magnetic field in the lead parts of the system according to the switching function (3.13), in order to reduce the computational effort. This does not affect the results significantly, since

only the magnetic field inside the quantum dots is crucial for the working principle of the considered ratchet system.

Although the geometry of the system is perfectly symmetric along the direction of transport, the system works as a spin ratchet. For the different spin components the spatial inversion symmetry is broken individually by the magnetic field generated by the magnetized ferromagnetic stripes. The potential of the up-electrons is proportional to the magnetic field shown in Fig. 5.9, whereas the down-electrons encounter the inverse potential. Because of the geometry of the system the Hamiltonian (5.5) is symmetric along the x-direction if the spins are exchanged and the voltage is inverted,

$$\mathcal{H}^{\sigma}(x,V) = \mathcal{H}^{-\sigma}(-x,-V). \tag{5.17}$$

A corresponding symmetry thus holds for the currents through the device: if the voltage is reversed the current changes its direction and the roles of up- and down-electrons are interchanged,

$$I_{\sigma}(V) = -I_{-\sigma}(-V). \tag{5.18}$$

For that reason one obtains a net spin current according to the definition (5.13)

$$I_S^{\mathrm{net}} = \frac{1}{2}\Big[I_S(V) + I_S(-V)\Big] = I_{\uparrow}(V) - I_{\downarrow}(V), \tag{5.19}$$

whereas the net charge current vanishes,

$$I_{\mathrm{net}} = \frac{1}{2}\Big[I(V) + I(-V)\Big] = 0. \tag{5.20}$$

The strongly peaked density of states of the considered system is shown in Fig. 5.10 in the range of the two lowest energy levels of the dots. In the absence of a magnetic

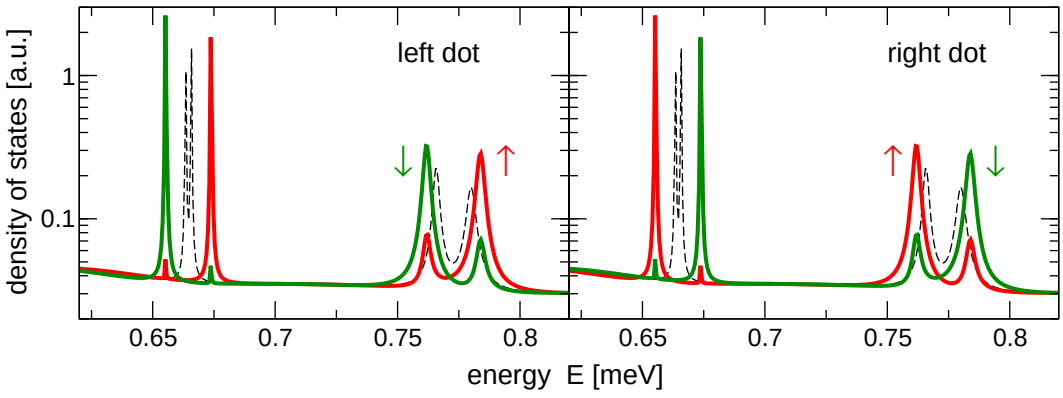

Figure 5.10: Density of states in arbitrary units for $M = 0$ (black dashed line), which is identical for the two spin species. The red and green lines show the density of states of the up- and down-electrons, respectively, in the presence of a magnetization of $\mu_0 M = 3\,\mathrm{T}$.

field each level appears as a double-peak in the density of states, since the two dots are identical. If the magnetic field is present the peaks corresponding to the different spins are clearly split and the up- and down-peaks are interchanged in the left and right dot. In order to obtain a sufficiently large splitting we take the material parameters of InAs with a large g-factor of $g = 15$, an effective mass of $m = 0.024m_0$ and a dielectric constant $\varepsilon = 15.15$ [122]. In order to observe a resonant current through the device, the chemical potential μ has to be located in the vicinity of one of the energy levels of the dot. An applied source-drain voltage shifts the energy levels and electrons can be transported if a level lies within the bias window $|\mu - eV/2| < E < |\mu + eV/2|$. Due to this rearrangement unoccupied levels can be occupied, or vice versa. This may lead to an accumulation or reduction of charges in the device, which affects the electrostatic potential. Since the lower energy level around $E \approx 0.66\,\mathrm{meV}$ is very sharp, the charge redistribution happens abruptly causing convergence problems for the self-consistent scheme for the computation of the potential drop. For that reason we restrict ourselves to the second level and set the chemical potential to the value $\mu = 0.773\,\mathrm{meV}$, in the center of the second double-peak in the density of states. The first energy level of the constrictions with a width $W = 215\,\mathrm{nm}$ is located at $E_1 = \hbar^2\pi^2/(2mW^2) = 0.9\,\mathrm{meV}$, including the potential offset of $U_0 = 0.56\,\mathrm{meV}$, see Fig. 5.7. Therefore, with our choice of μ the transport takes place in the tunneling regime.

The spin-resolved current components I_σ obtained with the self-consistent electrostatic potential are displayed in Fig. 5.11 as a function of the applied voltage V. The ferromagnetic stripes are magnetized with $\mu_0 M = 3\,\mathrm{T}$ and the chemical potential is $\mu = 0.773\,\mathrm{meV}$. We observe a resonance behavior in the current with maxima located at $V_{\mathrm{res}} = \pm 0.038\,\mathrm{mV}$. In the forward direction $V = +V_{\mathrm{res}}$ the down-current dominates,

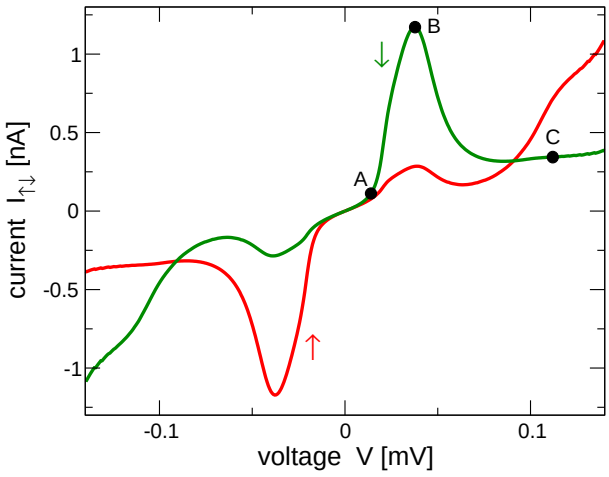

Figure 5.11: Spin-resolved current of the up (red) and down (green) electrons as a function of the applied voltage V for a magnetization of $\mu_0 M = 3\,\mathrm{T}$. The letters A, B and C mark the positions where the density of states is displayed in Fig. 5.13.

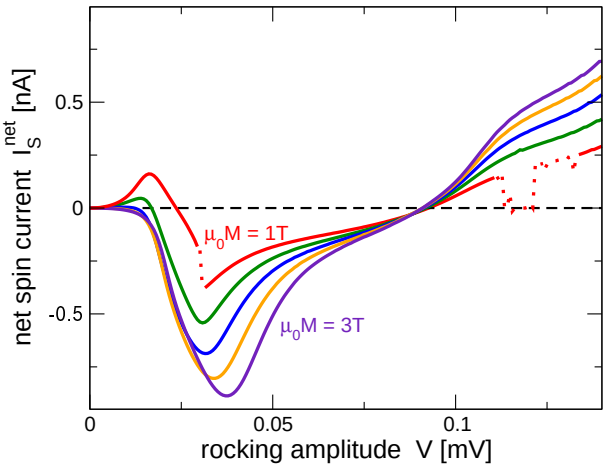

Figure 5.12: Net spin current I_S^{net} for different magnetizations $\mu_0 M = 1\,\text{T} \ldots 3\,\text{T}$ in steps of 0.5 T from low to high values of $|I_S|$. The dashed line represents the net charge current and the dotted segments of the 1 T-curve mark the regions where the self-consistency routine did not converge.

whereas for $V = -V_{\text{res}}$ the up-current is the larger component. The numerical results verify the symmetry relation (5.18) for the different spin components of the current. The net spin current is plotted in Fig. 5.12 for various magnetizations between 1 T and 3 T. The overall shape of the different curves is similar but the magnitude of the spin current increases with increasing magnetization. Also the location of the maximum spin current changes with M. All curves of the spin current change their sign at a driving amplitude of $V \approx 0.092\,\text{mV}$. This voltage approximately corresponds to the level spacing between the first and second mode in the quantum dots, see Fig. 5.10. Since the level spacing is large compared to the Zeeman energy E_Z the spin current inversion point is almost independent of M. The low-field curves for $\mu_0 M \leq 2\,\text{T}$ exhibit an additional spin current inversion at low rocking amplitudes $V < 0.025\,\text{mV}$. Moreover, for the 1 T result the numerical scheme did not fully converge in some regions, which causes the discontinuities in the spin current.

The obtained spin current characteristics can be understood from the evolution of the density of states with an applied bias shown in Fig. 5.13. With increasing voltage the down-levels of the left and right dot approach each other, whereas the up-levels drift apart, as also suggested by Fig. 5.6. At the resonance voltage $V_{\text{res}} = 0.038\,\text{mV}$ (point B in Fig. 5.11) the density of states of the down-particles form a double-peak which is almost identical for the two dots. The double-peak is completely located within the bias window, thus giving rise to the high value of the down-current. The density of states of the up-electrons at $V = V_{\text{res}}$ shows a weak resonance at the borders of the bias window causing a slight enhancement of the up-current in that voltage range as observed in Fig. 5.11. By further increasing the applied voltage the down-levels of the left and right dot drift away from each other, whereas the first up-level of the left dot and the second up-level of the right dot approach each other. At $V = 0.112\,\text{mV}$ we find

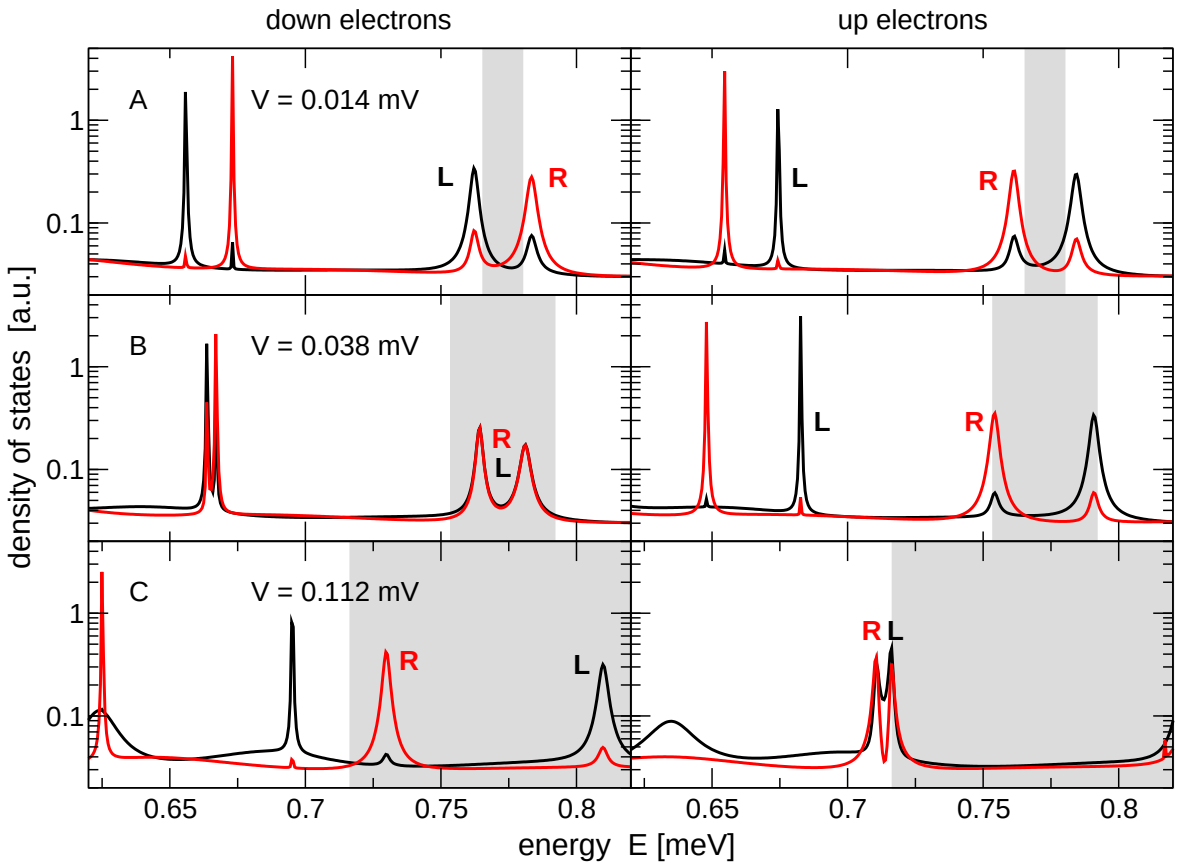

Figure 5.13: Density of states of the down-electrons (left column) and up-electrons (right column) for different voltages V corresponding to the points A, B and C in Fig. 5.11. The black curves (L) refer to the density of states in the left dot, the red curves (R) to the right dot. The gray shading marks the bias window around the chemical potential $\mu = 0.773\,\mathrm{meV}$. The ferromagnets are magnetized with $\mu_0 M = 3\,\mathrm{T}$.

a resonance of the up-levels, which is however only partially overlapping with the bias window. This explains the enhanced up-current in the high voltage regime observed in Fig. 5.11.

For the working principle of the presented spin ratchet the electrostatic potential drop is of great relevance. The results for the quantum wire (Fig. 4.7) and the triangular quantum dot (Fig. 5.5) imply that the potential predominantly drops at the quantum point contacts. This would lead to the picture shown in Fig. 5.6, in line with Linke's model for the potential drop, Eq. (4.38). In Fig. 5.14 we present the numerical results for the electrostatic potential $\overline{V}_{\mathrm{es}}(x)$ averaged over the transverse coordinate, see Eq. (4.37), where we can distinguish three different regimes: at low voltages we find a triple-step structure with a comparatively small drop between the two quantum dots, as shown in Fig. 5.14(a). In the range of high voltages displayed in Fig. 5.14(c) the volt-

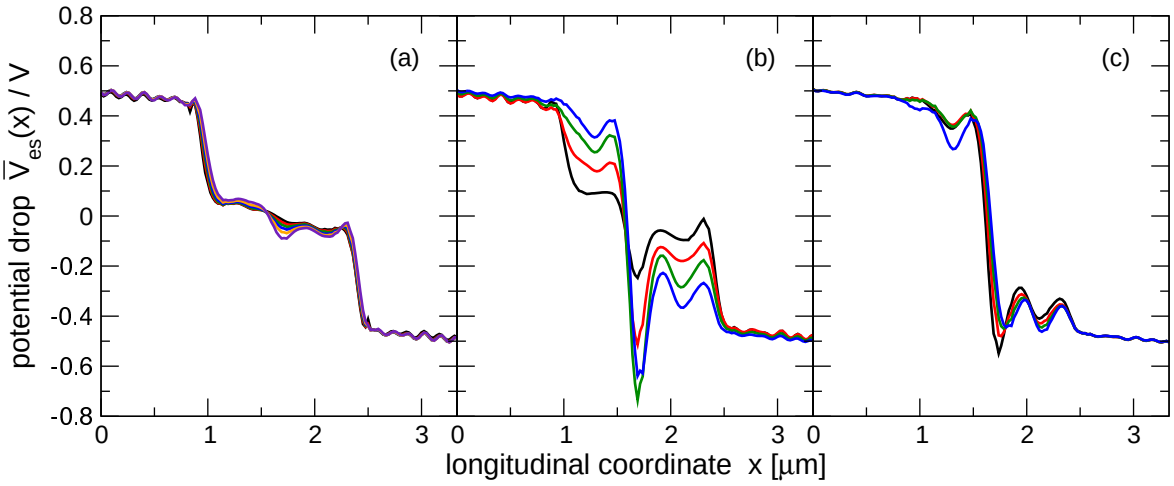

Figure 5.14: The electrostatic potential $\overline{V}_{\rm es}(x)$ scaled with the applied voltage V for different voltage ranges: (a) $V = 0.003\,\mathrm{mV} \ldots 0.017\,\mathrm{mV}$, (b) $V = 0.022\,\mathrm{mV} \ldots 0.056\,\mathrm{mV}$, and (c) $V = 0.070\,\mathrm{mV} \ldots 0.112\,\mathrm{mV}$.

age drops almost exclusively at the central point contact between the two dots. In the intermediate voltage regime there is a crossover from the triple-step to the single-step profile of the electrostatic potential, which is seen in Fig. 5.14(b).

Despite the non-trivial behavior of the voltage drop, we now use a simplified model to describe the electrostatic potential. According to Linke's model, Eq. (4.38), we assume a triple-step structure of the electrostatic potential with a parameter α giving the fraction of voltage that drops at the central constriction. The fraction that drops at

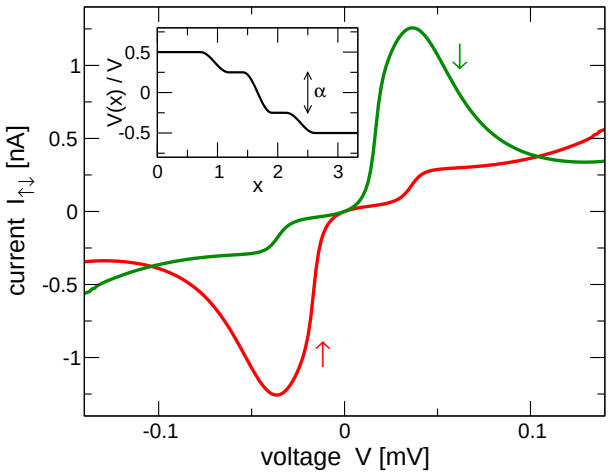

Figure 5.15: Spin-resolved current contributions of the up (red) and down (green) electrons obtained by a step-like potential drop shown in the inset with $\alpha = 0.5$.

the left and right point contacts is accordingly $(1-\alpha)/2$. Between the constant sections of the potential the interpolation is sinusoidal according to Eq. (3.13). For $\alpha = 0.5$ the electrostatic potential is shown in the inset of Fig. 5.15. The spin-resolved current contributions obtained with this model for $\alpha = 0.5$ are presented in Fig. 5.15. The overall behavior is similar to the self-consistent results in Fig. 5.11. Also the position and the height of the resonance peak is well reproduced for the chosen value of α. Unlike in the previous results the peak width is larger and the up- and down-currents intersect at a higher voltage. Those features can be related to the transition of the potential drop to a single-step profile, which is not captured by this simple model. This transition would correspond to a voltage dependent parameter α approaching unity in the high voltage regime. However, to understand the working principle of the double-dot device a triple-step voltage drop is sufficient and the simple picture shown in Fig. 5.6 properly describes the relevant physics.

5.5 Recapitulation

In this chapter we discussed two-dimensional mesoscopic devices with a broken spatial inversion symmetry exposed to a periodic and symmetric square wave driving. Due to the built in asymmetry of the devices the currents in the two rocking situations with $+V$ and $-V$ are in general different, if the voltage is sufficiently large in order to reach the nonlinear regime, see Eq. (5.10). In that regime the electrostatic potential profile plays an important role for the transport properties of the system. Going beyond the approaches using heuristic models for the electrostatic potential profile, we calculated the potential drop self-consistently with the rearrangement of charges in the biased system.

The first system we considered was a triangular quantum dot similar to the device used in experiments by Linke *et al.* in Refs. [38, 39]. We found a rectifying behavior in the presence of a symmetric driving giving rise to a finite net current through the device. The sign and the magnitude of the observed net current strongly depend on the rocking amplitude and the chemical potential. Changing one of the external parameters may cause current inversions, as also observed experimentally. The obtained profile of the electrostatic potential supports the heuristic model used in Refs. [38, 39] to qualitatively describe the IV-characteristics observed in the experiments.

The second system under investigation was a symmetric double-dot with oppositely magnetized ferromagnetic stripes. We found a resonance behavior in the spin-resolved current components leading to a finite net spin current. Since we chose the chemical potential to be located in the center of the double-peak in the density of states, the charging effects were minimized. The bias window opens symmetrically over the double-peak, when an external voltage is applied. Therefore, the upper peak is populated and simultaneously the lower peak is depopulated, keeping the total number of electrons in the system nearly constant. If the chemical potential is located at a different value, charging effects influence the energy spectrum of the quantum dots,

which causes problems for the self-consistent calculation scheme.

The fact that we can reproduce the IV-characteristics of the double-dot spin ratchet with a heuristic model of a step-like potential drop indicates that the electrostatic potential profile is not crucial for the working principle of the considered device. The only important condition is a finite potential offset between the two dots, which may also be achieved by the assumption of a linear potential drop. We showed results for a step-like profile of the electrostatic potential where a fraction α of the applied voltage drops between the two quantum dots. The parameter α thus determines the location and the width of the resonance in the spin current, as the resonance condition reads

$$\alpha e V_{\mathrm{res}} = E_Z. \tag{5.21}$$

For a small value of α a large voltage is necessary to reach the resonant situation; for values of α close to unity a correspondingly smaller voltage is sufficient. The insensitivity of the qualitative shape of the IV-characteristics towards the profile of the potential drop implies that the heuristic models used in Refs. [41–46] adequately describe the fundamentals of the considered spin ratchet devices.

CHAPTER 6

Summary and perspectives

The study of quantum transport in mesoscopic devices is an important issue with regard to future applications of nanosystems as electronic components. After Landauer's seminal work [32, 33], a way to obtain the conductance of a quantum system from its equilibrium transmission amplitudes was available. This allowed the description of transport of effectively noninteracting particles in the linear response regime, where the current I depends linearly on the applied voltage V. The Landauer approach provides a transparent physical picture of transport and it has proven to be sufficient for many applications. In some cases, however, the interactions between the electrons play an important role, like for the interpretation of the 0.7 conductance anomaly. Also the description of transport beyond the linear regime requires the consideration of the electrostatic potential created by the internal interactions among the electrons. In our work we therefore focused on the question how the transport properties are influenced by the explicit consideration of electron-electron interaction effects.

For the theoretical description of the transport problem we employed the well established nonequilibrium Green function formalism. It allows for the presence of finite source-drain voltages and incorporates the interaction effects in a perturbative way via a self-energy. For our simulations we restricted ourselves to the self-consistent Hartree-Fock or Hartree level, respectively, which corresponds to the first order of the perturbation expansion. After introducing the concepts of the Green function method we presented the effective mass Hamiltonian describing the dynamics of electrons in a 2DEG. For the numerical simulations the spatial coordinates were discretized to a square lattice leading to a Hamilton matrix. Along the same lines the Green functions were represented by matrices as well. We then showed how to extract the relevant physical quantities out of the Green functions. For our purposes the density of states, the particle density, the conductance and the current were of interest.

The first problem we investigated is the transport of electrons through a quantum point contact in the presence of short-range electron-electron interactions. We

restricted ourselves to the linear regime and modelled the interaction potential between the particles by a delta potential. In Hartree-Fock approximation this type of interactions leads to a repulsion of electrons with different spins. In a certain range of parameters the interaction favors an asymmetric occupation of the spin-up and spin-down states, leading to a local spin polarization in the system. We found that this model – despite its simplicity – is suitable to describe many features of the 0.7 conductance anomaly, which appears as a small shoulder in the conductance traces below the first quantized plateau, at a value of around $0.7 \times G_0$. In agreement with experimental results we find a non-quantized plateau below the first conductance step which evolves towards the Zeeman spin-split plateau at $0.5 \times G_0$ when an in-plane magnetic field is applied. In addition, a so-called 0.7 analog appears at high magnetic fields where Zeeman split energy levels intersect. We recover a suppression of shot noise at the 0.7 feature, which was also reported by experimentalists. The observed temperature dependence of the 0.7 feature, however, cannot be described properly by our model. In experiments the 0.7 plateau gets more pronounced with increasing temperature; in our results the feature is washed out by finite temperatures and eventually vanishes. In order to justify our choice of the interaction potential we presented qualitatively similar results for the conductance obtained with a Coulomb interaction potential, and we discussed the connection between both. We furthermore pointed out, that our approach also holds for the description of transport of cold fermionic atoms.

An obvious extension of the present work is the consideration of higher orders in the interaction. There is evidence that higher order contributions may yield the correct temperature dependence, as the Kondo model [97] or the consideration of second order interaction events [113] reveal the correct tendency of the temperature behavior. One possibility to go beyond the scope of the present work is the description of the interactions on the level of the random-phase approximation, see e.g. [157]. In this regard the electron-electron interaction is renormalized by considering fermion bubbles in the Feynman diagrams. In that way correlations are introduced in the description of interacting electrons. Such correlations may on the one hand influence the temperature dependence of the 0.7 structure. On the other hand the random-phase approximation is known to account for the screening of the electron-electron interactions. Therefore another interesting question in this regard is the connection between the Coulomb interaction in random-phase approximation and our model of short-range interactions. Since the recursive algorithm used in our calculations does not work beyond the Hartree-Fock approximation, and since an additional energy integral over Green functions is involved in random-phase approximation, the numerical effort is expected to increase significantly. Nevertheless, for systems with a larger lattice spacing such computations are manageable.

The second issue of our work was the treatment of two-dimensional mesoscopic systems in the presence of a finite bias voltage. Because an applied bias shifts the energy spectrum of the contacts, it is inevitable to include an electrostatic potential, which continuously interpolates between the band bottom of the leads, in order not to introduce artificial discontinuities. On a phenomenological level one can assume a

certain profile of the electrostatic potential, like for instance a linear potential drop. To provide a more realistic description of transport we presented a way to determine the electrostatic potential, which is created by the interactions between the electrons in the system, self-consistently with the rearrangement of charges. We included the electron-electron interactions on the Hartree level, which corresponds to the consideration of the classical electrostatic potential. Since the coupled system of equations for the charge density and the electrostatic potential is highly nonlinear, sophisticated numerical methods are required. As a first condition the particle density has to be determined with high accuracy. This was allowed for by a numerical complex contour integration of the density of states, instead of a real energy integration. Second, as the electrostatic potential $V_{\mathrm{es}}(\vec{r})$ is sensitive to small changes in the charge density, we used a Newton-Raphson method to compute $V_{\mathrm{es}}(\vec{r})$. Moreover we underrelaxed the obtained electrostatic potential during the self-consistency routine, in order to improve the convergence properties. With these steps included the numerical scheme turned out to work well for the systems we considered. Nevertheless, for some distinct sets of parameters it was not possible to achieve a converged solution for the potential drop.

The self-consistent method to determine the electrostatic potential drop was applied to investigate ballistic ratchet devices, where the profile of the potential drop plays a crucial role. A ratchet system can create a nonvanishing net current when exposed to a symmetric AC driving, if it is operated in the nonlinear transport regime. First we studied the transport properties of a triangular quantum dot acting as a charge ratchet in presence of a square wave rocking. We found a finite net current and – similar to the experimental results – current inversions were observed when varying the rocking amplitude or the chemical potential. Our results furthermore showed that the potential predominantly drops at the point contacts connecting the quantum dot to the leads, which justifies the model approach used in Ref. [38]. Besides that we investigated a double-dot system acting as a resonant tunneling spin ratchet. By oppositely magnetized ferromagnetic stripes mounted above the quantum dots one can split the energy levels of the up- and down-electrons inside the dots. If the appropriate voltage is applied the energy levels of one spin species are aligned leading to a resonant current of electrons with the corresponding spin, while electrons with the opposite spin are hardly transmitted. For negative voltages the spins change their roles, so that on average a net spin current flows through the system. Due to the symmetry of the chosen system the net charge current exactly vanishes. Such a device may be used as a "spin battery" in future spintronics devices.

Besides the considered resonant tunneling spin ratchet, also spin-orbit ratchets [41–43] and Zeeman ratchets [44–46] were proposed, which work in the nonlinear transport regime as well. However, so far only heuristic model approaches to the potential drop were considered. In order to justify the assumptions made for the electrostatics, a full self-consistent treatment of the problem would be appropriate. This could be realized along the same lines as presented in this work. However, as seen from our results, the simple model of a step-like potential drop accounts very well for the observed features in the IV-curve of the double-dot spin ratchet. Since different profiles for

the electrostatic potential have been considered for the spin-orbit and Zeeman ratchets yielding qualitatively similar results, we expect only quantitative changes when the potential drop is computed self-consistently. For the understanding of the working principle of the different spin ratchets, the applied model approaches are supposed to be sufficient.

Since for the ratchet systems the electron-electron interactions were only considered on the Hartree level, a possible extension is the inclusion of exchange interactions or higher order corrections. In Chapter 3 we have shown that the exchange contribution is responsible for the spin splitting of the up- and down-energy levels. In the case of the resonant tunneling spin ratchet the Zeeman splitting will be increased by the exchange interaction, resulting in a shift of the resonance voltage V_{res}. Also higher order contributions may influence the precise shape of the IV-characteristics, but the functionality of the presented ratchet device is not expected to be strongly affected.

In conclusion, we have shown regimes of mesoscopic transport where interaction effects among the electrons are of great relevance. We presented numerical results including a self-consistent treatment of the interactions on the level of the Hartree-Fock or Hartree approximation, respectively. Most of the results on the 0.7 anomaly and on the quantum dot charge ratchet are in agreement with experimental findings and with other theoretical approaches. The section about the spin ratchet extends present theoretical works on that subject with regard to the electrostatic potential drop. Although spin ratchet devices still await their experimental realization, they might be used to generate spin polarized currents in the near future.

APPENDIX A

Interaction self-energy in Hartree-Fock approximation

Within the Green function formalism the electron-electron interaction can be included in a perturbative way by expanding the S-matrix, Eq. (2.39), in powers of field operators as demonstrated in Eq. (2.42). This perturbation expansion is valid for both the time ordered Green function in equilibrium and also for the contour-ordered Green function in nonequilibrium problems. Here we write down the equations for the time-ordered Green function, but the corresponding expressions for the contour-ordered function are obtained by replacing the time-ordering operator $\hat{\mathsf{T}}$ by the contour-ordering operator $\hat{\mathsf{T}}_C$ and the real time integrals by integrals along the Keldysh contour.

The 0-th order of the expansion neglects all interactions and we recover the free Green function

$$\mathcal{G}^{\sigma,\sigma}(\vec{x},\vec{x}';t,t') = \mathcal{G}_0^{\sigma,\sigma}(\vec{x},\vec{x}';t,t') = -\frac{\mathrm{i}}{\hbar}\left\langle \hat{\mathsf{T}}\,\hat{\Psi}_\sigma(\vec{x},t)\hat{\Psi}^\dagger_\sigma(\vec{x}',t')\right\rangle . \tag{A.1}$$

Here we explicitly write the spin index σ. Since we only consider spin-conserving electron-electron interactions, the Green function has to be diagonal in the spin variable.

In the first order of the perturbation expansion, which is known as the Hartree-Fock approximation, the Green function according to Eq. (2.42) is given by

$$\begin{aligned}\mathcal{G}^{\sigma,\sigma}(\vec{x},\vec{x}';t,t') = -\frac{\mathrm{i}}{\hbar}\left\langle \hat{\mathsf{T}}\,\hat{\Psi}_\sigma(\vec{x},t)\hat{\Psi}^\dagger_\sigma(\vec{x}',t')\right\rangle + \frac{1}{2}\left(\frac{\mathrm{i}}{\hbar}\right)^2 \sum_{\sigma_1,\sigma_2}\int \mathrm{d}^3x_1\int \mathrm{d}^3x_2\int \mathrm{d}t_1 \times \\ \times\, w(\vec{x},\vec{x}')\left\langle \hat{\mathsf{T}}\,\hat{\Psi}^\dagger_{\sigma_1}(\vec{x}_1,t_1)\hat{\Psi}^\dagger_{\sigma_2}(\vec{x}_2,t_1)\hat{\Psi}_{\sigma_2}(\vec{x}_2,t_1)\hat{\Psi}_{\sigma_1}(\vec{x}_1,t_1)\hat{\Psi}_\sigma(\vec{x},t)\hat{\Psi}^\dagger_\sigma(\vec{x}',t')\right\rangle .\end{aligned} \tag{A.2}$$

To be precise, the right hand side of the above equation has to be divided by the expansion of the S-matrix, as shown in Eq. (2.41). However, we now apply Wick's theorem in order to evaluate the expectation value of the product of field operators and then, according to the cancellation theorem, all disconnected diagrams of the numerator, see Eqs. (A.4) and (A.5), are cancelled by the denominator.

According to Wick's theorem [26–28, 50] the time-ordered product of field operators can be rewritten into a sum of their normal products with all possible contractions. The normal ordering relocates all annihilation operators to the right, wherefore the expectation value of a normal-ordered product of field operators vanishes. Thus, only the fully contracted term contributes to the Green function. The contraction of two field operators defined in Eq. (2.43) is just a number. Hence it can be put outside the expectation value and it gives

$$\begin{aligned}\underbrace{\hat{\Psi}(\vec{x}_1,t_1)\hat{\Psi}^\dagger(\vec{x}_2,t_2)} &= \Big\langle \underbrace{\hat{\Psi}(\vec{x}_1,t_1)\hat{\Psi}^\dagger(\vec{x}_2,t_2)} \Big\rangle = \\ &= \Big\langle \hat{\mathtt{T}}\,\hat{\Psi}(\vec{x}_1,t_1)\hat{\Psi}^\dagger(\vec{x}_2,t_2)\Big\rangle - \Big\langle \hat{\mathtt{N}}\,\hat{\Psi}(\vec{x}_1,t_1)\hat{\Psi}^\dagger(\vec{x}_2,t_2)\Big\rangle = \\ &= \Big\langle \hat{\mathtt{T}}\,\hat{\Psi}(\vec{x}_1,t_1)\hat{\Psi}^\dagger(\vec{x}_2,t_2)\Big\rangle = \mathrm{i}\hbar\mathcal{G}_0(\vec{x}_1,\vec{x}_2;t_1,t_2).\end{aligned} \tag{A.3}$$

So the time-ordered products of field operators appearing in the perturbation expansion of the Green function can be written as a sum of all possible contractions, which are related to the free Green function $\mathcal{G}_0$.

Applying Wick's theorem to the product of six field operators in Eq. (A.2) and noticing that contractions of two creation or two annihilation operators gives zero, we end up with six possible contractions. Two of those contractions are so-called *disconnected diagrams*:

$$\begin{aligned}&\Big\langle \hat{\mathtt{T}}\,\hat{\Psi}^\dagger_{\sigma_1}(\vec{x}_1,t_1)\hat{\Psi}_{\sigma_1}(\vec{x}_1,t_1)\Big\rangle\Big\langle \hat{\mathtt{T}}\,\hat{\Psi}^\dagger_{\sigma_2}(\vec{x}_2,t_1)\hat{\Psi}_{\sigma_2}(\vec{x}_2,t_1)\Big\rangle\Big\langle \hat{\mathtt{T}}\,\hat{\Psi}_{\sigma}(\vec{x},t)\hat{\Psi}^\dagger_{\sigma}(\vec{x}',t')\Big\rangle = \\ &= (\mathrm{i}\hbar)^3\,\mathcal{G}^<_{\sigma_1,\sigma_1}(\vec{x}_1,\vec{x}_1;t_1,t_1)\,\mathcal{G}^<_{\sigma_2,\sigma_2}(\vec{x}_2,\vec{x}_2;t_1,t_1)\,\mathcal{G}_0^{\sigma,\sigma}(\vec{x},\vec{x}';t,t') =\end{aligned} \tag{A.4}$$

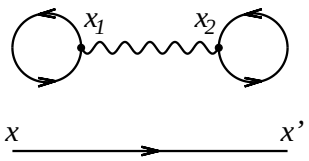

and

$$\begin{aligned}&\Big\langle \hat{\mathtt{T}}\,\hat{\Psi}^\dagger_{\sigma_1}(\vec{x}_1,t_1)\hat{\Psi}_{\sigma_2}(\vec{x}_2,t_1)\Big\rangle\Big\langle \hat{\mathtt{T}}\,\hat{\Psi}^\dagger_{\sigma_2}(\vec{x}_2,t_1)\hat{\Psi}_{\sigma_1}(\vec{x}_1,t_1)\Big\rangle\Big\langle \hat{\mathtt{T}}\,\hat{\Psi}_{\sigma}(\vec{x},t)\hat{\Psi}^\dagger_{\sigma}(\vec{x}',t')\Big\rangle\delta_{\sigma_1,\sigma_2} = \\ &= -(\mathrm{i}\hbar)^3\delta_{\sigma_1,\sigma_2}\,\mathcal{G}^<_{\sigma_1,\sigma_2}(\vec{x}_1,\vec{x}_2;t_1,t_1)\,\mathcal{G}^<_{\sigma_2,\sigma_1}(\vec{x}_2,\vec{x}_1;t_1,t_1)\,\mathcal{G}_0^{\sigma,\sigma}(\vec{x},\vec{x}';t,t') =\end{aligned} \tag{A.5}$$

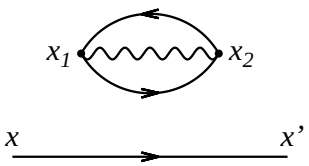

In the Feynman diagrams shown with the corresponding equations a solid line represents a free propagation described by the unperturbed Green function and the wavy line is an interaction line. A closed bubble from a point $\vec{x}$ back to the same point stands for the electron density at $\vec{x}$. From the Feynman diagrams one can easily see that for those two contractions the interaction part is decoupled from the original propagation from $\vec{x}$ to $\vec{x}'$. The lesser Green functions in the above equations appear, because the order of the field operator has to be maintained for equal time arguments. If the field operators contain different times, they can be commuted after including a minus-sign.

According to the cancellation theorem [26–28] the above displayed disconnected terms are cancelled by the corresponding terms in the denominator, so there are four contractions left, where only two of them are different. The first one reads

$$\begin{aligned} &2\left\langle \hat{\mathrm{T}}\,\hat{\Psi}^\dagger_\sigma(\vec{x},t)\hat{\Psi}_{\sigma_1}(\vec{x}_1,t_1)\right\rangle \delta_{\sigma,\sigma_1}\left\langle \hat{\mathrm{T}}\,\hat{\Psi}^\dagger_{\sigma_2}(\vec{x}_2,t_1)\hat{\Psi}_{\sigma_2}(\vec{x}_2,t_1)\right\rangle \times \\ &\times\left\langle \hat{\mathrm{T}}\,\hat{\Psi}_{\sigma_1}(\vec{x}_1,t)\hat{\Psi}^\dagger_\sigma(\vec{x}',t')\right\rangle \delta_{\sigma_1,\sigma} = \\ &= 2\delta_{\sigma,\sigma_1}\,\mathrm{i}\hbar\mathcal{G}_0^{\sigma,\sigma}(\vec{x},\vec{x}_1;t,t_1)\,(-\mathrm{i}\hbar)\mathcal{G}^<_{\sigma_2,\sigma_2}(\vec{x}_2,\vec{x}_2;t_1,t_1)\,\mathrm{i}\hbar\mathcal{G}_0^{\sigma,\sigma}(\vec{x}_1,\vec{x}';t_1,t'). \end{aligned} \tag{A.6}$$

This term is known as the Hartree term and the corresponding Feynman diagram has the structure:

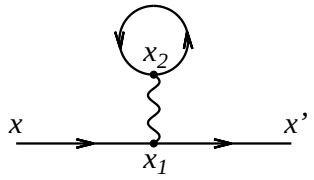

The second possible contraction gives the so-called Fock term

$$\begin{aligned} &-2\left\langle \hat{\mathrm{T}}\,\hat{\Psi}^\dagger_\sigma(\vec{x},t)\hat{\Psi}_{\sigma_1}(\vec{x}_1,t_1)\right\rangle \delta_{\sigma,\sigma_1}\left\langle \hat{\mathrm{T}}\,\hat{\Psi}^\dagger_{\sigma_2}(\vec{x}_2,t_1)\hat{\Psi}_{\sigma_1}(\vec{x}_1,t_1)\right\rangle \delta_{\sigma_2,\sigma_1}\times \\ &\times\left\langle \hat{\mathrm{T}}\,\hat{\Psi}_{\sigma_2}(\vec{x}_2,t)\hat{\Psi}^\dagger_\sigma(\vec{x}',t')\right\rangle \delta_{\sigma_2,\sigma} = \\ &= -2\delta_{\sigma,\sigma_1}\delta_{\sigma_1,\sigma_2}\,\mathrm{i}\hbar\mathcal{G}_0^{\sigma,\sigma}(\vec{x},\vec{x}_1;t,t_1)\,(-\mathrm{i}\hbar)\mathcal{G}^<_{\sigma,\sigma}(\vec{x}_1,\vec{x}_2;t_1,t_1)\,\mathrm{i}\hbar\mathcal{G}_0^{\sigma,\sigma}(\vec{x}_2,\vec{x}';t_1,t'), \end{aligned} \tag{A.7}$$

with a Feynman diagram

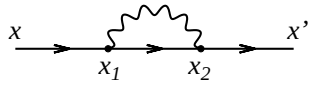

Inserting the Hartree- and Fock contribution into the first order expansion of the Green function, Eq. (A.2), we obtain after a Fourier transformation

$$\begin{aligned} &\mathcal{G}^{\sigma,\sigma}(\vec{x},\vec{x}';E) = \mathcal{G}_0^{\sigma,\sigma}(\vec{x},\vec{x}';E)\ + \\ &+\int \mathrm{d}^3x_1\int \mathrm{d}^3x_2\, w(\vec{x}_1,\vec{x}_2)\,\mathcal{G}_0^{\sigma,\sigma}(\vec{x},\vec{x}_1;E)\int\frac{\mathrm{d}E'}{2\pi\hbar}\sum_{\sigma_2}(-\mathrm{i}\hbar)\mathcal{G}^<_{\sigma_2,\sigma_2}(\vec{x}_2,\vec{x}_2;E')\,\mathcal{G}_0^{\sigma,\sigma}(\vec{x}_1,\vec{x}';E) \\ &-\int \mathrm{d}^3x_1\int \mathrm{d}^3x_2\, w(\vec{x}_1,\vec{x}_2)\,\mathcal{G}_0^{\sigma,\sigma}(\vec{x},\vec{x}_1;E)\int\frac{\mathrm{d}E'}{2\pi\hbar}(-\mathrm{i}\hbar)\mathcal{G}^<_{\sigma,\sigma}(\vec{x}_1,\vec{x}_2;E')\,\mathcal{G}_0^{\sigma,\sigma}(\vec{x}_2,\vec{x}';E). \end{aligned} \tag{A.8}$$

The additional energy integral over E' appears here, because the interaction is assumed to happen instantaneous in time. The above equation can be rewritten in a form similar to the Dyson equation

$$\begin{aligned}\mathcal{G}^{\sigma,\sigma}(\vec{x},\vec{x}';E) = \mathcal{G}_0^{\sigma,\sigma}(\vec{x},\vec{x}';E) + \\ + \int \mathrm{d}^3x_1 \int \mathrm{d}^3x_2\, \mathcal{G}_0^{\sigma,\sigma}(\vec{x},\vec{x}_1;E)\Sigma_{\mathrm{int}}^{\sigma}(\vec{x}_1,\vec{x}_2)\mathcal{G}_0^{\sigma,\sigma}(\vec{x}_2,\vec{x}';E),\end{aligned} \tag{A.9}$$

where the self-energy can be identified as

$$\begin{aligned}\Sigma_{\mathrm{int}}^{\sigma}(\vec{x}_1,\vec{x}_2) \;=\; & \int \frac{\mathrm{d}E'}{2\pi\hbar} \int \mathrm{d}^3x''\; w(\vec{x}_1,\vec{x}'') \sum_{\sigma_2} (-\mathrm{i}\hbar)\mathcal{G}^{<}_{\sigma_2,\sigma_2}(\vec{x}'',\vec{x}'';E')\,\delta(\vec{x}_1-\vec{x}_2) \\ & - \int \frac{\mathrm{d}E'}{2\pi\hbar}\; w(\vec{x}_1,\vec{x}_2)(-\mathrm{i}\hbar)\mathcal{G}^{<}_{\sigma,\sigma}(\vec{x}_1,\vec{x}_2;E').\end{aligned} \tag{A.10}$$

The first term is the Hartree self-energy $\Sigma_{\mathrm{int}}^{H}$, the second one the Fock self-energy $\Sigma_{\mathrm{int}}^{F}$. For the case of Coulomb interaction with $w(\vec{x}_1,\vec{x}_2) = e^2/(4\pi\varepsilon\varepsilon_0|\vec{x}_1-\vec{x}_2|)$ the Hartree self-energy corresponds to the classical Coulomb interaction

$$\Sigma_{\mathrm{int}}^{H}(\vec{x}_1,\vec{x}_2) = \delta(\vec{x}_1-\vec{x}_2)\,\frac{e^2}{4\pi\varepsilon\varepsilon_0}\int \mathrm{d}^3x''\frac{n(\vec{x}'')}{|\vec{x}_1-\vec{x}''|}, \tag{A.11}$$

where we inserted the particle density $n_\sigma(\vec{x}) = -\mathrm{i}/(2\pi)\int \mathrm{d}E'\mathcal{G}^{<}_{\sigma,\sigma}(\vec{x},\vec{x};E')$, according to Eq. (2.116), and $n(\vec{x}) = n_\uparrow(\vec{x}) + n_\downarrow(\vec{x})$ is the total electron density. The Hartree self-energy is diagonal and does not depend on the spin quantum number.

The expansion of the Dyson equation (2.46) in terms of powers of the self-energy reads

$$\mathcal{G} = \mathcal{G}_0 + \mathcal{G}_0\Sigma_{\mathrm{int}}\mathcal{G}_0 + \mathcal{G}_0\Sigma_{\mathrm{int}}\mathcal{G}_0\Sigma_{\mathrm{int}}\mathcal{G}_0 + \mathcal{G}_0\Sigma_{\mathrm{int}}\mathcal{G}_0\Sigma_{\mathrm{int}}\mathcal{G}_0\Sigma_{\mathrm{int}}\mathcal{G}_0 + \ldots, \tag{A.12}$$

where the spatial integrals were suppressed in our notation. Eq. (A.9) corresponds to the first two terms of the expansion (A.12). Hence, if we insert the Hartree-Fock self-energy, Eq. (A.10), into the Dyson equation we take into account multiple interaction events of Hartree-Fock type to infinite order. The Dyson equation with the same self-energy Σ_{int} also holds for the retarded Green function, see Eq. (2.54). Hence, if we determine the lesser Green function that enters the interaction self-energy self-consistently with the full retarded function, we end up with the so-called self-consistent Hartree-Fock approximation. The Dyson equation in terms of Feynman diagrams on that level of approximation reads

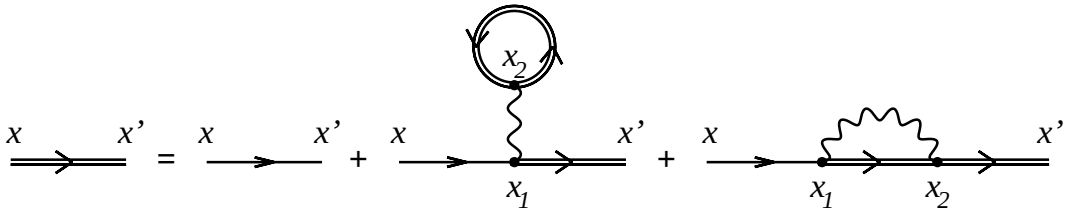

where a single line refers to the unperturbed Green function and a double line represents the full Green function.

For the case of delta-like interactions $w(\vec{x}_1, \vec{x}_2) = \gamma\delta(\vec{x}_1 - \vec{x}_2)$ the interaction self-energy simplifies to

$$\Sigma^{\sigma}_{\mathrm{int}}(\vec{x}_1, \vec{x}_2) = \gamma\delta(\vec{x}_1 - \vec{x}_2)\left[\sum_{\sigma_2} n_{\sigma_2}(\vec{x}_1) - n_{\sigma}(\vec{x}_1)\right]. \tag{A.13}$$

In that case the self-energy is diagonal and corresponds to a local potential $V^{\sigma}_{\mathrm{int}}(\vec{x}) = \Sigma^{\sigma}_{\mathrm{int}}(\vec{x}, \vec{x})$. The Fock term exactly compensates the $(\sigma_2 = \sigma)$-term of the Hartree contribution, and only the density of the opposite spins $-\sigma$ enters the final expression for the interaction potential,

$$V^{\sigma}_{\mathrm{int}}(\vec{x}) = \Sigma^{\sigma}_{\mathrm{int}}(\vec{x}, \vec{x}) = \gamma n_{-\sigma}(\vec{x}). \tag{A.14}$$

APPENDIX B

Green function of a semi-infinite lead

Here we show how to derive the Green function of a semi-infinite lead with width W, which starts at $x = 0$ and extends to $x = \infty$, as sketched in Fig. B.1. The transverse wave functions are given in Eq. (2.96) and accordingly the longitudinal lattice wave functions, which vanish at $x = 0$, are

$$\widetilde{\phi}_k(x) = \sqrt{\frac{2a}{L}} \sin kx, \tag{B.1}$$

with $k = n\pi/L$, $n \in \mathbb{N}$ and $L \to \infty$ being the length of the lead. Inserting the wave functions into Eq. (2.25) the Green function at the first slice $x = a$ reads

$$[g_0^r]_{i,j}(E) = g_0^r(a, z_i, a, z_j; E) = \frac{2a}{L} \sum_m \widetilde{\chi}_m(z_i) \widetilde{\chi}_m^*(z_j) \sum_k \frac{\sin^2 ka}{E - E_{mk} + \mathrm{i}\eta}, \tag{B.2}$$

with the energy dispersion, see Eq. (2.64),

$$E_{mk} = 2\kappa\Big(1 - \cos\frac{m\pi}{M+1}\Big) + 2\kappa\Big(1 - \cos ka\Big). \tag{B.3}$$

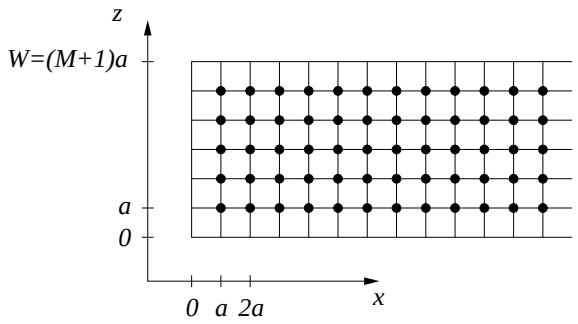

Figure B.1: The discretization of an isolated lead.

In the limit $L \to \infty$ one may replace the k-sum by an integral $(L/\pi)\int_0^{\pi/a} \mathrm{d}k$ and substitute $\vartheta = ak$ to find

$$[g_0^r]_{i,j}(E) = \frac{1}{\kappa\pi} \sum_m \widetilde{\chi}_m(z_i)\widetilde{\chi}_m^*(z_j) \int_0^\pi \mathrm{d}\vartheta \frac{\sin^2\vartheta}{Q + \cos\vartheta + \mathrm{i}\eta}, \tag{B.4}$$

with the abbreviation

$$Q = \frac{E}{2\kappa} - 2 + \cos\frac{m\pi}{M+1}. \tag{B.5}$$

The integrand is an even function of ϑ and hence Eq. (B.4) may be rewritten into a symmetric integral from $-\pi$ to π. Expressing the sine and cosine functions in the integral by exponentials and substituting $z = \exp(\mathrm{i}\vartheta)$, the integral turns into a closed contour integral along the unit circle in the complex plane

$$[g_0^r]_{i,j}(E) = \frac{1}{2\pi\mathrm{i}\kappa} \sum_m \widetilde{\chi}_m(z_i)\widetilde{\chi}_m^*(z_j) \oint_{|z|=1} \frac{1-z^2}{z^2 + 2zQ + 1}. \tag{B.6}$$

The resulting integral can be computed by the residual theorem, and we find

$$[g_0^r]_{i,j}(E) = \frac{1}{2\pi\mathrm{i}\kappa} \sum_m \widetilde{\chi}_m(z_i)\widetilde{\chi}_m^*(z_j) 2\pi\mathrm{i}\,\mathrm{Res}_{z_0} \frac{1-z^2}{z^2 + 2zQ + 1}. \tag{B.7}$$

The position of the pole z_0 depends on Q and is given by

$$z_0 = \begin{cases} -Q + \sqrt{Q^2-1} & \text{for } Q > 1 \\ -Q - \sqrt{Q^2-1} & \text{for } Q < -1 \\ -Q + \mathrm{i}\sqrt{1-Q^2} & \text{for } |Q| \le 1 \end{cases}. \tag{B.8}$$

Inserting the residual at z_0 we get as a final expression for the lead Green function

$$[g_0^r]_{i,j}(E) = \frac{1}{\kappa} \sum_{m=1}^{M} \widetilde{\chi}_m(z_i)\widetilde{\chi}_m(z_j) F(Q), \tag{B.9}$$

with

$$F(Q) = \begin{cases} Q - \sqrt{Q^2-1} & \text{for } Q > 1 \\ Q + \sqrt{Q^2-1} & \text{for } Q < -1 \\ Q - \mathrm{i}\sqrt{1-Q^2} & \text{for } |Q| \le 1. \end{cases} \tag{B.10}$$

APPENDIX C

Recursive Green function algorithm

The calculation of the retarded Green function with Eq. (2.95) requires the inversion of a large matrix. The typical number of lattice sites used in our calculations is of the order of 2000, so that due to the spin degree of freedom the matrices have the dimension of about 4000×4000. The direct inversion of a matrix of that size takes about 4:30 minutes on a Pentium4-2800 processor. Hence, the typical time to compute one single data point using 150 steps for the energy integral to get the particle density, Eq. (2.117), and 20 self-consistency loops would be more than 200 hours. However, due to the fact that the retarded Green function obeys the Dyson equation (2.100) it is possible to construct a recursive algorithm for noninteracting systems [24, 57]. This scheme can be extended to include interactions [58, 114], if the interaction potential is local, that means it affects only the diagonal elements of the effective Hamiltonian, which thus keeps its block-tridiagonal structure.

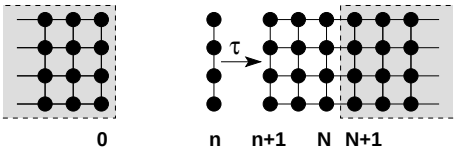

Figure C.1: The recursive strategy: the full Green function is calculated by adding one slice in each step.

The basic idea of the recursive algorithm is to build up the full Green function slice by slice as sketched in Fig. C.1, instead of evaluating it in one step. If the retarded Green function[1] $\mathcal{G}_0$ of a semi-infinite region and an adjacent *isolated* slice is known, it is possible to calculate the Green function $\mathcal{G}$ of the *coupled* system using Dyson's

[1] In this chapter we omit the superscript 'r' for the retarded function.

equation

$$\mathcal{G} = \mathcal{G}_0 + \mathcal{G}_0 \tau \mathcal{G}. \tag{C.1}$$

Here, the 'unperturbed' Green function $\mathcal{G}_0$ corresponds to the two isolated parts, $\mathcal{G}$ refers to the Green function of the coupled system, and the coupling matrix τ between two neighboring slices plays the role of the self-energy. For this step it is important that there is only nearest neighbor coupling involved. The Fock term of the Coulomb interaction, for instance, introduces long-range correlations as seen in Eq. (3.38), which makes the recursive scheme inapplicable.

Let us first see how to add one single slice to a semi-infinite region. In the following we use the notation $\mathcal{G}^{S(n)}$ for the Green function of an isolated slice n, and $\mathcal{G}^{R(n)}$ or $\mathcal{G}^{L(n)}$ for the Green function of the right or left semi-infinite region starting at slice n. The full Green function of the complete (infinite) system is denoted by $\mathcal{G}$ (without superscripts). In order to couple the Green function $\mathcal{G}^{S(n)}$ of the isolated slice n to the Green function $\mathcal{G}^{R(n+1)}$ that covers all lattice sites to the right of $(n+1)$, we use the Dyson equation (C.1) to obtain

$$\left\langle n \left| \mathcal{G}^{R(n)} \right| n \right\rangle = \left\langle n \left| \left(\mathcal{G}^{S(n)} + \mathcal{G}^{R(n+1)} \right) \right| n \right\rangle + \left\langle n \left| \left(\mathcal{G}^{S(n)} + \mathcal{G}^{R(n+1)} \right) \tau \mathcal{G}^{R(n)} \right| n \right\rangle .$$

The matrix element $\langle n|\mathcal{G}|m\rangle$ refers to the submatrix $\mathcal{G}_{i,j}$ with indices $i \in$ slice n and $j \in$ slice m. As $\mathcal{G}^{R(n+1)}$ has no matrix elements with slice n, the term $\langle n|\mathcal{G}^{R(n+1)}|n\rangle$ vanishes and we get

$$\left\langle n \left| \mathcal{G}^{R(n)} \right| n \right\rangle = \left\langle n \left| \mathcal{G}^{S(n)} \right| n \right\rangle + \sum_{a,b} \left\langle n \left| \mathcal{G}^{S(n)} \right| a \right\rangle \left\langle a \right| \tau \left| b \right\rangle \left\langle b \left| \mathcal{G}^{R(n)} \right| n \right\rangle .$$

Since $\mathcal{G}^{S(n)}$ is the Green function of the isolated slice n, its expectation value vanishes, if any slice different from n is involved. This leads to the constraint $a = n$. As the coupling matrix τ acts only between adjacent slices and has no overlap with other slices, b is restricted to the values $b = n \pm 1$. With $\langle n-1|\mathcal{G}^{R(n)}|n\rangle = 0$ we find

$$\mathcal{G}^{R(n)}_{n,n} = \mathcal{G}^{S(n)}_{n,n} + \mathcal{G}^{S(n)}_{n,n} \; \tau_{n,n+1} \; \mathcal{G}^{R(n)}_{n+1,n}, \tag{C.2}$$

where $\mathcal{G}_{n,m} = \langle n|\mathcal{G}|m\rangle$ is the sub-matrix of $\mathcal{G}$ related to the slices n and m. The Green function $\mathcal{G}^{R(n)}_{n+1,n}$ appearing in Eq. (C.2) can be calculated via the Dyson equation in a similar way, and we get

$$\mathcal{G}^{R(n)}_{n+1,n} = \mathcal{G}^{R(n+1)}_{n+1,n+1} \; \tau_{n+1,n} \; \mathcal{G}^{R(n)}_{n,n}.$$

Inserting this result into Eq. (C.2) and solving for $\mathcal{G}^{R(n)}_{n,n}$ we obtain

$$\mathcal{G}^{R(n)}_{n,n} = \left[(E - H_{n,n}) - \tau_{n,n+1} \; \mathcal{G}^{R(n+1)}_{n+1,n+1} \; \tau_{n+1,n} \right]^{-1}, \tag{C.3}$$

where we used $\mathcal{G}^{S(n)}_{n,n} = (E - H_{n,n})^{-1}$. Therefore, Eq. (C.3) allows us to calculate the Green function covering all lattice sites to the right of slice n from the Green function to the right of $(n+1)$. In that way we have added one slice, as depicted in Fig. C.1. Iterating this scheme we can finally obtain the Green function $\mathcal{G}^{R(1)}_{1,1}$ at the left end of the scattering region. Then one has to connect the Green functions of the two semi-infinite sections to get the full Green function $G_{1,1}$ (without superscript) at the left end of the scatterer. This we obtain by using the Dyson equation

$$\langle 1\,|\mathcal{G}|\,1\rangle = \left\langle 1\,\middle|\left(\mathcal{G}^{L(0)} + \mathcal{G}^{R(1)}\right)\middle|\,1\right\rangle + \left\langle 1\,\middle|\left(\mathcal{G}^{L(0)} + \mathcal{G}^{R(1)}\right)\tau\,\mathcal{G}\middle|\,1\right\rangle, \tag{C.4}$$

and we find

$$\mathcal{G}_{1,1} = \left[1 - \mathcal{G}^{R(1)}_{1,1}\tau_{1,0}\,\mathcal{G}^{L(0)}_{0,0}\,\tau_{0,1}\,\right]^{-1}\mathcal{G}^{R(1)}_{1,1}. \tag{C.5}$$

In this equation $\mathcal{G}^{L(0)}_{0,0}$ is the surface Green function of the semi-infinite left lead. The Green function $\mathcal{G}_{1,1}$ contains all information about the reflection coefficients at the left lead. Thus, the above described steps are sufficient in order to obtain the conductance or the current through a noninteracting system, as the total transmission is related to the reflection by unitarity and the transmission gives the conductance, Eq. (2.136), and the current, Eq. (2.146), by means of the Landauer formulas.

To include interaction effects one is interested in the evaluation of $\mathcal{G}^{<}$. If the interaction incorporates only the electron density, which is the case for a delta-like interaction potential in Hartree-Fock approximation or the Hartree part of the Coulomb interaction, it is sufficient to know only the diagonal matrix elements of $\mathcal{G}^{<}$. To do so, one has to repeat the above scheme from left to right to find

$$\mathcal{G}^{L(n)}_{n,n} = \left[(E - H_{n,n}) - \tau_{n,n-1}\,\mathcal{G}^{L(n-1)}_{n-1,n-1}\,\tau_{n-1,n}\right]^{-1}, \tag{C.6}$$

and finally obtain the full Green function at the right end of the scatterer,

$$\mathcal{G}_{N,N} = \left[1 - \mathcal{G}^{L(N)}_{N,N}\,\tau_{N,N+1}\,\mathcal{G}^{R(N+1)}_{N+1,N+1}\,\tau_{N+1,N}\right]^{-1}\mathcal{G}^{L(N)}_{N,N}. \tag{C.7}$$

Here $\mathcal{G}^{R(N+1)}_{N+1,N+1}$ is the surface Green function of the right lead.

Knowing the full Green functions at both ends of the scatterer, $\mathcal{G}_{1,1}$ and $\mathcal{G}_{N,N}$, we can now compute the full Green functions between the ends and any slice n inside the scattering region. We use the Dyson equation

$$\langle n\,|\mathcal{G}|\,1\rangle = \left\langle n\,\middle|\left(\mathcal{G}^{L(n-1)} + \mathcal{G}^{R(n)}\right)\middle|\,1\right\rangle + \left\langle n\,\middle|\left(\mathcal{G}^{L(n-1)} + \mathcal{G}^{R(n)}\right)\tau\mathcal{G}\middle|\,1\right\rangle$$

to obtain

$$\mathcal{G}_{n,1} = \mathcal{G}^{R(n)}_{n,n}\,\tau_{n,n-1}\,\mathcal{G}_{n-1,1}, \tag{C.8}$$

where the $\mathcal{G}^{R(n)}_{n,n}$ are calculated from Eq. (C.3). Analogously one finds

$$\mathcal{G}_{n,N} = \mathcal{G}^{L(n)}_{n,n}\, \tau_{n,n+1}\, \mathcal{G}_{n+1,N} \tag{C.9}$$

with the Green functions $\mathcal{G}^{L(n)}_{n,n}$ from Eq. (C.6). The last two equations allow us to compute the Green functions $\mathcal{G}_{n,1}$ and $\mathcal{G}_{n,N}$ recursively by starting with the Green functions $\mathcal{G}_{1,1}$ and $\mathcal{G}_{N,N}$ at the ends of the scattering region.

Now it is possible to compute the diagonal elements of the lesser Green function which are needed to calculate the electron density, Eq. (2.116). A diagonal matrix element of $\mathcal{G}^<$ reads according to Eq. (2.101)

$$[\mathcal{G}^<]_{x,x} = \sum_{i,j} [\mathcal{G}]_{x,i}\, [\Sigma^<]_{i,j}\, [\mathcal{G}]^*_{x,j} \tag{C.10}$$

with $i, j \in \{n = 1, n = N\}$. The self-energy $\Sigma^<$ is only non-zero at the ends of the scatterer where the lattice sites are coupled to the leads. So the indices i and j are from the first and last slice of the scattering region. Therefore, the Green functions calculated from Eqs. (C.8) and (C.9) enter here.

The complete recursive procedure can be summarized in the following steps:

① calculate and store all $\mathcal{G}^{R(n)}_{n,n}$ from the lead Green function $\mathcal{G}^{R(N+1)}_{N+1,N+1}$ by means of Eq. (C.3);

② calculate and store all $\mathcal{G}^{L(n)}_{n,n}$ from the lead Green function $\mathcal{G}^{L(0)}_{0,0}$ by means of Eq. (C.6);

③ compute the full Green functions $\mathcal{G}_{1,1}$ and $\mathcal{G}_{N,N}$ at the left and right end of the scatterer using Eqs. (C.5) and (C.7);

④ use Eqs. (C.8) and (C.9) to calculate and store all $\mathcal{G}_{n,1}$ and $\mathcal{G}_{n,N}$ from $\mathcal{G}_{1,1}$ and $\mathcal{G}_{N,N}$. One of those Green functions is $\mathcal{G}_{N,1}$ which contains information about the transport properties;

⑤ finally, one obtains the diagonal elements of $\mathcal{G}^<$ from $\mathcal{G}_{n,1}$ and $\mathcal{G}_{n,N}$ by means of Eq. (C.10).

In total, one has to run four times through the entire system in order to be able to calculate the diagonal elements of $\mathcal{G}^<$ as well as parts of $\mathcal{G}^r$ which are needed for the reflection and transmission coefficients. If the calculation of $\mathcal{G}^<$ is not necessary it is enough to pass the system twice to get all reflection and transmission coefficients. So the scheme reduces to the standard recursive algorithm [24, 57]. If one is only interested in the current, one can stop the procedure after computing $\mathcal{G}_{1,1}$ with Eq. (C.5), which gives the total reflection. Employing current conservation (unitarity) it is possible to get the total transmission and hence the current.

References

[1] G. E. Moore, *Cramming more components onto integrated circuits*, Electronics **38**, 114 (1965)

[2] L. L. Sohn, *Nanotechnology: A quantum leap for electronics*, Nature **394**, 131 (1998)

[3] G. Cuniberti, G. Fagas, K. Richter (Editors), *Introducing Molecular Electronics* (Springer-Verlag, Berlin, 2005)

[4] T. Heinzel, *Mesoscopic Electronics in Solid State Nanostructures* (Wiley-VCH, 2003)

[5] M. A. Topinka, B. J. LeRoy, R. M. Westervelt, S. E. J. Shaw, R. Fleischmann, E. J. Heller, K. D. Maranowski, A. C. Gossard, *Coherent branched flow in a two-dimensional electron gas*, Nature **410**, 183 (2001)

[6] B. J. van Wees, H. van Houten, C. W. J. Beenakker, J. G. Williamson, L. P. Kouwenhoven, D. van der Marel, C. T. Foxon, *Quantized conductance of point contacts in a two-dimensional electron gas*, Phys. Rev. Lett. **60**, 848 (1988)

[7] D. A. Wharam, T. J. Thornton, R. Newbury, M. Pepper, H. Ahmed, J. E. F. Frost, D. G. Hasko, D. C. Peacock, D. A. Ritchie, G. A. C. Jones, *One-dimensional transport and the quantisation of the ballistic resistance*, J. Phys. C **21**, L209 (1988)

[8] M. J. Berry, J. A. Katine, C. M. Marcus, R. M. Westervelt, A. C. Gossard, *Weak localization and conductance fluctuations in a chaotic quantum dot*, Surf. Sci. **305**, 495 (1994)

[9] S. A. Wolf, D. D. Awschalom, R. A. Buhrman, J. M. Daughton, S. von Molnár, M. L. Roukes, A. Y. Chtchelkanova, D. M. Treger, *Spintronics: A Spin-Based Electronics Vision for the Future*, Science **294**, 1488 (2001)

[10] I. Žutić, J. Fabian, S. D. Sarma, *Spintronics: Fundamentals and applications*, Rev. Mod. Phys. **76**, 323 (2004)

[11] J. Fabian, A. Matos-Abiague, C. Ertler, P. Stano, I. Žutić, *Semiconductor Spintronics*, Acta Phys. Slov. **57**, 565 (2007)

[12] M. N. Baibich, J. M. Broto, A. Fert, F. N. Van Dau, F. Petroff, P. Eitenne, G. Creuzet, A. Friederich, J. Chazelas, *Giant Magnetoresistance of (001)Fe/(001)Cr Magnetic Superlattices*, Phys. Rev. Lett. **61**, 2472 (1988)

[13] J. Barnaś, A. Fuss, R. E. Camley, P. Grünberg, W. Zinn, *Novel magnetoresistance effect in layered magnetic structures: Theory and experiment*, Phys. Rev. B **42**, 8110 (1990)

[14] S. Datta, B. Das, *Electronic analog of the electro-optic modulator*, Appl. Phys. Lett. **56**, 665 (1990)

[15] E. I. Rashba, *Properties of semiconductors with an extremum loop: I. Cyclotron and combinational resonance in a magnetic field perpendicular to the plane of the loop*, Sov. Phys. Solid State **2**, 1109 (1960), [Fiz. Tverd. Tela (Leningrad) **2**, 1224 (1960)]

[16] G. Dresselhaus, *Spin-Orbit Coupling Effects in Zinc Blende Structures*, Phys. Rev. **100**, 580 (1955)

[17] G. Schmidt, D. Ferrand, L. W. Molenkamp, A. T. Filip, B. J. van Wees, *Fundamental obstacle for electrical spin injection from a ferromagnetic metal into a diffusive semiconductor*, Phys. Rev. B **62**, R4790 (2000)

[18] G. Burkard, H.-A. Engel, D. Loss, *Spintronics and Quantum Dots for Quantum Computing and Quantum Communication*, Fortschr. Phys. **48**, 965 (2000)

[19] S. Harris, *An Introduction to the Theory of the Boltzmann Equation* (Dover Publications, Inc., New York, 2004)

[20] H. U. Baranger, R. A. Jalabert, A. D. Stone, *Quantum-chaotic scattering effects in semiconductor microstructures*, Chaos **3**, 665 (1993)

[21] K. Richter, M. Sieber, *Semiclassical Theory of Chaotic Quantum Transport*, Phys. Rev. Lett. **89**, 206801 (2002)

[22] K. F. H. Bruus, *Many-Body Quantum Theory in Condensed Matter Physics* (Oxford University Press, 2004)

[23] S. Datta, *Electronic transport in mesoscopic systems* (Cambridge University Press, 1995)

[24] D. K. Ferry, S. M. Goodnick, *Transport in Nanostructures* (Cambridge University Press, 1997)

[25] H. Haug, A.-P. Jauho, *Quantum Kinetics in Transport and Optics of Semiconductors* (Springer, Berlin, 1996)

[26] A. M. Zagoskin, *Quantum Theory of Many-Body Systems: Techniques and Applications* (Springer, New York, 1998)

[27] G. D. Mahan, *Many-Particle Physics* (Kluwer Academic/Plenum Publishers, New York, 2000)

[28] A. L. Fetter, J. D. Walecka, *Quantum Theory of Many-Particle Physics* (McGraw-Hill, New York, 1971)

[29] J. Rammer, H. Smith, *Quantum field-theoretical methods in transport theory of metals*, Rev. Mod. Phys. **58**, 323 (1986)

[30] S. Datta, *Nanoscale device modeling: the Green's function method*, Superlattices and Microstructures **28**, 253 (2000)

[31] Y. Xue, S. Datta, M. A. Ratner, *First-principles based matrix Green's function approach to molecular electronic devices: general formalism*, Chem. Phys. **281**, 151 (2002)

[32] R. Landauer, *Spatial Variation of Currents and Fields Due to Localized Scatterers in Metallic Conduction*, IBM J. Res. Dev. **1**, 223 (1957)

[33] R. Landauer, *Electrical resistance of disordered one-dimensional lattices*, Phil. Mag. **21**, 863 (1970)

[34] D. S. Fisher, P. A. Lee, *Relation between conductivity and transmission matrix*, Phys. Rev. B **23**, 6851 (1981)

[35] C. W. J. Beenakker, H. van Houten, *Quantum Transport in Semiconductor Nanostructures*, Solid State Phys. **44**, 1 (1991), [arXiv:cond-mat/0412664v1]

[36] S. E. Laux, D. J. Frank, F. Stern, *Quasi-one-dimensional electron states in a split-gate GaAs/AlGaAs heterostructure*, Surf. Sci. **196**, 101 (1988)

[37] K. J. Thomas, J. T. Nicholls, M. Y. Simmons, M. Pepper, D. R. Mace, D. A. Ritchie, *Possible Spin Polarization in a One-Dimensional Electron Gas*, Phys. Rev. Lett. **77**, 135 (1996)

[38] H. Linke, W. Sheng, A. Löfgren, H. Xu, P. Omling, P. E. Lindelof, *A quantum dot ratchet: Experiment and theory*, Europhys. Lett. **44**, 341 (1998), *Erratum:* Europhys. Lett. **44**, 406 (1999)

[39] H. Linke, W. D. Sheng, A. Svensson, A. Löfgren, L. Christensson, H. Q. Xu, P. Omling, P. E. Lindelof, *Asymmetric nonlinear conductance of quantum dots with broken inversion symmetry*, Phys. Rev. B **61**, 15914 (2000)

[40] H. Linke, T. E. Humphrey, A. Löfgren, A. O. Sushkov, R. Newbury, R. P. Taylor, P. Omling, *Experimental Tunneling Ratchets*, Science **286**, 2314 (1999)

[41] A. Pfund, *A ratchet mechanism for directed spin transport in nanostructures*, Master thesis (Uni Regensburg, 2005)

[42] M. Strehl, *Coherent spin ratchets – transport and noise properties*, Master thesis (Uni Regensburg, 2007)

[43] M. Scheid, A. Pfund, D. Bercioux, K. Richter, *Coherent Spin Ratchets*, Phys. Rev. B, in press (2007), [arXiv:cond-mat/0601118v2]

[44] M. Scheid, *Directed quantum transport in non-uniform magnetic fields*, Master thesis (Uni Regensburg, 2006)

[45] M. Scheid, M. Wimmer, D. Bercioux, K. Richter, *Zeeman ratchets for ballistic spin currents*, Phys. Stat. Sol. (C) **3**, 4235 (2006)

[46] M. Scheid, D. Bercioux, K. Richter, *Zeeman ratchets: Rectification of spin current via magnetic fields*, New J. Phys., in press (2007), [arXiv:0707.2478v1]

[47] E. R. Mucciolo, C. Chamon, C. M. Marcus, *Adiabatic Quantum Pump of Spin-Polarized Current*, Phys. Rev. Lett. **89**, 146802 (2002)

[48] S. K. Watson, R. M. Potok, C. M. Marcus, V. Umansky, *Experimental Realization of a Quantum Spin Pump*, Phys. Rev. Lett. **91**, 258301 (2003)

[49] M. Gell-Mann, F. Low, *Bound States in Quantum Field Theory*, Phys. Rev. **84**, 350 (1951)

[50] G. C. Wick, *The Evaluation of the Collision Matrix*, Phys. Rev. **80**, 268 (1950)

[51] A. Anthore, F. Pierre, H. Pothier, D. Esteve, *Magnetic-Field-Dependent Quasiparticle Energy Relaxation in Mesoscopic Wires*, Phys. Rev. Lett. **90**, 076806 (2003)

[52] L. V. Keldysh, *Diagram Technique for Nonequilibrium Processes*, Sov. Phys. JETP **20**, 1018 (1965), [Zh. Eksp. Teor. Fiz. **47**, 1515 (1964)]

[53] L. P. Kadanoff, G. Baym, *Quantum Statistical Mechanics* (W. A. Benjamin, Inc. New York, 1962)

[54] J. H. Davies, S. Hershfield, P. Hyldgaard, J. W. Wilkins, *Current and rate equation for resonant tunneling*, Phys. Rev. B **47**, 4603 (1993)

[55] D. Frustaglia, M. Hentschel, K. Richter, *Aharonov-Bohm physics with spin. II. Spin-flip effects in two-dimensional ballistic systems*, Phys. Rev. B **69**, 155327 (2004)

[56] R. Peierls, *Zur Theorie des Diamagnetismus von Leitungselektronen*, Z. Phys. **80**, 763 (1933)

[57] M. Macucci, A. Galick, U. Ravaioli, *Quasi-three-dimensional Green's-function simulation of coupled electron waveguides*, Phys. Rev. B **52**, 5210 (1995)

[58] R. Lake, G. Klimeck, R. C. Bowen, D. Jovanovic, *Single and multiband modeling of quantum electron transport through layered semiconductor devices*, J. Appl. Phys. **81**, 7845 (1997)

[59] A. R. Williams, P. J. Feibelman, N. D. Lang, *Green's-function methods for electronic-structure calculations*, Phys. Rev. B **26**, 5433 (1982)

[60] R. Zeller, J. Deutz, P. H. Dederichs, *Application of complex energy integration to self-consistent electronic structure calculations*, Sol. State Comm. **44**, 993 (1982)

[61] J. Taylor, H. Guo, J. Wang, *Ab initio modeling of quantum transport properties of molecular electronic devices*, Phys. Rev. B **63**, 245407 (2001)

[62] M. Brandbyge, J.-L. Mozos, P. Ordejón, J. Taylor, K. Stokbro, *Density-functional method for nonequilibrium electron transport*, Phys. Rev. B **65**, 165401 (2002)

[63] W. H. Press, S. A. Teukolsky, W. T. Vetterling, B. P. Flannery, *Numerical Recipes in C++* (Cambridge University Press, 2002)

[64] Y. Meir, N. S. Wingreen, *Landauer formula for the current through an interacting electron region*, Phys. Rev. Lett. **68**, 2512 (1992)

[65] A. Khurana, *Ballistic electron transport through a narrow channel is quantized*, Phys. Today **41**(11), 21 (1988)

[66] K. J. Thomas, J. T. Nicholls, N. J. Appleyard, M. Y. Simmons, M. Pepper, D. R. Mace, W. R. Tribe, D. A. Ritchie, *Interaction effects in a one-dimensional constriction*, Phys. Rev. B **58**, 4846 (1998)

[67] C.-T. Liang, M. Y. Simmons, C. G. Smith, G. H. Kim, D. A. Ritchie, M. Pepper, *Spin-dependent transport in a clean one-dimensional channel*, Phys. Rev. B **60**, 10687 (1999)

[68] K. J. Thomas, J. T. Nicholls, M. Pepper, W. R. Tribe, M. Y. Simmons, D. A. Ritchie, *Spin properties of low-density one-dimensional wires*, Phys. Rev. B **61**, R13365 (2000)

[69] A. Kristensen, H. Bruus, A. E. Hansen, J. B. Jensen, P. E. Lindelof, C. J. Marckmann, J. Nygård, C. B. Sørensen, F. Beuscher, A. Forchel, M. Michel, *Bias and temperature dependence of the 0.7 conductance anomaly in quantum point contacts*, Phys. Rev. B **62**, 10950 (2000)

[70] S. Nuttinck, K. Hashimoto, S. Miyashita, T. Saku, Y. Yamamoto, Y. Hirayama, *Quantum point contacts in a density-tunable two-dimensional electron gas*, Jpn. J. Appl. Phys. **39**, L655 (2000)

[71] D. J. Reilly, G. R. Facer, A. S. Dzurak, B. E. Kane, R. G. Clark, P. J. Stiles, R. G. Clark, A. R. Hamilton, J. L. O'Brien, N. E. Lumpkin, L. N. Pfeiffer, K. W. West, *Many-body spin-related phenomena in ultra low-disorder quantum wires*, Phys. Rev. B **63**, 121311 (2001)

[72] D. J. Reilly, T. M. Buehler, J. L. O'Brien, A. R. Hamilton, A. S. Dzurak, R. G. Clark, B. E. Kane, L. N. Pfeiffer, K. W. West, *Density-Dependent Spin Polarization in Ultra-Low-Disorder Quantum Wires*, Phys. Rev. Lett. **89**, 246801 (2002)

[73] A. C. Graham, M. Pepper, M. Y. Simmons, D. A. Ritchie, *Anomalous spin-dependent behavior of one-dimensional subbands*, Phys. Rev. B **72**, 193305 (2005)

[74] S. M. Cronenwett, H. J. Lynch, D. Goldhaber-Gordon, L. P. Kouwenhoven, C. M. Marcus, K. Hirose, N. S. Wingreen, V. Umansky, *Low-Temperature Fate of the 0.7 Structure in a Point Contact: A Kondo-like Correlated State in an Open System*, Phys. Rev. Lett. **88**, 226805 (2002)

[75] L. P. Rokhinson, L. N. Pfeiffer, K. W. West, *Spontaneous Spin Polarization in Quantum Point Contacts*, Phys. Rev. Lett. **96**, 156602 (2006)

[76] P. Roche, J. Segala, D. C. Glattli, J. T. Nicholls, M. Pepper, A. C. Graham, K. J. Thomas, M. Y. Simmons, D. A. Ritchie, *Fano Factor Reduction on the 0.7 Conductance Structure of a Ballistic One-Dimensional Wire*, Phys. Rev. Lett. **93**, 116602 (2004)

[77] L. DiCarlo, Y. Zhang, D. T. McClure, D. J. Reilly, C. M. Marcus, L. N. Pfeiffer, K. W. West, *Shot-Noise Signatures of 0.7 Structure and Spin in a Quantum Point Contact*, Phys. Rev. Lett. **97**, 036810 (2006)

[78] L. DiCarlo, Y. Zhang, D. T. McClure, D. J. Reilly, C. M. Marcus, L. N. Pfeiffer, K. W. West, M. P. Hanson, A. C. Gossard, *Current Noise in Quantum Point Contacts*, arXiv:0704.3892v1 (2007)

[79] A. C. Graham, K. J. Thomas, M. Pepper, N. R. Cooper, M. Y. Simmons, D. A. Ritchie, *Interaction Effects at Crossings of Spin-Polarized One-Dimensional Subbands*, Phys. Rev. Lett. **91**, 136404 (2003)

[80] A. C. Graham, K. J. Thomas, M. Pepper, M. Y. Simmons, D. A. Ritchie, *0.7 Structure in quantum wires observed at crossings of spin-polarised 1D subbands*, Physica E **22**, 264 (2004)

[81] A. C. Graham, K. J. Thomas, M. Pepper, M. Y. Simmons, D. A. Ritchie, K.-F. Berggren, P. Jaksch, A. Debnarova, I. I. Yakimenko, *0.7 Analogue structures and exchange interactions in quantum wires*, Sol. State Comm. **131**, 591 (2004)

[82] A. C. Graham, D. L. Sawkey, M. Pepper, M. Y. Simmons, D. A. Ritchie, *Energy-level pinning and the 0.7 spin state in one dimension: GaAs quantum wires studied using finite-bias spectroscopy*, Phys. Rev. B **75**, 035331 (2007)

[83] A. C. Graham, T.-M. Chen, I. Farrer, D. A. Ritchie, M. Pepper, *The origin of the 'zero-bias anomaly' in quantum wires*, to be published (2007)

[84] T.-M. Chen, A. C. Graham, M. Pepper, I. Farrer, D. A. Ritchie, *Spin phase transitions in a one-dimensional electron system*, to be published (2007)

[85] C.-K. Wang, K.-F. Berggren, *Spin splitting of subbands in quasi-one-dimensional electron quantum channels*, Phys. Rev. B **54**, R14257 (1996)

[86] C.-K. Wang, K.-F. Berggren, *Local spin polarization in ballistic quantum point contacts*, Phys. Rev. B **57**, 4552 (1998)

[87] C.-K. Wang, K.-F. Berggren, *Spontaneous spin polarization in quantum wires*, Physica E **2**, 964 (1998)

[88] A. M. Bychkov, I. I. Yakimenko, K.-F. Berggren, *Spin-dependent electron behaviour in quantum point contacts*, Nanotechnology **11**, 318 (2000)

[89] K.-F. Berggren, I. I. Yakimenko, *Effects of exchange and electron correlation on conductance and nanomagnetism in ballistic semiconductor quantum point contacts*, Phys. Rev. B **66**, 085323 (2002)

[90] A. A. Starikov, I. I. Yakimenko, K.-F. Berggren, *Scenario for the 0.7-conductance anomaly in quantum point contacts*, Phys. Rev. B **67**, 235319 (2003)

[91] P. Havu, M. J. Puska, R. M. Nieminen, V. Havu, *Electron transport through quantum wires and point contacts*, Phys. Rev. B **70**, 233308 (2004)

[92] K.-F. Berggren, P. Jaksch, I. Yakimenko, *Effects of electron interactions at crossings of Zeeman-split subbands in quantum wires*, Phys. Rev. B **71**, 115303 (2005)

[93] A. Ashok, R. Akis, D. Vasileska, D. K. Ferry, *Theoretical Evidence of Spontaneous Spin Polarization in GaAs/AlGaAs Split-Gate Heterostructures*, J. Comp. Electronics **4**, 125 (2005)

[94] K.-F. Berggren, *Dimensional Crossover in Semiconductor Structures: From 3D Electron Transport to Ballistic Electrons in 1D*, Turk. J. Phys **30**, 197 (2006)

[95] P. Jaksch, I. Yakimenko, K.-F. Berggren, *From quantum point contacts to quantum wires: Density-functional calculations with exchange and correlation effects*, Phys. Rev. B **74**, 235320 (2006)

[96] A. M. Bychkov, T. M. Stace, *0.4 and 0.7 conductance anomalies in quantum point contacts*, Nanotechnology **18**, 185403 (2007)

[97] Y. Meir, K. Hirose, N. S. Wingreen, *Kondo Model for the "0.7 Anomaly" in Transport through a Quantum Point Contact*, Phys. Rev. Lett. **89**, 196802 (2002)

[98] K. Hirose, Y. Meir, N. S. Wingreen, *Local Moment Formation in Quantum Point Contacts*, Phys. Rev. Lett. **90**, 026804 (2003)

[99] T. Rejec, Y. Meir, *Magnetic impurity formation in quantum point contacts*, Nature **442**, 900 (2006)

[100] A. Golub, T. Aono, Y. Meir, *Suppression of Shot Noise in Quantum Point Contacts in the "0.7 Regime"*, Phys. Rev. Lett. **97**, 186801 (2006)

[101] H. Bruus, V. V. Cheianov, K. Flensberg, *The anomalous 0.5 and 0.7 conductance plateaus in quantum point contacts*, Physica E **10**, 97 (2001)

[102] D. J. Reilly, *Phenomenological model for the 0.7 conductance feature in quantum wires*, Phys. Rev. B **72**, 033309 (2005)

[103] D. J. Reilly, Y. Zhang, L. DiCarlo, *Phenomenology of the 0.7 conductance feature*, Physica E **34**, 27 (2006)

[104] G. Seelig, K. A. Matveev, *Electron-Phonon Scattering in Quantum Point Contacts*, Phys. Rev. Lett. **90**, 176804 (2003)

[105] P. S. Cornaglia, C. A. Balseiro, *On the magnetic nature of quantum point contacts*, Europhys. Lett. **67**, 634 (2004)

[106] P. S. Cornaglia, C. A. Balseiro, M. Avignon, *Magnetic moment formation in quantum point contacts*, Phys. Rev. B **71**, 024432 (2005)

[107] B. Spivak, F. Zhou, *Ferromagnetic correlations in quasi-one-dimensional conducting channels*, Phys. Rev. B **61**, 16730 (2000)

[108] K. A. Matveev, *Conductance of a Quantum Wire in the Wigner-Crystal Regime*, Phys. Rev. Lett. **92**, 106801 (2004)

[109] A. D. Klironomos, J. S. Meyer, K. A. Matveev, *Spontaneous spin polarization in quantum wires*, Europhys. Lett. **74**, 679 (2006)

[110] O. F. Syljuåsen, *Length-Dependent Conductance of a Spin-Incoherent Hubbard Chain: Monte Carlo Calculations*, Phys. Rev. Lett. **98**, 166401 (2007)

[111] V. V. Flambaum, M. Y. Kuchiev, *Possible mechanism of the fractional-conductance quantization in a one-dimensional constriction*, Phys. Rev. B **61**, R7869 (2000)

[112] C. Sloggett, A. I. Milstein, O. P. Sushkov, *Correlated electron current and temperature dependence of the conductance of a quantum point contact*, arXiv:cond-mat/0606649v2 (2006)

[113] A. M. Lunde, A. De Martino, R. Egger, K. Flensberg, *Electron-electron interaction effects in quantum point contacts*, arXiv:0707.1989v1 (2007)

[114] A. Lassl, P. Schlagheck, K. Richter, *Effects of short-range interactions on transport through quantum point contacts: A numerical approach*, Phys. Rev. B **75**, 045346 (2007)

[115] S. Ihnatsenka, I. V. Zozoulenko, *Conductance of a quantum point contact based on spin-density-functional theory*, Phys. Rev. B **76**, 045338 (2007)

[116] S. Ihnatsenka, I. V. Zozoulenko, *"0.7 anomaly" and magnetic impurity formation in quantum point contacts*, arXiv:cond-mat/0701657v1 (2007)

[117] R. Fitzgerald, *Quantum Point Contact Mysteries Reexamined*, Phys. Today **55**(5), 21 (2002)

[118] G. Grüner, A. Zawadowski, *Magnetic impurities in non-magnetic metals*, Rep. Prog. Phys. **37**, 1497 (1974)

[119] D. Goldhaber-Gordon, H. Shtrikman, D. Mahalu, D. Abusch-Magder, U. Meirav, M. A. Kastner, *Kondo effect in a single-electron transistor*, Nature **391**, 156 (1998)

[120] P. W. Anderson, *Localized Magnetic States in Metals*, Phys. Rev. **124**, 41 (1961)

[121] T. Ando, A. B. Fowler, F. Stern, *Electronic properties of two-dimensional systems*, Rev. Mod. Phys. **54**, 437 (1982), *note*: the authors are using cgs-units.

[122] O. Madelung (Editor), *Semiconductors – Basic Data* (Springer Berlin-Heidelberg, 1996)

[123] Y. M. Blanter, M. Büttiker, *Shot noise in mesoscopic conductors*, Phys. Rep. **336**, 1 (2000)

[124] Private communication with M. Grifoni

[125] E. Lieb, D. Mattis, *Theory of Ferromagnetism and the Ordering of Electronic Energy Levels*, Phys. Rev. **125**, 164 (1962)

[126] S. Daul, R. M. Noack, *Ferromagnetic transition and phase diagram of the one-dimensional Hubbard model with next-nearest-neighbor hopping*, Phys. Rev. B **58**, 2635 (1998)

[127] A. J. Leggett, *Bose-Einstein condensation in the alkali gases: Some fundamental concepts*, Rev. Mod. Phys. **73**, 307 (2001)

[128] T. Paul, P. Leboeuf, N. Pavloff, K. Richter, P. Schlagheck, *Nonlinear transport of Bose-Einstein condensates through waveguides with disorder*, Phys. Rev. A **72**, 063621 (2005)

[129] T. Paul, K. Richter, P. Schlagheck, *Nonlinear Resonant Transport of Bose-Einstein Condensates*, Phys. Rev. Lett. **94**, 020404 (2005)

[130] M. W. Zwierlein, J. R. Abo-Shaeer, A. Schirotzek, C. H. Schunck, W. Ketterle, *Vortices and superfluidity in a strongly interacting Fermi gas*, Nature **435**, 1047 (2005)

[131] D. S. Petrov, M. Holzmann, G. V. Shlyapnikov, *Bose-Einstein Condensation in Quasi-2D Trapped Gases*, Phys. Rev. Lett. **84**, 2551 (2000)

[132] S. Jochim, M. Bartenstein, A. Altmeyer, G. Hendl, S. Riedl, C. Chin, J. Hecker Denschlag, R. Grimm, *Bose-Einstein Condensation of Molecules*, Science **302**, 2101 (2003)

[133] J. H. Thywissen, R. M. Westervelt, M. Prentiss, *Quantum Point Contacts for Neutral Atoms*, Phys. Rev. Lett. **83**, 3762 (1999)

[134] E. Castaño, G. Kirczenow, *Theory of nonlinear transport in narrow ballistic constrictions*, Phys. Rev. B **41**, 3874 (1990)

[135] H. Xu, *Theory of nonlinear ballistic transport in quasi-one-dimensional constrictions*, Phys. Rev. B **47**, 15630 (1993)

[136] M. J. McLennan, Y. Lee, S. Datta, *Voltage drop in mesoscopic systems: A numerical study using a quantum kinetic equation*, Phys. Rev. B **43**, 13846 (1991)

[137] V. A. Sablikov, B. S. Shchamkhalova, *Electron transport in a quantum wire with realistic Coulomb interaction*, Phys. Rev. B **58**, 13847 (1998)

[138] V. Mujica, A. E. Roitberg, M. Ratner, *Molecular wire conductance: Electrostatic potential spatial profile*, J. Chem. Phys. **112**, 6834 (2000)

[139] A. Nitzan, M. Galperin, G.-L. Ingold, H. Grabert, *On the electrostatic potential profile in biased molecular wires*, J. Chem. Phys. **117**, 10837 (2002)

[140] S. Pleutin, H. Grabert, G.-L. Ingold, A. Nitzan, *The electrostatic potential profile along a biased molecular wire: A model quantum-mechanical calculation*, J. Chem. Phys. **118**, 3756 (2003)

[141] A. Trellakis, A. T. Galick, A. Pacelli, U. Ravaioli, *Iteration scheme for the solution of the two-dimensional Schrödinger-Poisson equations in quantum structures*, J. Appl. Phys. **81**, 7880 (1997)

[142] J. H. Davies, I. A. Larkin, E. V. Sukhorukov, *Modeling the patterned two-dimensional electron gas: Electrostatics*, J. Appl. Phys. **77**, 4504 (1995)

[143] P. L. Pernas, A. Martin-Rodero, F. Flores, *Electrochemical-potential variations across a constriction*, Phys. Rev. B **41**, 8553 (1990)

[144] G. C. Liang, A. W. Ghosh, M. Paulsson, S. Datta, *Electrostatic potential profiles of molecular conductors*, Phys. Rev. B **69**, 115302 (2004)

[145] B. S. Shchamkhalova, V. A. Sablikov, *Potential landscape of a biased quantum wire*, Physica E **27**, 51 (2005)

[146] P. Reimann, *Brownian motors: noisy transport far from equilibrium*, Phys. Rep. **361**, 57 (2002)

[147] R. D. Astumian, *Thermodynamics and Kinetics of a Brownian Motor*, Science **276**, 917 (1997)

[148] R. D. Astumian, P. Hänggi, *Brownian Motors*, Phys. Today **55**(11), 33 (2002)

[149] R. P. Feynman, R. B. Leighton, M. Sands, *The Feynman Lectures on Physics, Vol. 1* (Addison-Wesley, Reading, 1963)

[150] http://www.physik.uni-bielefeld.de/theory/cm/research/projects/ratchet.html

[151] P. Reimann, M. Grifoni, P. Hänggi, *Quantum Ratchets*, Phys. Rev. Lett. **79**, 10 (1997)

[152] V. S. Khrapai, S. Ludwig, J. P. Kotthaus, H. P. Tranitz, W. Wegscheider, *Double-Dot Quantum Ratchet Driven by an Independently Biased Quantum Point Contact*, Phys. Rev. Lett. **97**, 176803 (2006)

[153] S. Smirnov, D. Bercioux, M. Grifoni, K. Richter, *Dissipative spin rectifiers based on Rashba's spin-orbit interaction*, to be published (2007)

[154] C. Ertler, J. Fabian, *Resonant tunneling magnetoresistance in coupled quantum wells*, Appl. Phys. Lett. **89**, 242101 (2006)

[155] C. Kittel, *Introduction to Solid State Physics* (John Wiley & Sons, Inc., New York, 1996)

[156] J. D. Jackson, *Classical Electrodynamics* (John Wiley & Sons, Inc., New York, 1999)

[157] S. V. Faleev, M. I. Stockman, *Self-consistent random-phase approximation for a two-dimensional electron gas: Kadanoff-Baym-Keldysh approach*, Phys. Rev. B **62**, 16707 (2000)

Acknowledgments

At this point I want to take the opportunity to say thanks to many people who accompanied me during my PhD time.

In the first place I want express my gratitude to my supervisor Prof. Dr. Klaus Richter, who gave me the possibility to work in his group. In many discussions he helped me to overcome fundamental difficulties and showed me new directions to proceed. Without his assistance this work surely would not be present in this form.

I am very grateful to PD Dr. Peter Schlagheck, who had a lot of ideas and recommendations in the context of the 0.7 anomaly, and to Matthias Scheid who intensively supported me with regard to the ratchet systems. I benefitted a lot from the close collaboration with both of them.

Herzlichen Dank, *muchas gracias* and *teşekkür ederim* to my officemates Dr. Tobias Paul, Prof. Dr. Juan Diego Urbina and Dr. İnanç Adagideli for endless conversations about physics and life in general. They created a friendly and humorous atmosphere in our office so that it was a pleasure to spend my working days.

Many thanks to Michael Wimmer, Andreas Pfund, Dr. Christian Ertler, Michael Hartung, Dr. Dmitry Ryndyk, PD Dr. Jens Siewert, Dr. Marko Turek and Prof. Dr. Rodolfo Jalabert for numerous discussions about Green functions, numerical implementations, electrostatics, diagrammatics and general physics.

I would like to thank Angie Reisser for her support with all administrative matters and for contributing a lot to the pleasant atmosphere in our institute. In this regard I am also grateful to all other members of our chair for turning the past few years into a beautiful period of my life with lots of colleagues becoming my friends.

I am indebted to Dr. Abi C. Graham and Prof. Sir Michael Pepper for inviting me to their lab at the University of Cambridge and giving me the opportunity to present my results. There I had many fruitful meetings with the pioneers of the 0.7 anomaly and I was highly inspired after exchanging lots of new ideas.

Special thanks go to our system administrators Michael Wimmer, Michael Hartung and Matthias Scheid for their never-ending patience with my stupid questions and for promptly helping me with any small and big computer problems.

I am grateful to my parents Monika and Johann for their continuous support, especially during my time at the university.

Finally I want to thank my girlfriend Agnes for being the "wind beneath my wings". Her loving care helped me to survive the unsuccessful periods of my work and she always gave me new drive and inspiration whenever I needed it.

I acknowledge financial support by the *Freistaat Bayern* and the DFG within the research school GRK 638 *"Nichtlinearität und Nichtgleichgewicht in kondensierter Materie"*.

Andreas Laßl
October 2007